New Methods for Synchrophasor Measurement

Yingchen Zhang

Dissertation submitted to the faculty of the Virginia Polytechnic Institute and State University in partial fulfillment of the requirements for the degree of

Doctor of Philosophy

In

Electrical Engineering

Yilu Liu (Co-Chair)

Virgilio Centeno (Co-Chair)

Richard W. Conners (Committee Member)

Ahmad Safaai-Jazi (Committee Member)

Tao Lin (Committee Member)

7 December 2010

Blacksburg, Virginia

Keywords:

Electric and magnetic fields, Synchrophasor measurement, Discrete Fourier transform, Nonlinear least squares, Angle instability

New Methods for Synchrophasor Measurement

Yingchen Zhang

ABSTRACT

Recent developments in smart grid technology have spawned interest in the use of phasor measurement units to help create a reliable power system transmission and distribution infrastructure. Wide-area monitoring systems (WAMSs) utilizing synchrophasor measurements can help with understanding, forecasting, or even controlling the status of power grid stability in real-time. A power system Frequency Monitoring Network (FNET) was first proposed in 2001 and was established in 2004. As a pioneering WAMS, it serves the entire North American power grid through advanced situational awareness techniques, such as real-time event alerts, accurate event location estimation, animated event visualization, and post event analysis.

Traditionally, Phasor Measurement Units (PMUs) have utilized signals obtained from current transformers (CTs) to compute current phasors. Unfortunately, this requires that CTs must be directly connected with buses, transformers or power lines. Chapters 2, 3 will introduce an innovative phasor measurement instrument, the Non-contact Frequency Disturbance Recorder (NFDR), which uses the magnetic and electric fields generated by power transmission lines to obtain current phasor measurements. Prototype testing of the NFDR in both the laboratory and the field environments were performed. Testing results show that measurement accuracy of the NFDR satisfies the requirements for power system dynamics observation.

Researchers have been developing various techniques in power system phasor measurement and frequency estimation, due to their importance in reflecting system health. Each method has its own pros and cons regarding accuracy and speed. The DFT (Discrete Fourier Transform) based algorithm that is adopted by the FDR device is particularly suitable for tracking system dynamic changes and is immune to harmonic distortions, but it has not proven to be very robust when the input signal is polluted by random noise. Chapter 4 will discuss the Least Mean Squares-based methods for power system frequency tracking, compared with a DFT-based algorithm. Wide-area monitoring systems based on real time PMU measurements can provide great visibility to the angle instability conditions. Chapter 5 focuses on developing an early warning algorithm on the FNET platform.

ACKNOWLEDGEMENT

I would like to express my deepest gratitude to my primary advisor, Dr. Yilu Liu. She introduced me into a world leading research group in the power and guided me through a greater than ever four-year journey. She is a great mentor for my research, a wise counselor for my personal development, and a beloved friend to share good times. I would like to thank Dr. Richard W. Conners, Dr. Vigilio A. Centeno and Dr. Jaime De La Ree for their enthusiasms in teaching and studying, which brings great courage and joy to my research. I am thankful for great advisers Dr. Ahmad Safaai-Jazi and Dr. Tao Lin, who served in my dissertation committee.

Many thanks go to my former group members, Jingyuan Dong, Robert M. Gardner, Joshua K. Wang, Tao Xia, Jason N. Bank, Lei Wang, Robert Jon Burgett, and Mark W. Baldwin. Their brightness and success enlightened my path of pursuing higher level on my academics.

I am greatly appreciative of the help and friendship of Penn Markham, Lang Chen, YanZhu Ye, and Zhongyu Wu.

Last but not least, I would like to thank the graduate students and visiting scholars in FNET and the Power Systems Laboratory for the help and friendship they have given to me.

The time flies, but the memory stays. I will cherish my four years at Virginia Tech as one of my best memories.

To my beloved wife, Chunmei Ban. You are the most beautiful thing that ever happened to me. I am blessed to have you by my side along the journey of my life.

Table of Contents

Table of Figures

List of Tables

Chapter 1 Background

1.1 Synchrophasor measurement and Frequency Monitoring Network

GPS time-synchronized phasor measurements [1]-[4] were introduced in the mid -1980's. Since a Virginia Tech research team developed the first prototype PMU in 1988, PMUs have been gradually but cautiously deployed throughout the North American power system. The initial field installations of the PMUs were in the service territories of Bonneville Power Administration, American Electric Power, and the New York Power Authority. At present, there are only 105 PMUs installed in the Eastern Interconnection (EI) and 56 in the Western Interconnection (WECC).

As a member of the PMU family, the Frequency Disturbance Recorder (FDR) was developed at Virginia Tech in 2003. Thus far there are about 80 FDRs installed in the United States and another 20 installed worldwide. Figure 1.1 is a distribution map indicating the locations of all the FDRs deployed in North America. A wide-area Frequency Monitoring Network (FNET) was constructed by utilizing the FDR data collected from the three interconnections in North America. FNET has served utilities, academics and regulators since 2004 with valuable synchrophasor data and its applications [5]-[8].

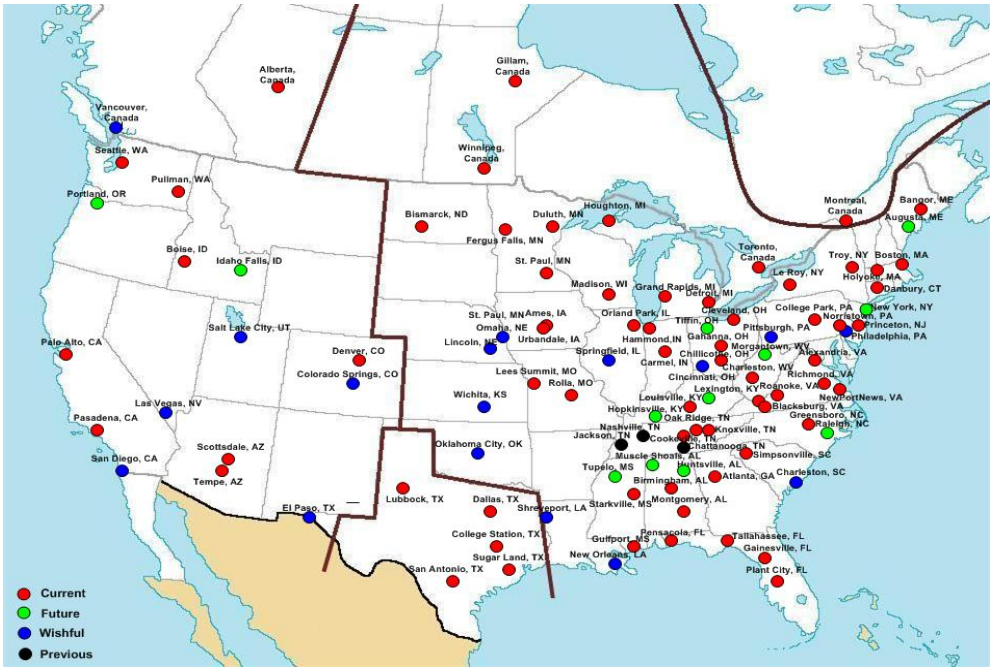

Figure 1.1 Map of FDR locations in North America

The main reason for the rapid FNET deployment is the extremely low cost and high accuracy dynamic measurements that this system makes possible. Each FDR itself is actually a single phase PMU in the sense that it measures the voltage phase angle, amplitude and frequency from a single phase voltage source. The fact that the FDRs are installed at the 120V distribution level reduces their manufacturing and installation costs significantly. The frequency measurement algorithm in the FDRs makes use of phasor analysis and signal re-sampling techniques, which have virtually zero algorithm error in the range between 52 and 70 Hz [6]. Real hardware accuracy of the FDRs falls into the interval of ±0.0005 Hz, which is better than certain commercial PMUs [11].

Frequency is a universal parameter across the entire interconnected power system [9], [10]. It can provide information about generation electro-mechanical transients, generation-demand dynamics, and system operations, such as load-shedding, break reclosing, and capacitor bank switching. This characteristic allows frequency monitoring to be as informative at the distribution level as it is at the transmission level. Phasor calculation in the FDRs is derived from real-time voltage signal sampling and its Discrete Fourier Transform-based complex representation. Voltage phase angles and magnitudes are also measured by FDRs, which can provide useful information for power system event recognition and status estimation.

1.2 FNET structure and FDR framework

Figure 1.2 demonstrates the key components of the FNET system. Phasor measurements from the North American power grids are collected by widely installed sensors, known as FDRs, and are transmitted via the Internet to a local client or remote data center. In most of the cases, FDR data are transmitted to the FNET data center for processing and long term storage.

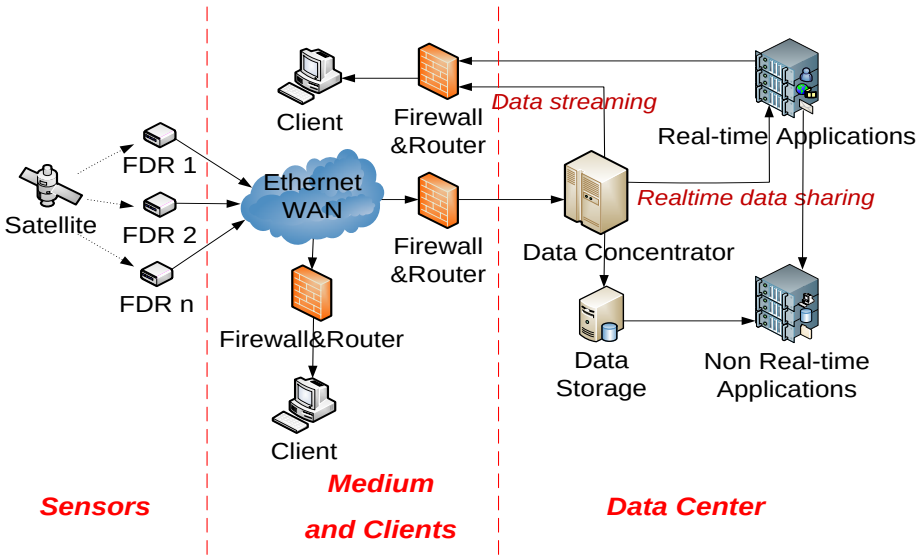

Figure 1.2 Building blocks of the FNET system

Each FDR is equipped with a GPS receiver, which is used to provide the accurate time signal needed for synchrophasor calculation. The units are powered from ordinary 120 V electrical outlets, which also provide the power signal used to compute the phasor value. Internet access is required in order for FDRs to transmit their measurement results. They are installed in a variety of locations, such as power plants, substations, office buildings, and private residences.

Measurement data from FDRs are managed in the data center by multi-layer agents. The top layer is the FNET data concentrator, whose primary functions are to receive data from the FDRs, create GPS time-aligned records, share data with the real-time application agent as soon as the records are made, and forward the data records to the data storage agent and subscribed clients. The real-time application agent and data storage agent are in the second layer of the data center hierarchy. The third layer is the non-real-time application agent.

First built in 2003 [11], [12], the FDR is now in its second generation as shown in Figure 1.3. The first generation FDR was composed of a transformer, low pass filter, analog-to-digital converter (ADC), GPS receiver, microprocessor module, and Ethernet communications module. About 20 of the first generation FDRs are still in use and provide measurement data to the FNET system or to local client systems. Figure 1.4 and Figure 1.5 demonstrate the framework of the first and second generation FDR. The second generation FDR has been upgraded with more integrated PCBs. Instead of using a single microprocessor to handle both intensive calculation and communications, the newer version implements a digital signal processor (DSP) for data

calculation and a microcontroller for communicating coordinates with the GPS module and the Ethernet card. In terms of accuracy, the newer version FDR utilizes an active filter design instead of an inductor-capacitor L-C filter as in the first generation FDR. It has a sharper cut-off frequency edge which leads to less noise allowance.

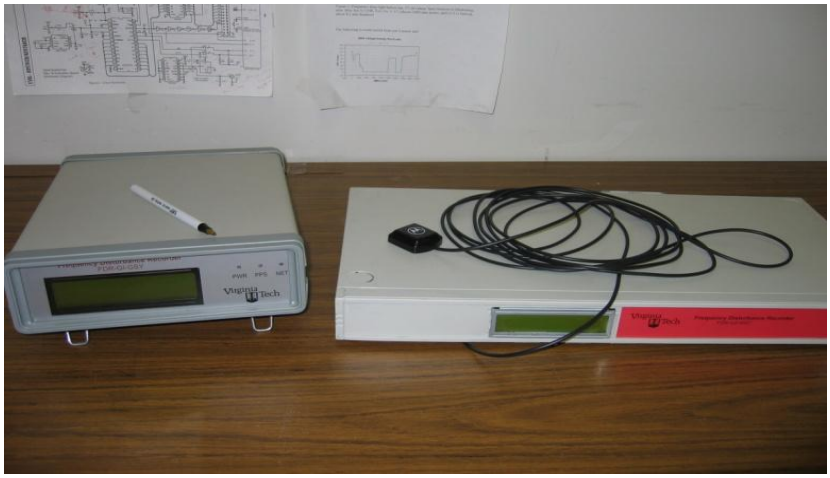

Figure 1.3 Photo of the first generation FDR (right) and the second generation FDR (left)

Despite the differences in hardware layout, both generation FDRs are driven by the same principle. A regular power outlet's 120 V sinusoidal voltage signal is stepped down to 10 V by the internal transformer of the FDR. High frequency noises are then blocked by the low pass filter. The ADC periodically samples the 10 V signal according to the GPS clock regulated oscillator pulses. (Oscillator pulses are synchronized with a one pulse per second (PPS) signal, provided by the GPS module.) Phasor values such as voltage magnitude, phase angle, and frequency are calculated by the central processing units and then transmitted over the Internet by the device server.

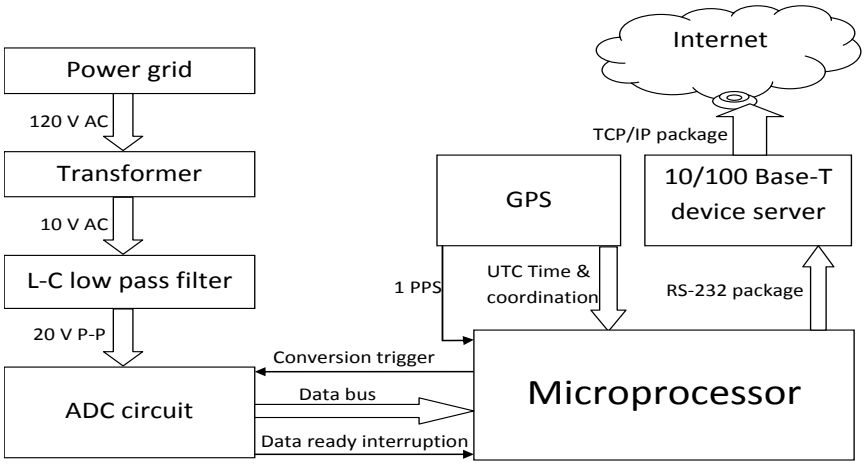

Figure 1.4 First generation FDR hardware block diagram

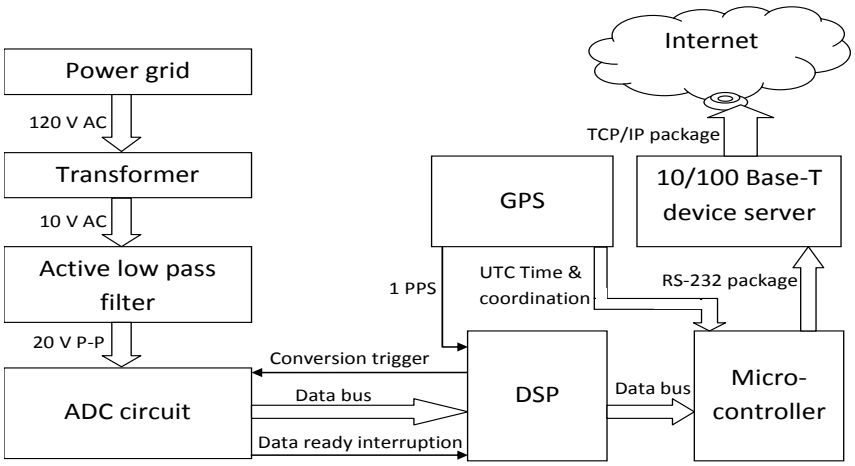

Figure 1.5 Second generation FDR hardware block diagram

The resulting frequency accuracy of the FDRs is ±0.0005 Hz or better. A comparison was made in 2003 between one FDR and four commercial PMUs from two different manufacturers. During the comparison period, PMUs and the FDR measured the same voltage phasor from a wall outlet. Wang et. al. in [11] concluded that the FDR frequency measurement accuracy is more refined than that of the four commercial PMUs.

1.3 FNET applications

FNET applications [13]-[28] can be divided into real-time applications and non real-time by their response time frame. Real-time applications require response within seconds or even sub-seconds after receiving the data, while non-real-time applications have more flexible timing requirements. The FNET system defines applications that operate on the data in the memory cache as real-time and those that operate on any other saved data as non-real-time. The FNET applications now under service include: Frequency monitoring interface, Event trigger, Oscillation trigger, Event location, Oscillation modal analysis, Event visualization, and Web service. The overall structure of FNET data flow and applications' hierarchy is demonstrated in Figure 1.6.

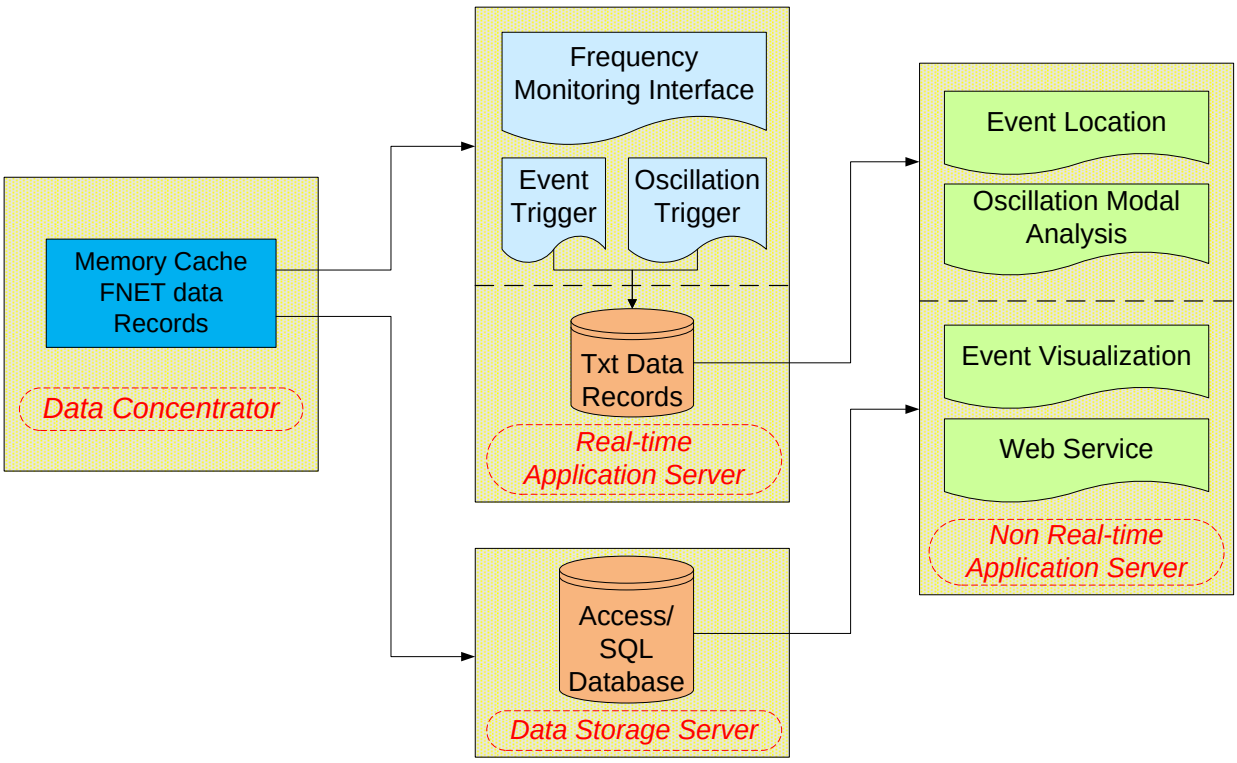

Figure 1.6 FNET data flow and applications' hierarchy

Chapter 2 Magnetic field based phasor measurement

2.1 Overview of Magnetic Field sensor-based phasor measurement

Many practical power system applications require that a large number of PMUs are installed at critical locations (generator plants and transmission substations) throughout an interconnected power system. Due to the high installation costs of these PMUs, only a small number of them have been installed in the United States during the last 30 years [29], [30].

Traditionally, Phasor Measurement Units have utilized signals obtained from current transformers (CTs) to compute current phasors. Unfortunately, this requires that CTs must be directly connected with buses, transformers or power lines. This paper will introduce an innovative phasor measurement instrument, the Non-contact Frequency Disturbance Recorder (NFDR), which uses the magnetic field generated by power transmission lines to obtain current phasor measurements.

The NFDR is developed on the same hardware platform as the Frequency Disturbance Recorder (FDR), which is actually a single phase PMU. Prototype testing of the NFDR in both the laboratory and the field environments were performed. Testing results show that measurement accuracy of the NFDR satisfies the requirements for power system dynamics observation.

2.2 Frequency calculation from voltage phase angle

Phadke et. al. in [71] discussed using a Fourier Transform based method for phase angle calculation and frequency estimation. A sinusoidal voltage signal can be periodical sampled with a time interval Δt. Assuming the signal frequency remain constant until the k th sampling point, the voltage signal at the k th sampling point can be represented by (2-1).

$$V_k = \sqrt{2}V_{\max}\sin(2\pi fk\Delta t + \phi) = \sqrt{2}V_{\max}\sin\Phi_k \qquad (2\text{-}1)$$

If the frequency of the signal is now changed slightly by some amount Δf, the $(k+1)$ th sampling point can be represented by (2-2).

$$V_{k+1} = \sqrt{2}V_{\max}\sin(\Phi_k + 2\pi(f+\Delta f)\Delta t) = \sqrt{2}V_{\max}\sin\Phi_{k+1} \qquad (2\text{-}2)$$

The change of frequency can be calculated from the rate of change of phasor angle as shown in (2-3).

$$\Delta f = \frac{1}{2\pi} \bullet \frac{d\Phi}{dt} - f \qquad (2\text{-}3)$$

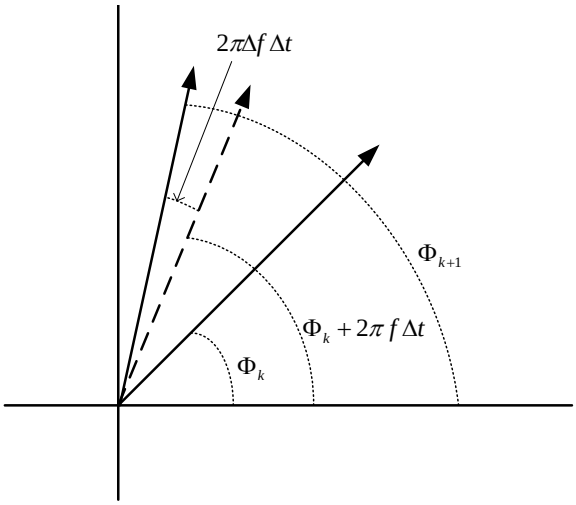

Figure 2.1 Phase angle and frequency deviation.

Figure 2.1illustrates the incremental phase angle in the presence of frequency deviations.

The magnetic field generated by alternating voltage also exhibits the same alternating characteristics in the time domain. Thus, the phase angle based frequency calculation can also be applied to electric field signal. Each FDR unit is a single phase PMU in the sense that it measures the single phase voltage phasor instead of the positive sequence voltage phasor. Thus, the NFDR will have the capability of phasor measurement if the input signal can be directly linked to the power system voltage or current. Since the frequency is the final result of the algorithm, it is logical to assess NFDR accuracy from its frequency output.

2.3 Principles of magnetic field sensor based phasor measurements

Two well-known physical principles are involved in measuring current phasors via the magnetic field - Ampere's Law and Faraday's Law. AC current flowing through transmission lines will generate changing magnetic fields in the surrounding atmosphere as well as in nearby objects, as stated in Ampere's law. By Faraday's law, if there is a coil placed in a certain direction in the magnetic field, the changing flux will induce a voltage in the coil. This *current*

→ *magnetic field* → *induced voltage* transition enables wireless phasor measurement functionality.

As shown in Figure 2.2, the distance between the measurement point and the power line is represented by ***r***. If current flow through a single conductor of the power line is $I_m \cdot \sin(2\pi ft + \theta)$, the magnetic field strength at the measurement point can be calculated with (2-4). Magnetic field strength is a vector quantity. Its direction can be determined by using the Right-Hand rule. For measurement purposes, only the direction of maximum field strength is considered in the calculation.

$$B = \frac{\mu \cdot I_m \cdot \sin(2\pi ft + \theta)}{2\pi r} \tag{2-4}$$

Induced voltage in a coil of *N* turns at a measurement point can be calculated with (2-5).

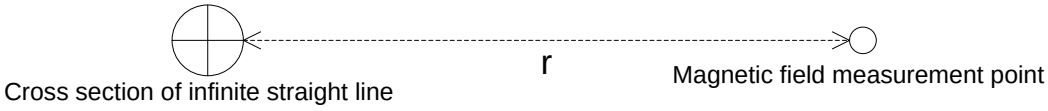

Figure 2.2 Magnetic field strength generated by infinite line

$$E = N\frac{d\Phi}{dt} = NS\frac{dB}{dt} = NS \cdot \frac{\mu \cdot I_m \cdot f \cdot \sin(2\pi ft + \theta + 90^\circ)}{r} \tag{2-5}$$

where:

E: Induced voltage

B: Magnetic field strength

μ: Magnetic permeability of the medium

I_m: Maximum value of current flowing through the power line

f: Frequency of current flowing through the power line

Φ: Magnetic flux

N: Number of turns of sensor coil

S: Area of each turn

In reality, transmission lines contain several conductors from three phases. Therefore, the magnetic field at the measurement point will be a summation of several magnetic fields with 120

degree phase shift from each other. It is easy to conclude from (2-4) that the summation of magnetic fields with different ***r*** values will also have a frequency of *f*. Figure 2.3 is a demonstration of three sinusoidal magnetic fields that are 120 degrees out of phase with one another being added together. For simplicity, amplitudes of 60, 80, and 100 were assigned to each of the fields using radian frequency $2\pi f = 1$.

Standard measurement for transmission line magnetic fields should be carried out at the edge of the transmission line right-of-way as shown in Figure 2.4.

The width of right-of-way varies in different states from 70 feet to 200 feet [32-35] for different voltage level lines. The calculated magnetic field strength also varies from 1 to 2 μT with the voltage level as shown in Table 2-I [36]-[40].

The magnetic field sensor should be designed as such that the induced voltage is strong enough for analog to digital converter (A/D) sampling. It is intuitive that the bigger the sensor is, the stronger the signal will reach. However, it is not practical to use a large sensor for a portable measurement device.

$$E = N\frac{d\Phi}{dt} = NS\frac{dB}{dt} = NS\cdot\mu_0\frac{\sqrt{2}}{2}\frac{A}{2r}\cdot 2\pi f = N\cdot\pi\frac{D^2}{4}\cdot B\times 10^{-6}\cdot 2\pi f \qquad (2\text{-}6)$$

Equation (2-6) demonstrates the factors that decided the signal strength are the number of turns of the sensor coil (N) and its diameter (D), by assuming that the magnetic field strength at the measurement point is 1 μT.

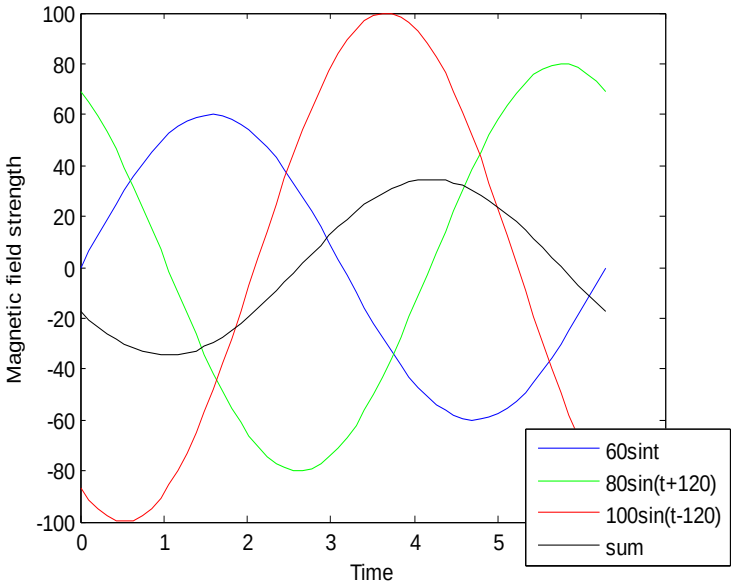

Figure 2.3 Individual and Sum of magnetic fields generated by three phase line currents

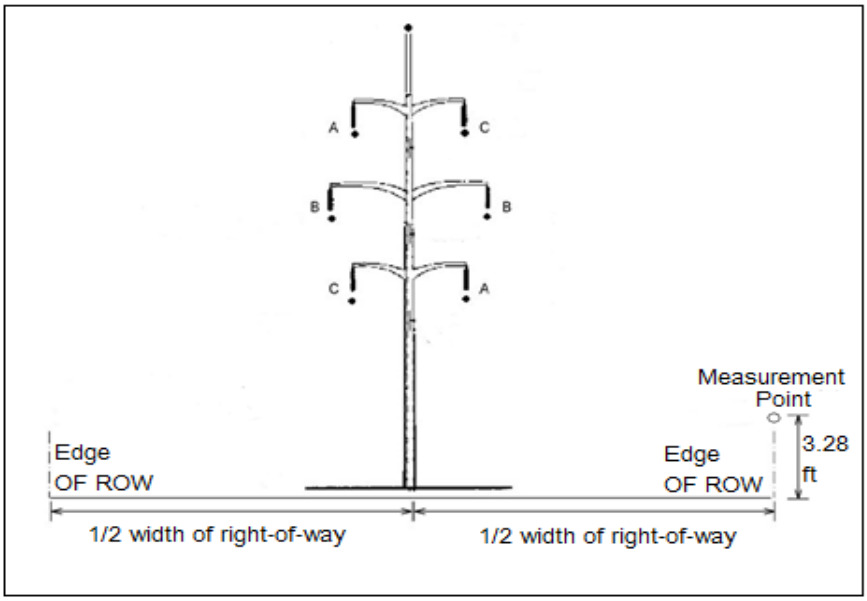

Figure 2.4 Measuring Instrument Placement at Transmission Line Right of Way

Table 2-I Typical magnetic field strength for different voltage level lines

Transmission line voltage level	138 kV	230 kV	500 kV
RMS Current (A)	1000	1500	2000
Magnetic Field at the edge of right-of-way (μT)	1.0	1.3	1.7

2.4 Magnetic field based NFDR structure

The NFDR system inherits from the FDR framework [41], [42]. The major components of the FDR such as a low pass filter, analog-to-digital converter (ADC), GPS receiver board, microprocessor development board and network communication module are retained in the new system. A magnetic field sensor and an amplifying circuit compose the signal input end. The overall structure of the NFDR is described in Figure 2.5.

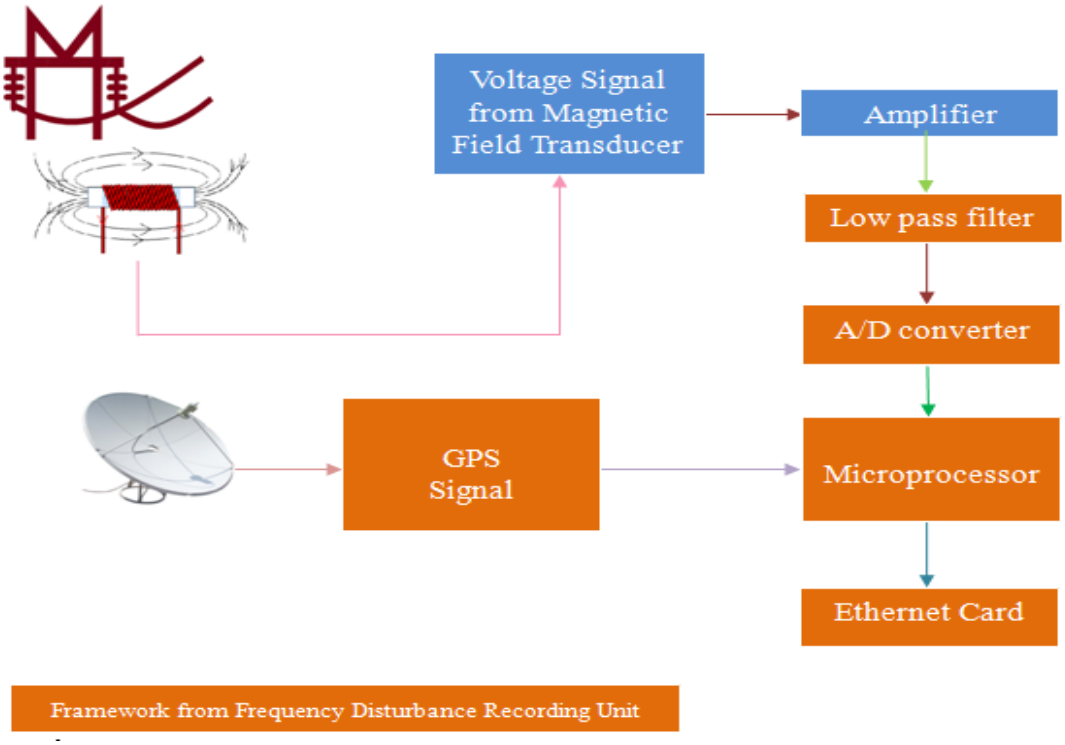

Figure 2.5 NFDR overall structure

2.5 NFDR laboratory testing

Two scenarios are performed in the laboratory testing procedure. In both of the scenarios, a magnetic field that simulates the actual magnetic field at the edge of a power line right-of-way is generated by a coil. This coil is called the *source coil* to be distinguished from the *sensor coil*.

2.5.1 Laboratory testing scenario one

In the first laboratory testing scenario, the source coil is connected to the output channel of an Agilent 6811B AC source. The major components and the layout of the testing system are shown in the photos in Figure 2.6 and Figure 2.7. Signals generated by the AC source are applied to the source coil. The sensor coil capture the magnetic field generated by the source coil and transfer

the induced voltage signal to the NFDR. By changing the output voltage magnitude of the AC source, the magnetic field strength is set to 2 μT at the location of the sensor coil. The frequency of the magnetic field can also be adjusted by varying the AC source output frequency so that NFDR measurement accuracy under different frequencies can be estimated. Two different sensor coils are tested separately in scenario one. Their dimensions are listed in Table 2-II.

Figure 2.6 From left to right: Agilent AC source, Source and senor coil, Crown PS-400 Amplifier

Figure 2.7 The NFDR system as it is arranged during laboratory testing

Table 2-II Dimensions for two types of coils

Dimension	Number of turns	Coil length	Coil diameter	
			Inner	External
Coil 1	800	3cm	2cm	5cm
Coil 2	600	3cm	2cm	6cm

Figure 2.8, Figure 2.9, and Figure 2.10 demonstrate the induced voltage on the sensor coils and the voltages signals after being amplified and filtered. When the coil diameters are almost the same, the more turns the coil has, the stronger the voltage signal can be generated.

A 26 V peak-to-peak voltage signal is applied to the A/D converter from 800 turns coil while it is 22 V from the 600 turns coil. The A/D converter in the NFDR is referenced to a rated ±12 V supply, and actual measurement shows its limit can reach to ±15 V. When the input signal to the A/D converter reaches its intake limit, its digitalization resolution will be fully utilized.

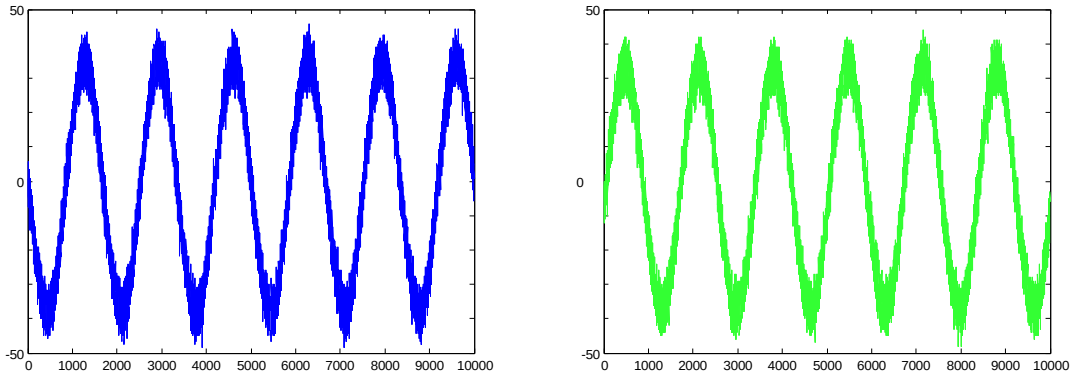

Figure 2.8 Voltage signal output from sensor (Unit: mV) for coil 1 (left) and coil 2 (right)

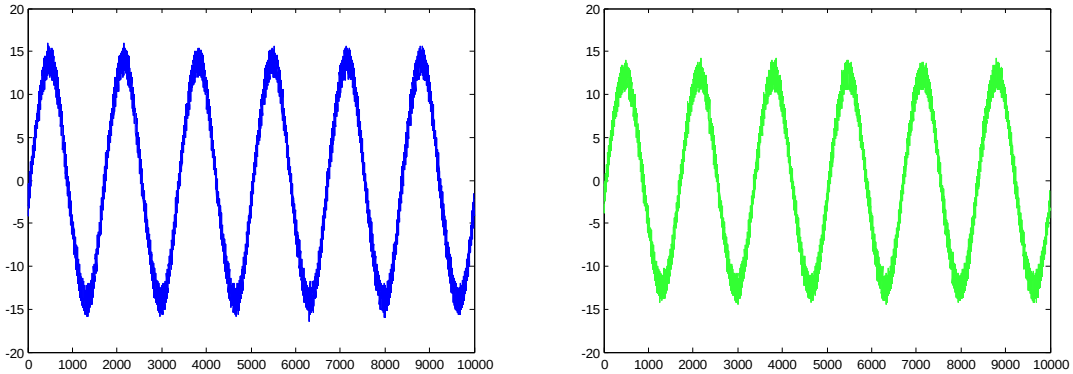

Figure 2.9 Voltage signal output from amplify (Unit: V) for coil 1 (left) and coil 2 (right)

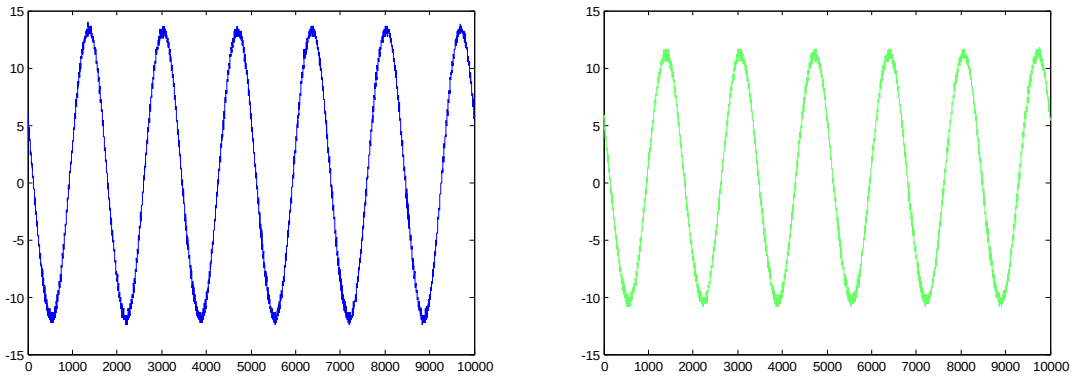

Figure 2.10 Voltage signal output from low pass filter (Unit: V) for coil 1 (left) and coil 2 (right)

Four frequency steps, 59.90Hz, 59.98Hz, 60.02Hz and 60.10Hz are applied to the NFDR. Figure 2.11 shows the measurement at a frequency stage of 59.9Hz for both of the sensors. Statistical analysis results of 300 seconds worth of data from each step are listed in Table 2-III. Error is calculated by direct subtraction of the measurement average from the input signal frequency. Standard deviation of measurement data can illuminate device measurement stability and noise band.

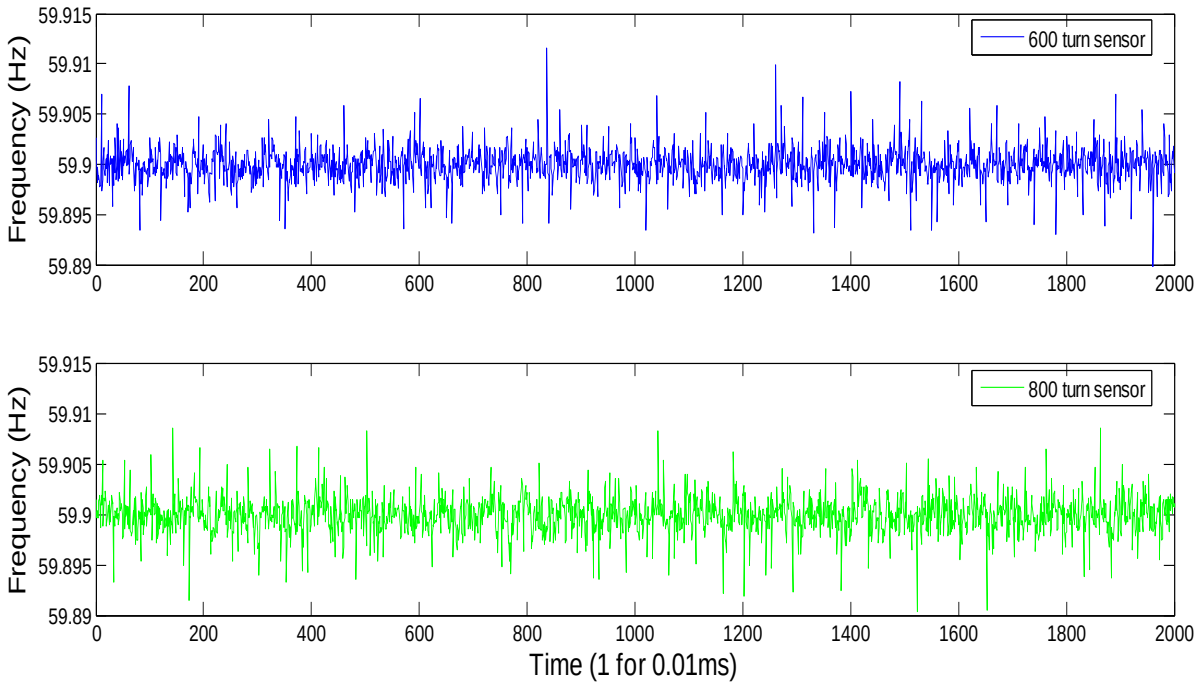

Figure 2.11 Measured frequency when input signal is 59.9Hz (Unit: Hz) for coil 1 (top) and coil 2 (bottom)

Table 2-III Measured frequency comparison for two types of coils

Coil type		1			2		
Coil Turns		800			600		
Test result	Input signal Frequency	Measured Average	Error	STD	Measured Average	Error	STD
	59.90Hz	59.89996	0.000039	0.0017	59.89988	0.000115	0.001821
	59.98Hz	59.97997	0.000029	0.001631	59.97998	0.000014	0.001986
	60.02Hz	60.01997	0.000063	0.001942	60.01990	0.000093	0.001896
	60.10Hz	60.09994	0.000059	0.001691	60.09985	0.000147	0.001927
Average error %		0.000319%			0.000618%		

From the table, frequency measurements of the NFDR under steady-state condition are 0.001%. Also, the measurements' standard deviations during the tests are all smaller than 0.002 Hz, which illustrates that the NFDR steady-state frequency measurements are stable and within a narrow band. It is also obvious that when the diameters are the same, the sensor with more turns has higher measurement accuracy because it produces a stronger signal for the A/D converter.

2.5.2 Laboratory testing scenario two

In the second scenario, only one major change in the testing procedure has been made, which is the replacement of the Agilent AC source with an extension power stripe connected to a regular wall outlet. A GE Volt-PAC Variac controls the signal that feeds into the source coil. NFDR measurement accuracy is estimated by comparing this with the measurement obtained from a FDR device that is directly connected to the same wall outlet. Since test scenario one has already proved that the 800-turn coil can produce a stronger signal, in test scenario two, only the 800-turns coil is used as the sensor coil.

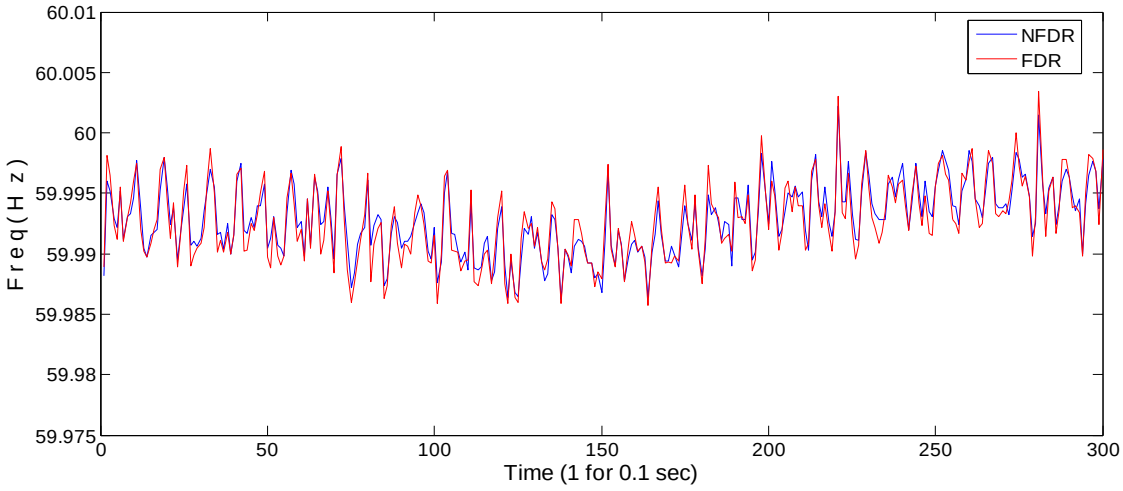

Figure 2.12 Measured frequency (Unit: Hz) of NFDR and FDR

Figure 2.12 shows 30 seconds worth of data plotted for both NFDR and FDR devices. They closely match with each other in such a high resolution. Their absolute difference is plotted in Figure 2.13 to illustrate the relative error that compares one measurement to the other. The root-mean-square (RMS) value of the difference reflects an average level of the measurement difference of the two, and the standard deviation of the measurements difference indicates the variance of one device's measurements from the other.

As shown in Table 2-I, the difference between NFDR frequency measurements and the FDR frequency measurements is at the 0.001 Hz level.

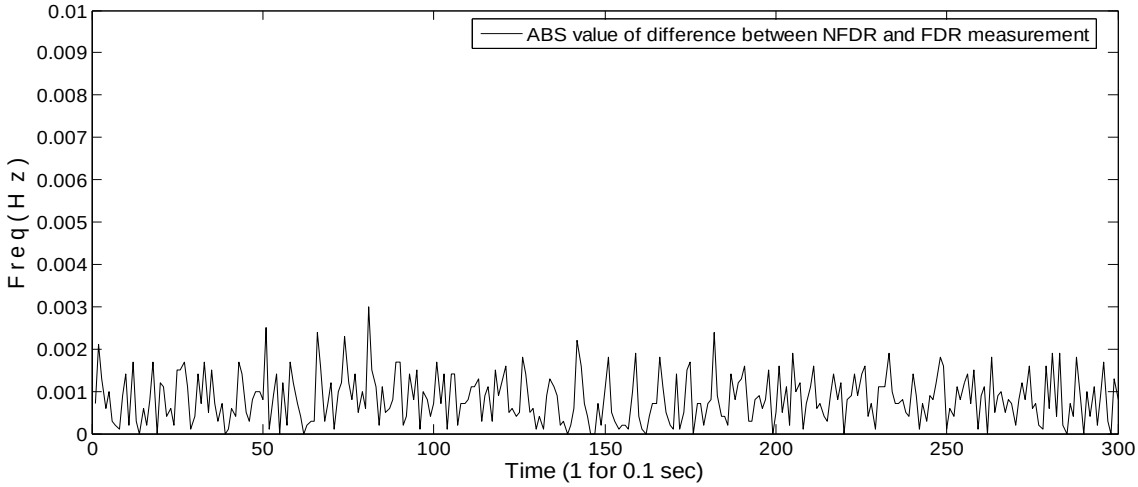

Figure 2.13 Absolute value of measured frequency difference between NFDR and FDR

Table 2-IV Statistics of measured frequency difference between NFDR and FDR

Time	21/2/2008 6:00-6:30	21/2/2008 13:00-13:30	21/2/2008 21:00-21:30
RMS of Freq Difference	0.0009863	0.0010442	0.0011113
Standard Deviation of Freq Difference	0.0009839	0.0010413	0.0011084

2.6 NFDR field testing

Ultimately, the NFDR power supply should be self-sustainable because the system is designed for flexible field measurement. A solar panel and rechargeable lithium battery combination will be a better option for that purpose. However, at the current stage of prototype testing, a fully charged Uninterruptible Power Supply (UPS) is sufficient to power the system for up to one hour in the field. Also, for data transmission, a complete NFDR needs to possess wireless communication capability. In the development phase, however, the device transmits data via Ethernet or crossover cable to desktop (laboratory test) or laptop (field test) PCs. The proposed final framework is shown in Figure 2.14.

During the field test, even when the magnetic field strength is approximate 1 μT, the induced voltage in the sensor coil can only be measured around 0.5 mV. Thus, a high gain amplifier as displayed in Figure 2.15 is designed and integrated into to the NFDR framework. It has adjustable gain ratios that can accommodate different signal strengths.

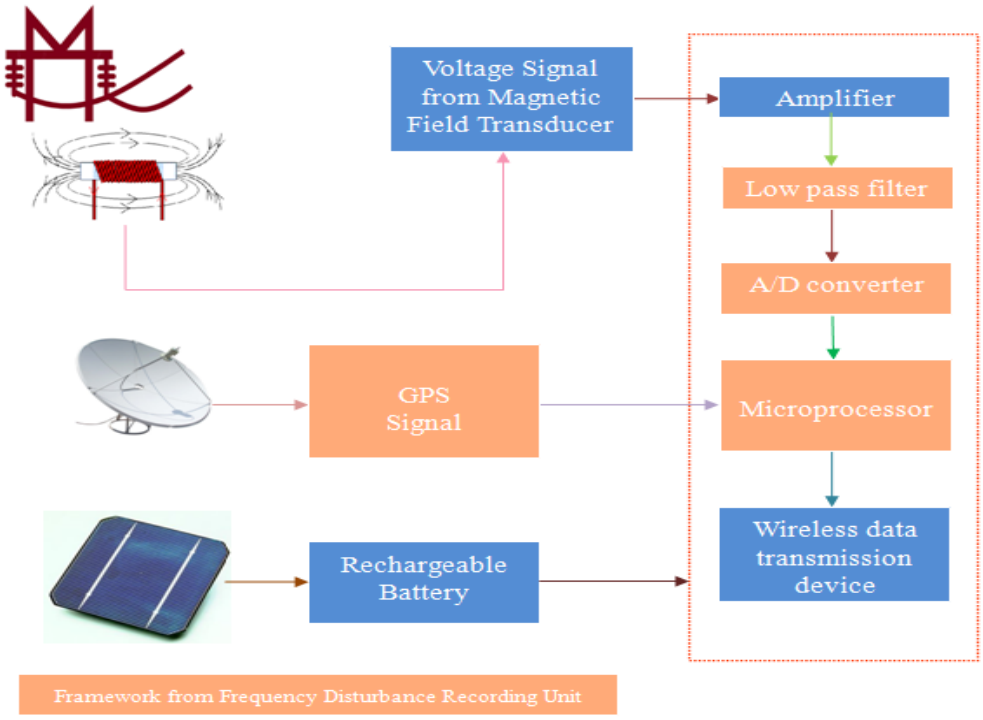

Figure 2.14 Proposed NFDR structure

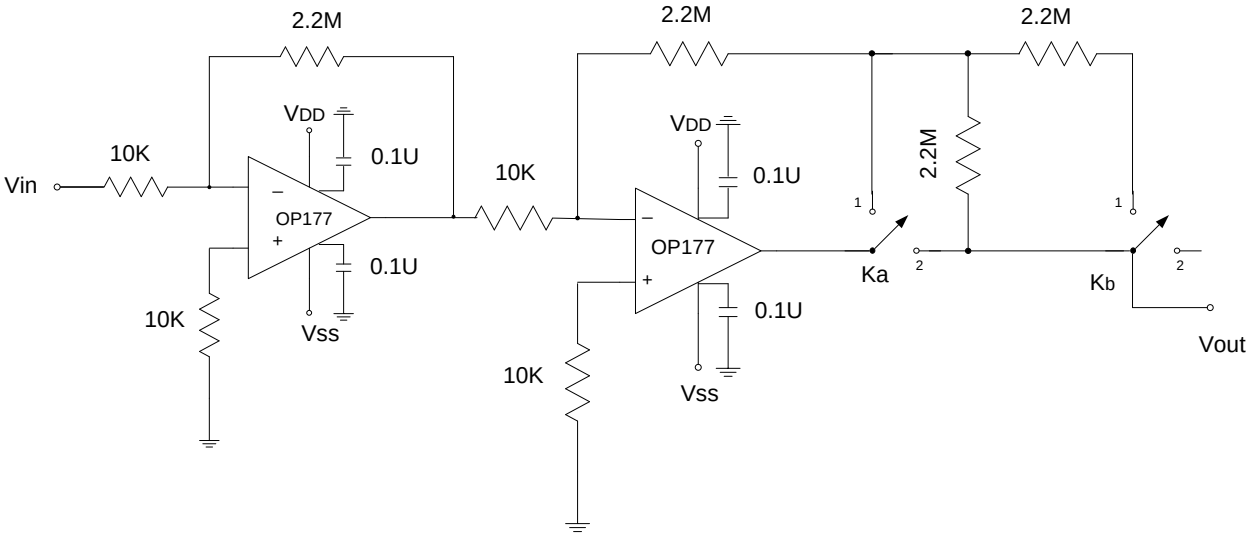

Figure 2.15 The high gain amplifier circuit

Table 2-V Switch positions and the according amplifying ratio

Switch	Position	Gain Ratio	Position	Gain Ratio	Position	Gain Ratio
Ka	1	40000	2	60000	2	80000
Kb	2		1		2	

Figure 2.16 The NFDR in field testing

There are several challenges and uncertainties associated with bringing NFDR systems to a field environment. One is that the magnetic field strength is not stable at transmission line right-of-way edges. Figure 2.16 is a photograph of a NFDR taken during the field testing. Note that the oscilloscope is not a component of the measurement system but is used for monitoring the induced voltage from magnetic field sensors in order to detect potential problems.

2.6.1 Harmonics and digital filter design

The first trial of field testing is took place on the Virginia Tech campus. The testing equipments were setting up close to the feeder lines of the 69/12.47 kV substation located on Turner Street.

Figure 2.17 displays the voltage signal output from the amplifier. By looking at its Fast Fourier Transform (FFT) analysis result, the dominant frequency components in this signal are the 3^{rd} and 9^{th} harmonics. The fundamental frequency component is too weak for phasor and frequency calculation. There are various reasons that can cause this problem, since the device is close to the transformers; it is highly likely that the sensor captures the magnetic field generated by the transformers. Their core saturations could cause harmonic distortions in the secondary.

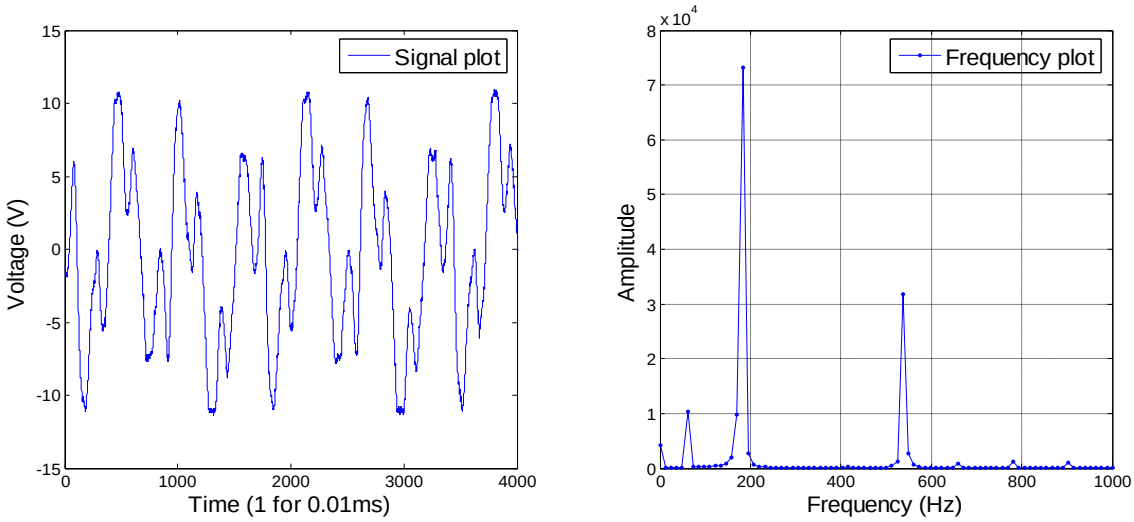

Figure 2.17 Amplifier output voltage signal and its FFT analysis

The second trial of field testing was carried out at the right-of-way (ROW) of a 138 kV transmission line close to the intersection of Interstate 81 and Route 460 in Christianburg, Virginia. Figure 2.18 displays the amplifier output signal and its FFT analysis result.

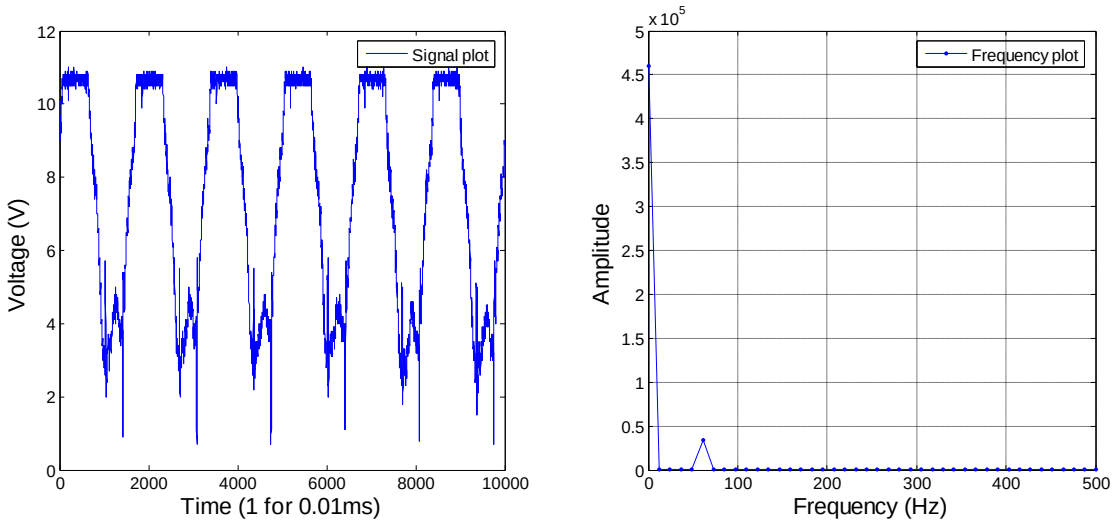

Figure 2.18 Amplifier output voltage signal and its FFT analysis

Clearly, there is a large Direct Current (DC) component contained by the signal. However, by moving the NFDR along the edge of the ROW, a better signal reception is obtained as shown in Figure 2.19. The reason for the DC component remains unclear because neither coupling of the magnetic field nor the electric field under a transmission line will produce a DC offset in the

sensor. The DC offset is a minor concern since the series connected capacitor in the low pass filter will block any DC component in the signal. The filter design is shown in Figure 2.20.

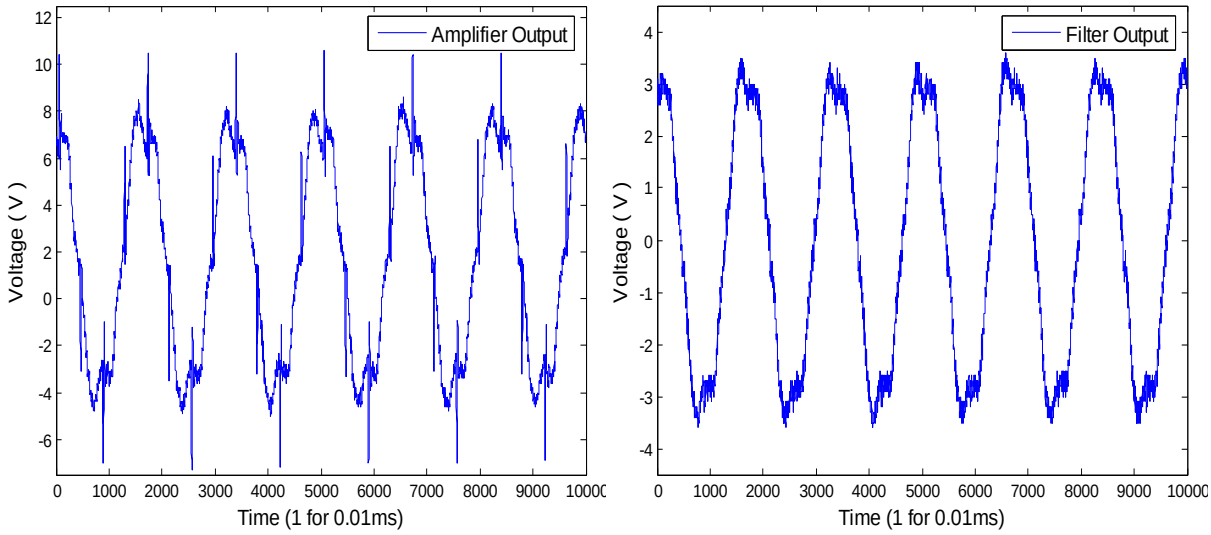

Figure 2.19 Voltage signal: amplifier output (left), filter output (right)

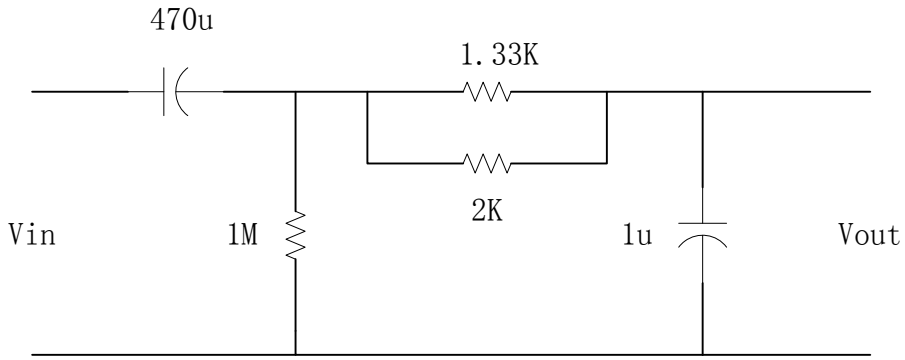

Figure 2.20 NFDR low pass filter

To examine the frequency components contained in the signal output from the filter, a FFT analysis is conducted and its result demonstrates the fundamental frequency is dominating as shown in Figure 2.21. However, spikes at harmonic frequencies can also be observed.

Figure 2.22 shows a screen shoot of the measurement frequency for one minute. It exhibits oscillating frequency measurements in a band between 59.88 Hz and 60.12 Hz. Based on the knowledge gained from historical FNET measurements, it can be concluded that this measurement is much nosier than the actual system frequency characteristics.

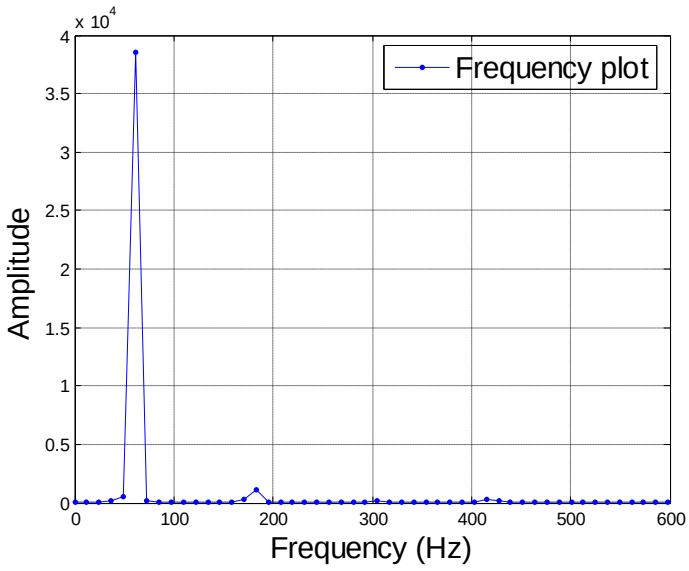

Figure 2.21 FFT analysis for signal from Low Pass Filter

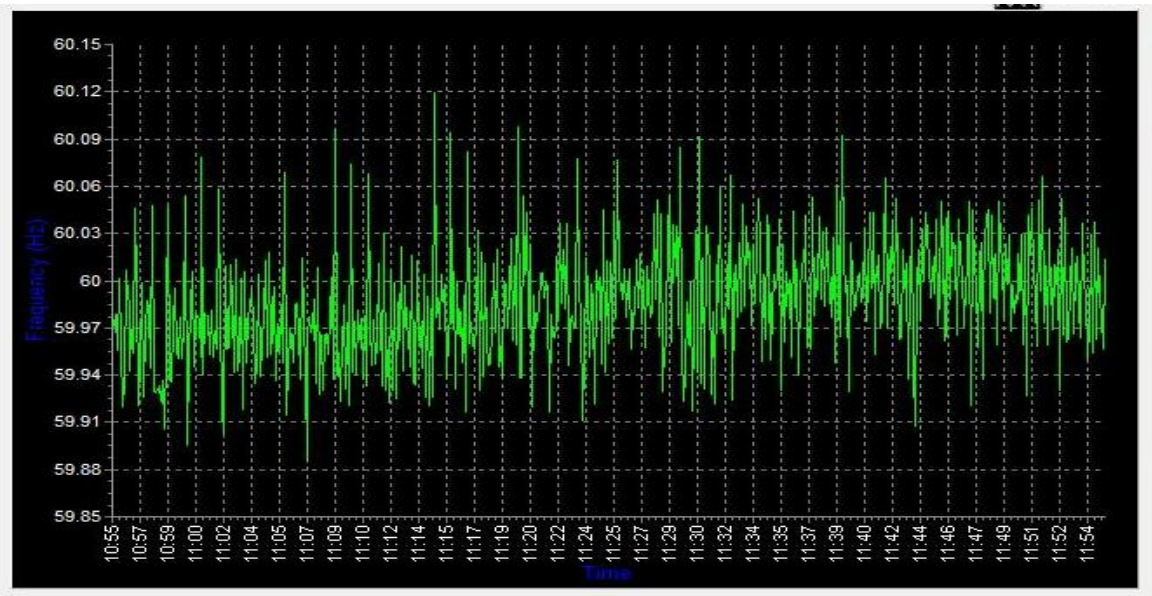

Figure 2.22 Measured frequency from first field test

From the signal condition analysis above, the measurement accuracy is limited for two reasons. The first reason is the poor signal quality. Compare with the clean sinusoidal signal waveforms captured during the laboratory testing, the signal from field measurement exhibits nosier patterns. The second reason is the weak signal strength. From Figure 2.19, the actual signal feed into the A/D converter is +3 V to -3 V. It is far from the rated A/D converter input

signal magnitude, which will dramatically reduce its resolution when transferring analog signal to digital ones.

A frequency scan is done to the RC low pass filter by PSPICE simulation as illustrated in Figure 2.23, the cutoff frequency of this filter is between 100 Hz and 300 Hz and it has a flat transition from pass band to the block band which still has a certain amount of permeability of harmonics up to 5th order.

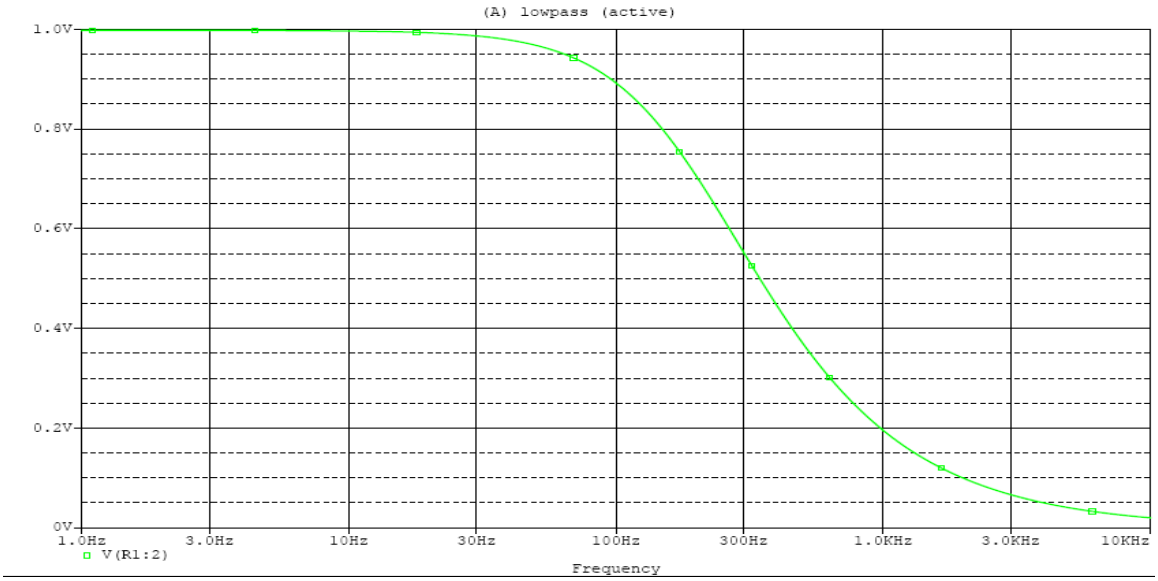

Figure 2.23 The RC low pass filter pass band and cut off frequency

Therefore, in order to solve the first problem, it is necessary to improve the filter design. The following is a frequency response of a third order Butterworth digital filter with the transfer function: $H(z) = \dfrac{0.036 + 0.0731z^{-1} + 0.0366z^{-2}}{1 - 1.3909z^{-1} + 0.5372z^{-2}}$.

The cutoff frequency of this digital filter is 70 Hz, and the transition from passing band to block band is quite sharp to permit as few high frequency components as possible. Another advantage of using digital filter is that it provides the final stage protection from noise, because any hardware components, when exposed to a high electric and magnetic fields densities, will have the chance to couple some amount of noises. The signal from Figure 2.19 is conditioned by the digital filter and then analyzed by FFT. All the harmonics and high frequency noise are effectively reduced as shown in Figure 2.25. The digital filter is implemented into an algorithm as described in Figure 2.26.

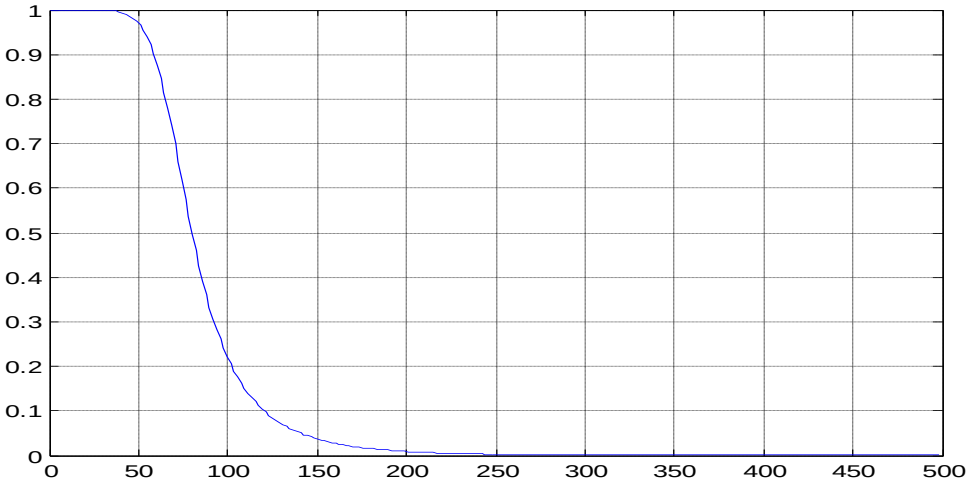

Figure 2.24 Third order Butterworth digital low pass filter

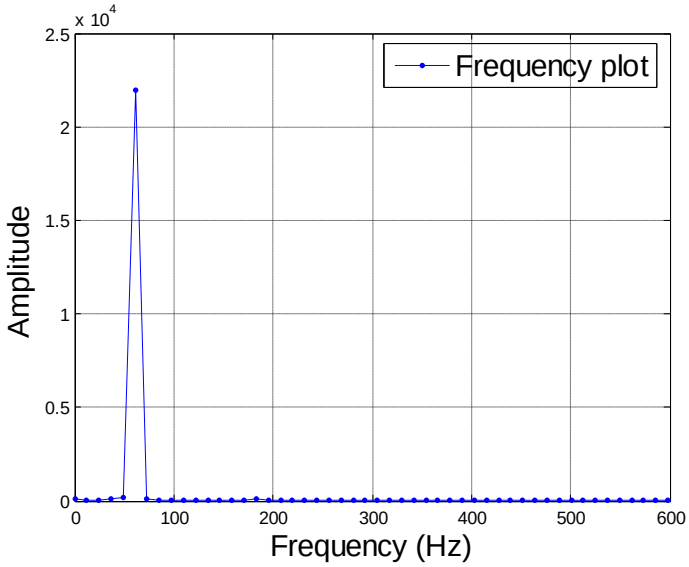

Figure 2.25 The FFT analysis for the signal after three order digital filter

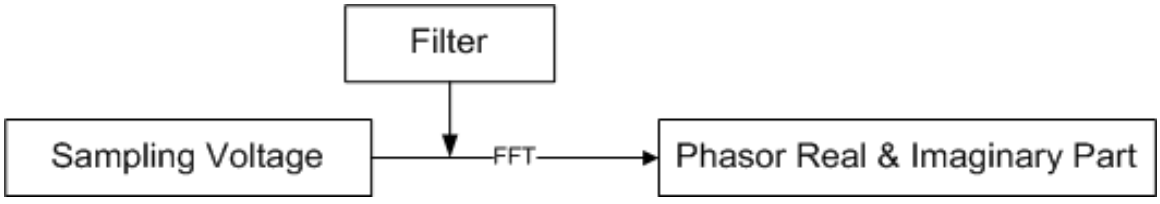

Figure 2.26 Digital filter implementation

2.6.2 Measurements in different magnetic field strength environment

The previous measurement is done at the ROW of 138 kV line. The magnetic field strength is relatively weak and less stable to obtain an accurate phasor measurement. Higher level transmission lines usually carries heavier loads so their current can produce stronger, more stable magnetic field signals. Therefore, a new location at the ROW of a 500 kV line near Exit 133 of Interstate 81, Virginia, is selected to carry on the field test. Even at the ROW of a 500 kV line, the magnetic field strength varies at different location. To further examine how field strength could influence measurement accuracy, the NFDR experiments have been conducted at two spots. 300 seconds' worth of measurement data for locations exposed in 1.1 μT and 2.6 μT magnetic field as shown in Figure 2.27 are taken into comparison.

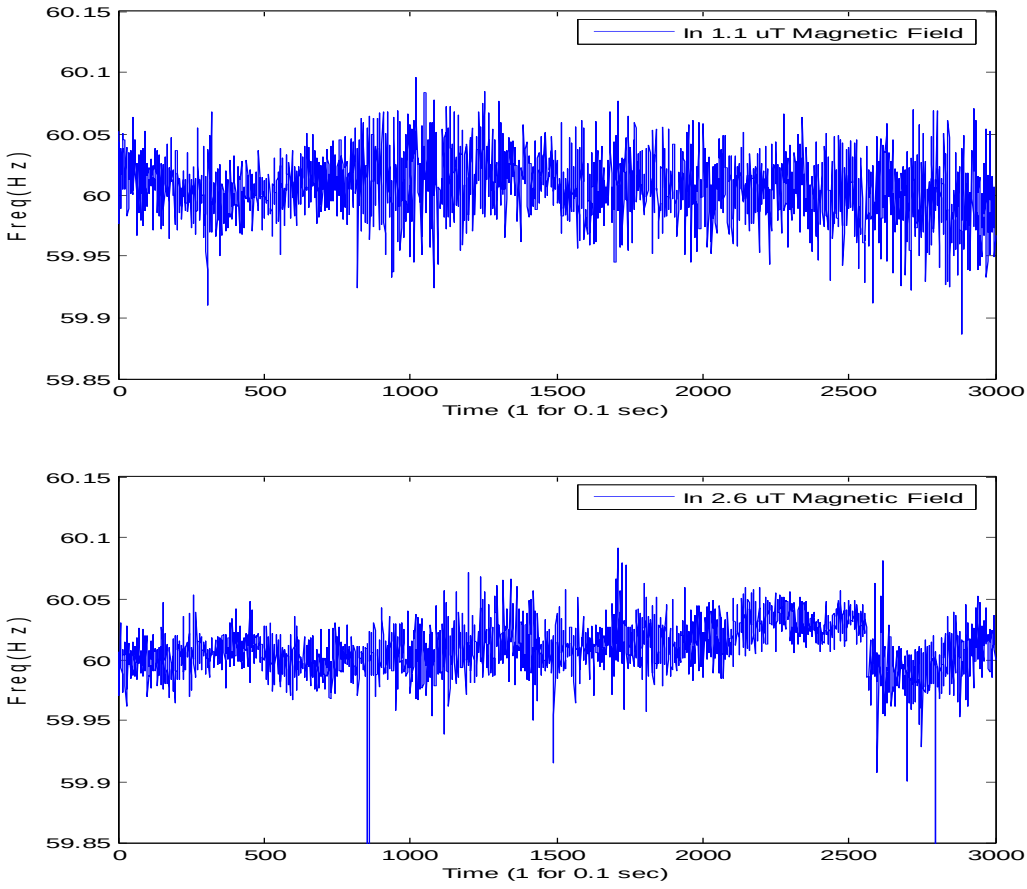

Figure 2.27 Frequency measurement at different magnetic field strength location

Unlike the laboratory test, which has a standard input signal or another frequency measurement unit using the same input source for comparison, it is hard to estimate the measurement accuracy of field data from the NFDR. However, theatrically, frequency

measurements in certain time period should have similar probability distributions throughout the same interconnection [43]. So the statistic comparison can be made for the NFDR and any other FDR measurement in the same system to estimate its frequency accuracy.

The frequency measurement data by 31 points Moving Median Filter (MMF) to distract the system frequency trend from noise [44] in order to estimate the measurement accuracy. For randomly sampled 300 seconds' worth of data, the system is assumed to operate under normal condition which means there is no oscillation information lost by applying the 31 points Moving Median Filter. Figure 2.28 presents the raw data and their 31-points moving median filtering in both 1.1 μT and 2.6 μT magnetic field environments. By subtracting the general trend from the raw data, only measurement deviation remains. Then absolute (ABS) value of the subtraction will be analyzed statistically for evaluating measurement accuracy.

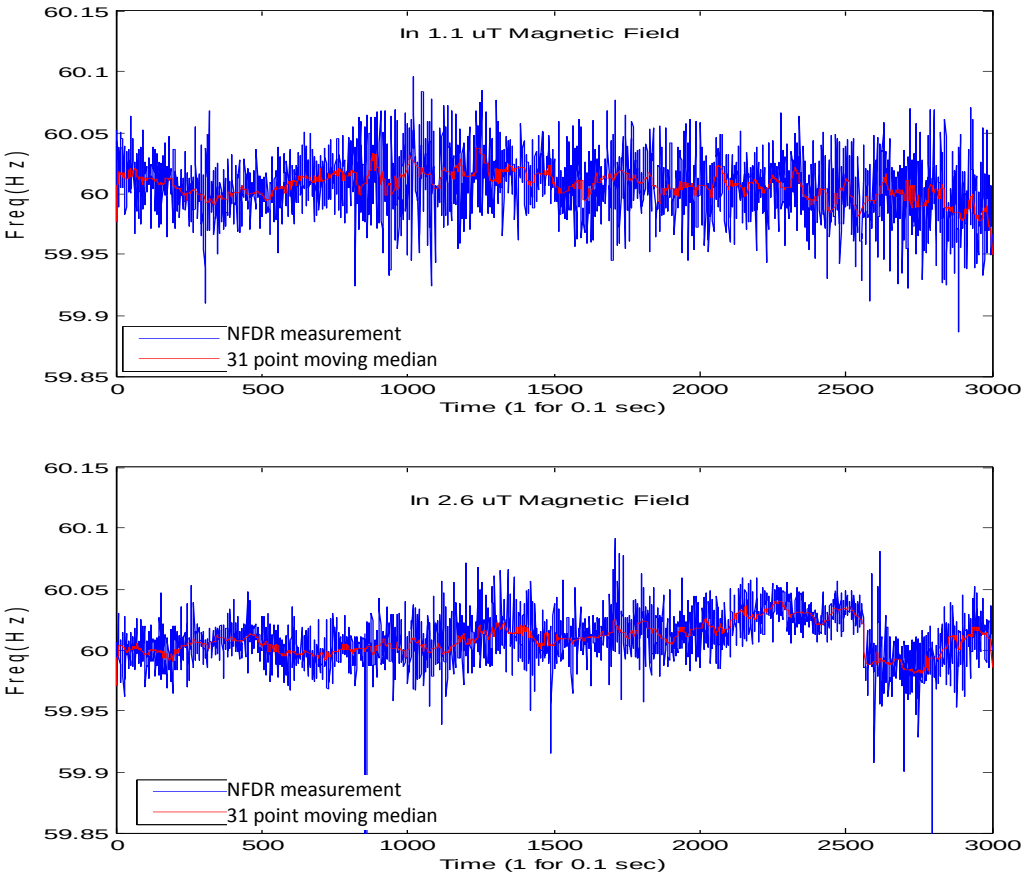

Figure 2.28 Frequency measurements and their 31 Points MMF

Figure 2.29 displays the histograms of absolute values of difference between raw data and the 31-points MMF estimated general trend. Table 2-VI and Table 2-VII present the measurement

deviation quantiles and moments. Basically, the quantiles show the percentage of data that falling into relative categories. For example, at 1.1 μT, 97.5% of the measurement deviation is smaller than 0.059 Hz and 90% are smaller than 0.038 Hz. Similarly, at 2.6 μT, 97.5% of the noise is within 0.0373 Hz and 90% are within 0.0242 Hz. The Moments table contains the average of the noises, their standard deviations and standard error means. It is easy to conclude that stronger input signals will increase measurement accuracy.

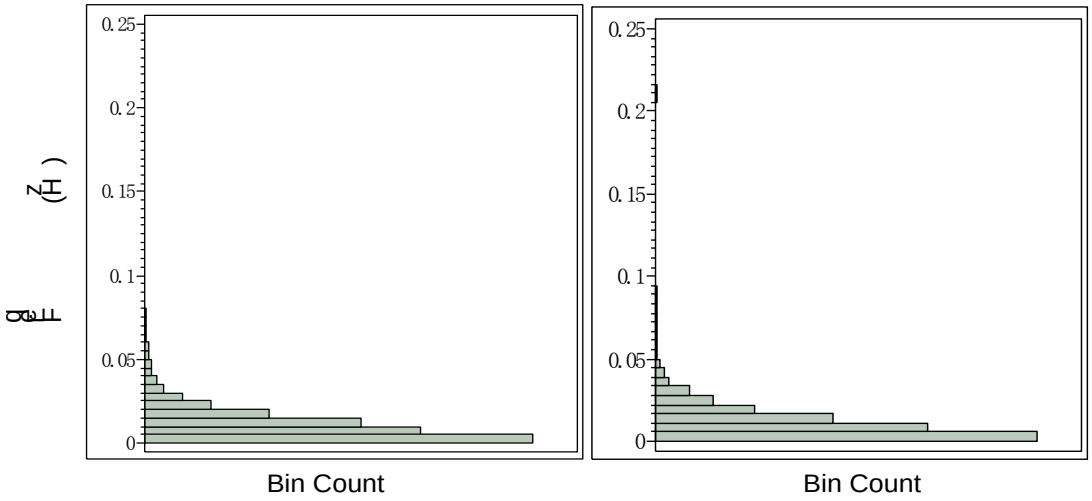

Figure 2.29 Histogram of ABS difference between raw data and 31 points MMF

Table 2-VI Quantiles of ABS difference between raw data and 31 points MMF

Quantiles					
1.1 μT			2.6 μT		
100.00%	maximum	0.098	100.00%	maximum	0.2153
99.50%		0.076	99.50%		0.0631
97.50%		0.059	97.50%		0.0373
90.00%		0.038	90.00%		0.0242
75.00%	quartile	0.025	75.00%	quartile	0.0154
50.00%	median	0.013	50.00%	median	0.0084
25.00%	quartile	0.006	25.00%	quartile	0.0036
10.00%		0.001	10.00%		0.001
2.50%		0	2.50%		0
0.50%		0	0.50%		0
0.00%	minimum	0	0.00%	minimum	0

Table 2-VII Moments of ABS difference between raw data and 31 points MMF

Moments			
1.1 μT		2.6 μT	
Mean	0.017242	Mean	0.0111642
Std Dev	0.015501	Std Dev	0.0116659
Std Err Mean	2.83E-04	Std Err Mean	2.13E-04

Figure 2.29 shows the signal analysis from the amplifier at the 2.6 μT location and its FFT analysis. Its peak-to-peak magnitude is around 16 V. Considering the A/D converters minimum signal strength requirement, which is ±7 V, this signal can provide valid measurement result. However, as mentioned in previous paragraphs, the signal strength is critical in terms of fully utilizing A/D converter digitization accuracy. Even be positioned in 2.6 μT magnetic field, signal from magnetic field sensor can only reach to 16 V_{pp}, at least 4 V less than seen in lab testing. It is necessary to improve the sensor for higher signal gain.

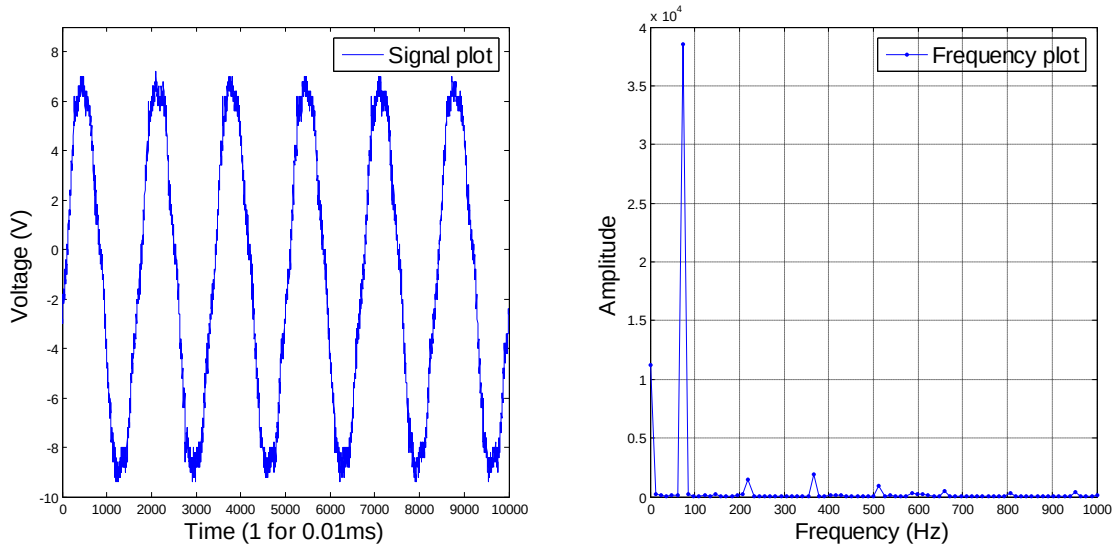

Figure 2.30 Amplifier output voltage and its FFT analysis

In its frequency plot, harmonics at the fourth, sixth, and ninth order appear. The even harmonics result for nonlinearities produced by the iron core when exposed to magnetic fields. In the following test, one of the steps of modifying the sensor design is to remove the iron core from it. The results show that even-order harmonics are reduced dramatically.

2.6.3 Improvement of sensor design

Figure 2.31 shows the type II sensor designed for field testing. Table 2-VIII gives its dimensions. It has three times the number of turns compared with the type I sensor and the iron core is no longer included. Increasing the number of turns increases the induced the voltage proportionally, and removing the iron core can eliminates the harmonics in the signal that are caused by the saturation of the core itself.

Figure 2.31 Type II sensor for field test

Table 2-VIII Type II sensor dimension

Dimension	Number of turns	Coil length	Coil diameter	
			Inner	External
Value	1000	9cm	5mm	1cm

Based on equation (4) in Chapter 2, the type II sensor can increase the signal strength by 2.5 times. But the actual signal from the output of the amplifier during field testing with the type II sensor is ±16 V. Field environment testing with the type II sensor is conducted in the same 2.6 μT location as the previous field testing.

The voltage captured from the amplifier output is shown in Figure 2.32. Its peak-to-peak value is approximately 16 V, almost the same as previous field testing using type I sensor. But from the FFT analysis it is clear that the remove of the iron core reduces the harmonic components in the signal. Same statistic analysis procedure is carried as did to the previous field testing data. ABS of the measurement deviation, which is the subtraction of the 31-points MMF from raw data, shows improved measurement accuracy compared with first field test result.

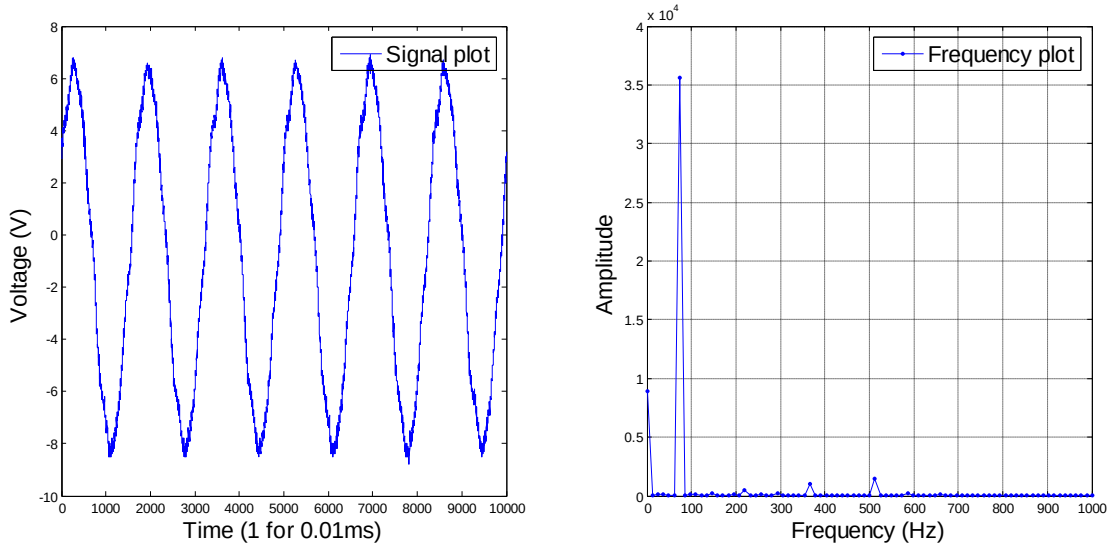

Figure 2.32 Amplifier output voltage and its FFT analysis

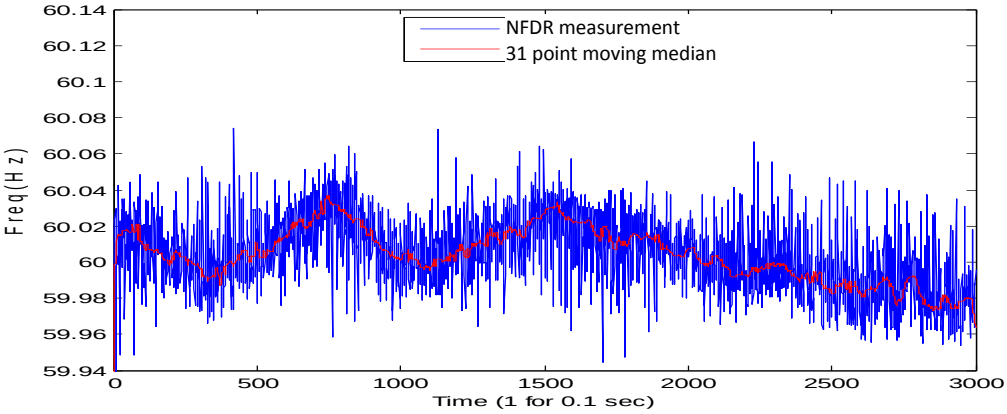

Figure 2.33 Frequency measurement with type II sensor and its 31 Points MMF

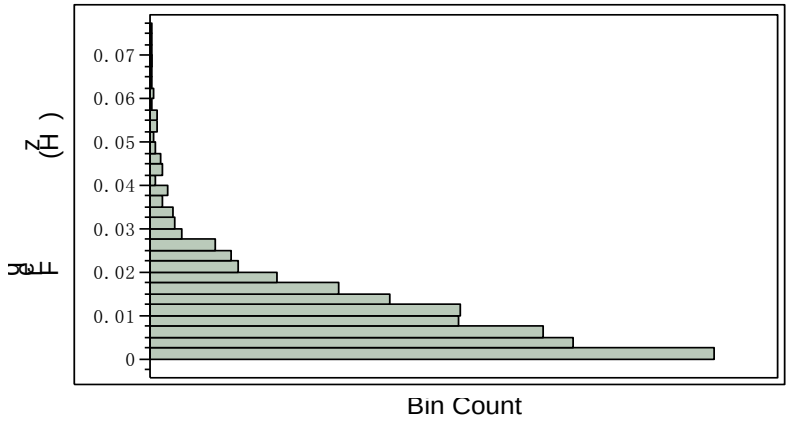

Figure 2.34 Histogram of ABS difference between raw data and 31 points MMF

Table 2-IX Quantiles of ABS difference between raw data and 31 points MMF

Quantiles		
100.00%	maximum	0.0753
99.50%		0.0598
97.50%		0.04009
90.00%		0.0235
75.00%	quartile	0.0149
50.00%	median	0.0084
25.00%	quartile	0.0036
10.00%		0.0011
2.50%		0
0.50%		0
0.00%	minimum	0

Table 2-X Moments of ABS difference between raw data and 31 points MMF

Moments	
Mean	0.01093
Std Dev	0.01048
Std Err Mean	1.91E-04

Compare with previous field testing data at 2.6 μT. The measurement deviation average decreases from 0.01116 to 0.01093, and its standard deviation decreases from 0.011665 to 0.01048.

In order to increase the induced voltage from the sensor coil, the sensor design is further improved by increasing the area of the cross section as shown in Figure 2.35. Based on calculation in chapter 2, the type III sensor is able to generate nine times the signal strength as type I sensor dose under the same condition.

As mentioned before, even if that sensor could provide a stronger signal, the maximum output from the amplifier will be within the limit of positive-negative DC power supply to amplifier. By redesigning the power supply to ±15V, the maximum peak-to-peak magnitude of the amplifier output signal could reach to ±15V.

Figure 2.35 Type III sensor for field test

Table 2-XI Type III sensor dimension

Dimension	Number of turns	Coil length	Coil diameter	
			Inner	External
Value	400	1.5cm	5mm	1cm

Figure 2.36 shows the captured amplifier output signal waveform during field testing with the type III sensor and modified amplifier power supply. Its peak-to-peak magnitude is close to 30 V. Comparing its FFT plot with the previous field test waveform's FFT plot, the ratio of the fundamental frequency component to the harmonics in the current signal is greater than before.

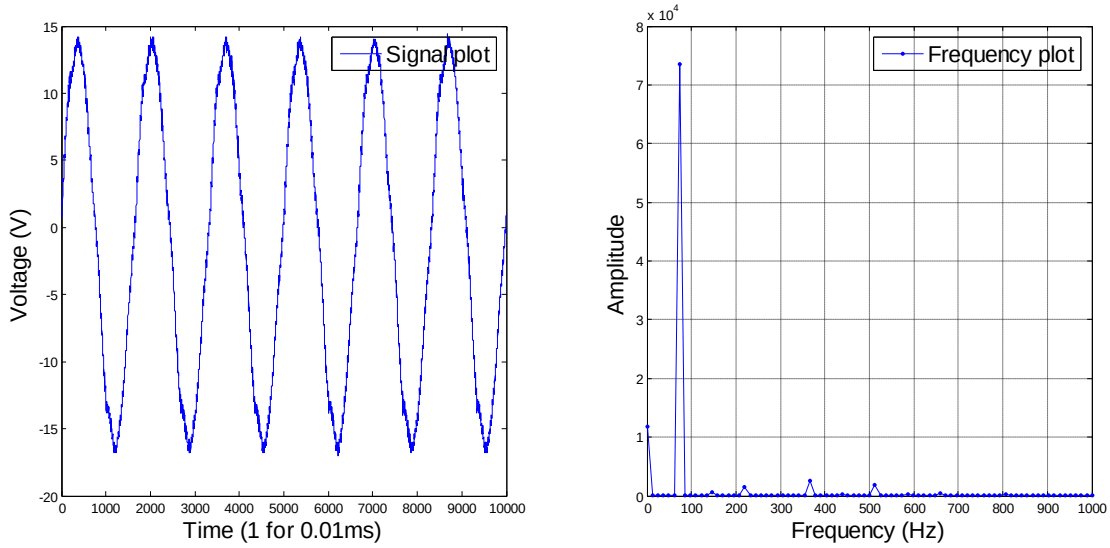

Figure 2.36 Amplifier output voltage and its FFT analysis

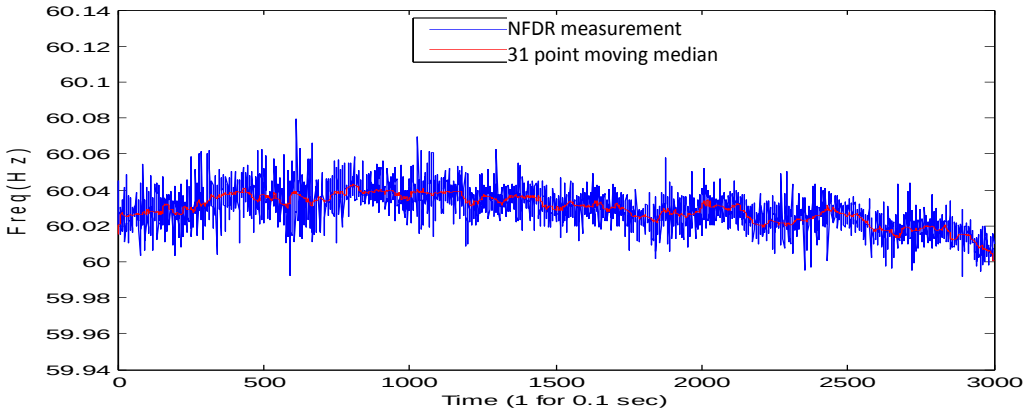

Figure 2.37 Frequency measurement with type II sensor and its 31 Points MMF

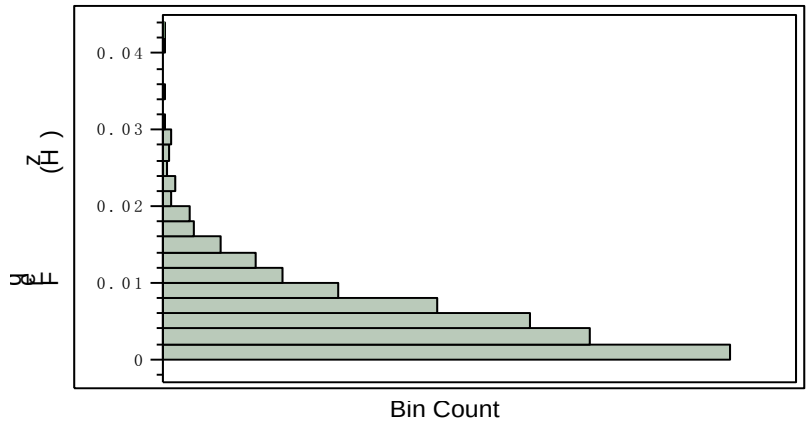

Figure 2.38 Histogram of ABS difference between raw data and 31 points MMF

Table 2-XII Quantiles of ABS difference between raw data and 31 points MMF

Quantiles		
100.00%	maximum	0.0438
99.50%		0.0285
97.50%		0.0194
90.00%		0.0128
75.00%	quartile	0.0081
50.00%	median	0.0045
25.00%	quartile	0.0019
10.00%		0.0006
2.50%		0
0.50%		0
0.00%	minimum	0

Table 2-XIII Moments of ABS difference between raw data and 31 points MMF

Moments	
Mean	0.00583
Std Dev	0.00531
Std Err Mean	9.69E-05

A similar analysis approach is applied by comparing measurement data with the 31-points MMF estimated general trend to decide the measurement deviation distribution.

Measurement accuracy increases by almost two times when just comparing average measurement deviation with the previous field test result.

Until now, the measurement accuracy of the NFDR was estimated by comparing raw data with the general trend embedded in the measurement data. This estimation is accurate based on the assumption that the embedded trend copes with the characteristic of system behavior although a few system oscillations would be eliminated as noises.

As measurement accuracy is improved gradually with hardware modification, it is now insufficient to judge measurement accuracy based purely upon the MMF estimation. We take the advantage of having FDR unit deplored in the system to monitoring the system frequency behavior. Similar as the reference selection in lab testing, a single FDR unit can be chosen as a reference and a comparison test will be used to judge the measurement accuracy of the NFDR.

Because of the frequency characteristic of an interconnected power system, it is safe to assume that the frequency from different measurement point in the system during the same time period should exhibit the same distribution.

Figure 2.39 presents the plotting of NFDR measurement data and FDR unit 13 measurement data for 300 seconds with time alignment using GPS time tagging. Figure 2.40 shows the histogram for both NFDR and FDR measurement data during the same time period. And Figure 2.41 is the quantiles to quantiles (Q-Q) plot of NFDR versus FDR measurements.

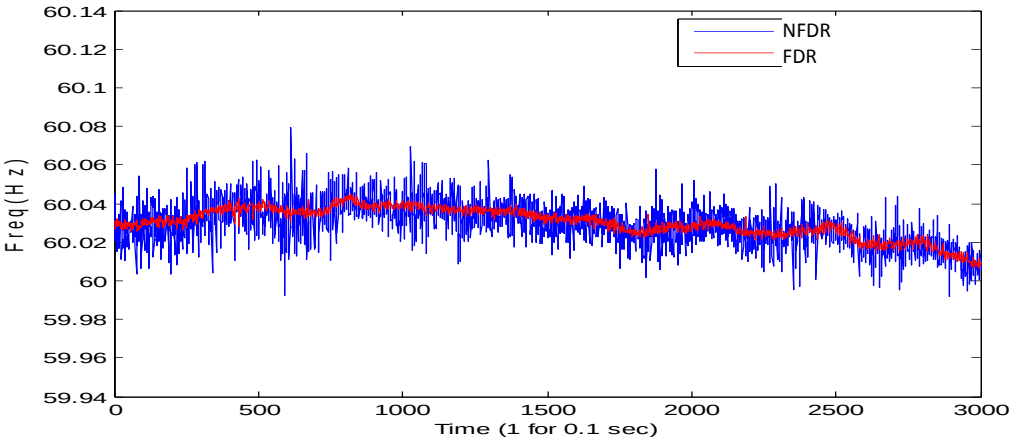

Figure 2.39 NFDR frequency measurement compare with FDR

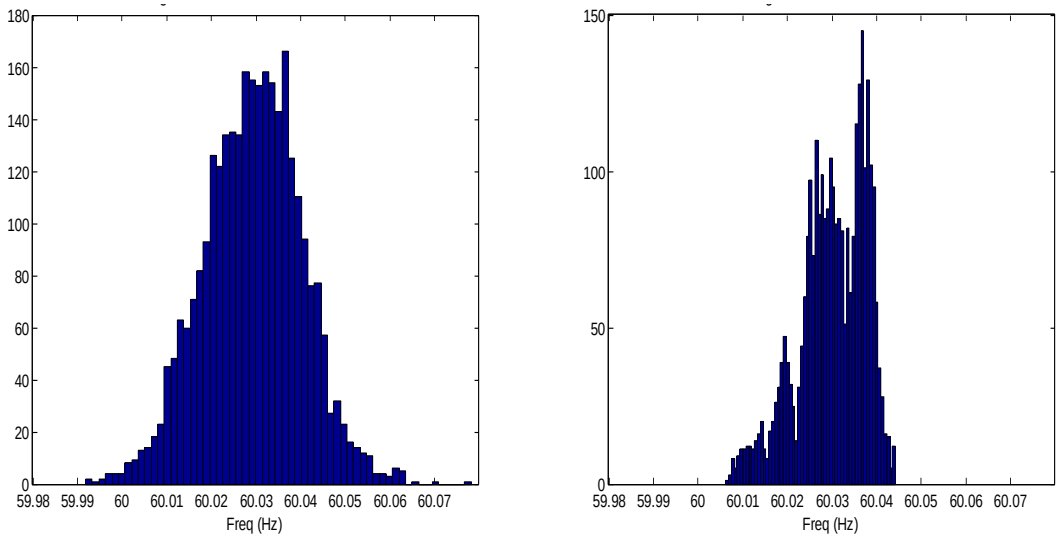

Figure 2.40 NFDR (Left) and FDR (Right)frequency measurement histogram

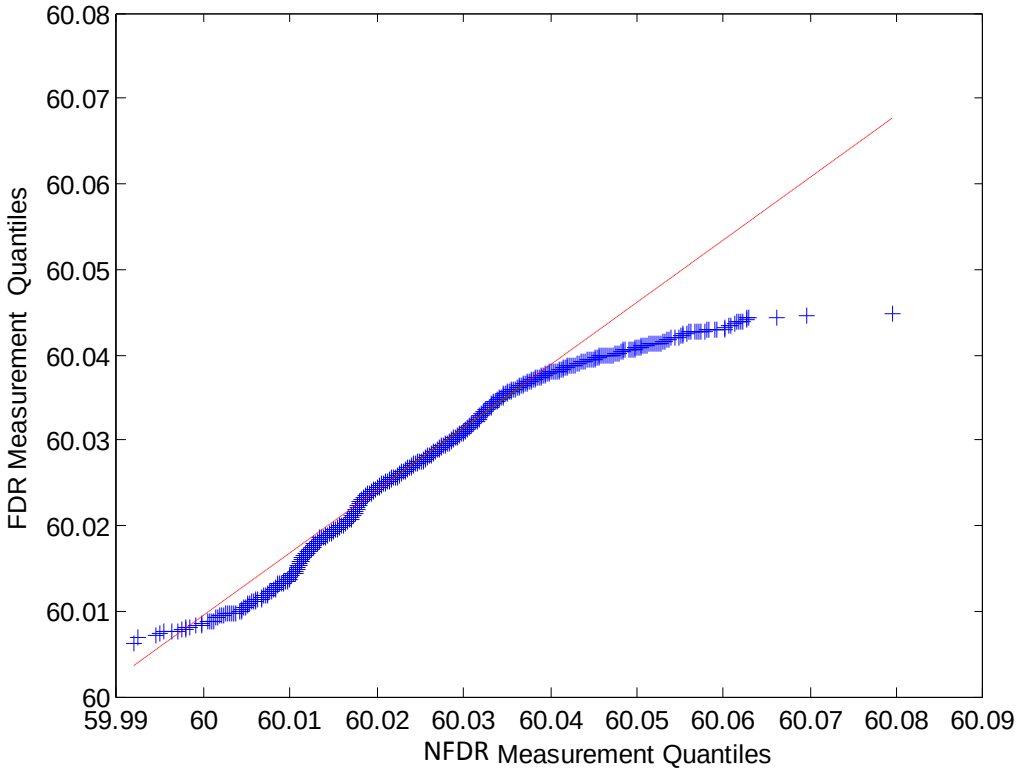

Figure 2.41 NFDR versus FDR Q-Q plotting

Form the Q-Q plotting we can tell that centered with the median of the frequency measurement, NFDR and FDR align with each other. But at both tails, they tend to be separate, mainly because NFDR measurement data contains more noises and outliers.

2.6.4 Hardware system shielding

Following the process of field testing, two major defects, harmonics and weak signal strength, were reduced. But, although the statistical analysis shows that the frequency measurement of NFDR has improved significantly, it is still not as accurate as the FDR measurements during the field testing. Whether or not continuously improve the sensor in order to get better input signal is depend on the following simulation with the current best amplifier output signal. The random noises coupled in the hardware system contribute to the remaining measurement inaccuracy. A complete software simulation using the signal that input to the A/D converter to calculate frequency is conducted.

In the simulation, the signal shown in Figure 2.36 has been input to frequency measurement software developed with Visual C++, which uses the same algorithm as the NFDR firmware. Our purpose is to locate the inaccuracy of measurement in either the signal sensing side or the firmware side.

The simulation result is plotted in Figure 2.42, and the calculated frequency are within a band of 0.000047Hz, which means that the current signal from the sensor is able generate accurate measurement results.

We notice that the simulation result is centered at 57.59999Hz. That is because the signal from the oscilloscope is discrete data obtained by the sampling rate of 100 kHz. But the input simulation software requires a sampling rate of 1440Hz. A down sampling is used. However, the frequency oscillatory band, which indicates the accuracy of the measurement, is purely decided by the signal quality.

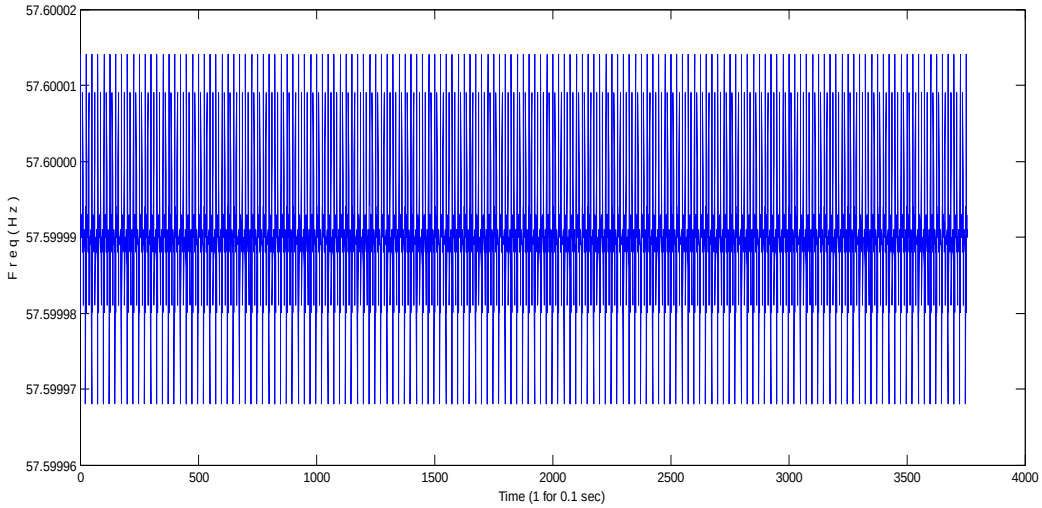

Figure 2.42 Software simulation result of field test signal

The conclusion is that the deviation of actual measurement is cause by the magnetic electrical interference on the hardware side. In order to improve the measurement accuracy, shielding design of the device is necessary. Simplified shielding is deployed in the following field testing. Magnetic sensor is shielded by wrapping with aluminum paper and the rest of the device is covered with an iron box. Bellowing is the field test result with magnetic-electric shielding for NFDR device, while Type III sensor is used.

Frequency measurement data is first been compared with 31 points MMF estimated trend, so that we can identify its accuracy improvement with respect to former field tests. The ABS value of measurement deviation is been plotted as in the form of a histogram in Figure 2.44 and quantified distributions are listed in Table 2-XIV and Table 2-XV.

The average measurement deviation compare with the general trend decreased from 0.0058 to 0.0033 Hz, almost half in magnitude, with hardware shielding.

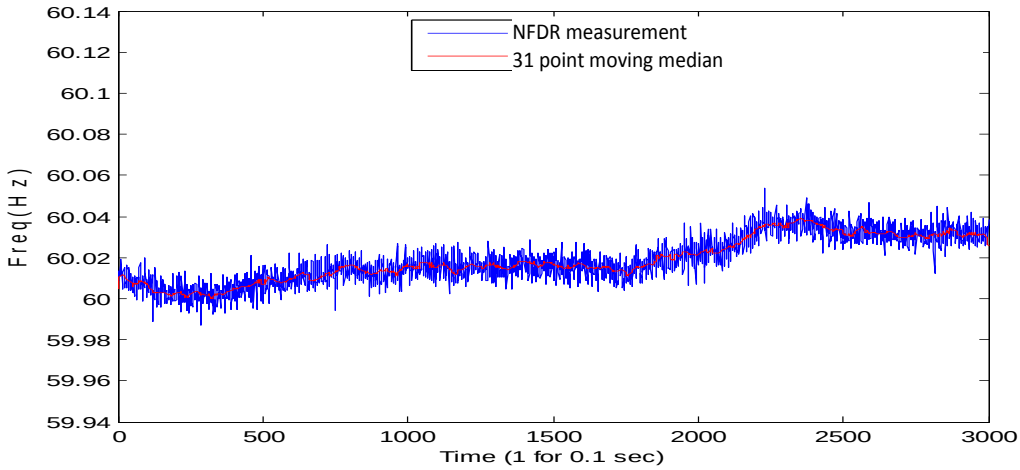

Figure 2.43 Frequency measurement with type III sensor and its 31 Points MMF

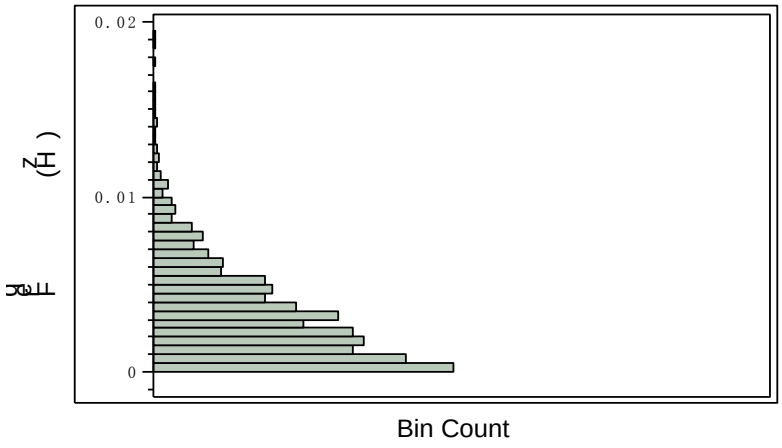

Figure 2.44 Histogram of ABS difference between raw data and 31 points MMF

Table 2-XIV Quantiles of ABS difference between raw data and 31 points MMF

Quantiles		
100.00%	maximum	0.0192
99.50%		0.014
97.50%		0.0102
90.00%		0.00719
75.00%	quartile	0.0047
50.00%	median	0.0027
25.00%	quartile	0.0012
10.00%		0.0003
2.50%		0
0.50%		0
0.00%	minimum	0

Table 2-XV Moments of ABS difference between raw data and 31 points MMF

Moments	
Mean	0.0033
Std Dev	0.00277
Std Err Mean	5.06E-05

Frequency measurement distributions during a certain period of time are compared between NFDR and FDR with GPS time alignment as plotted in Figure 2.45. Figure 2.46 displays the histogram of NFDR measurement and FDR measurement data during same time period and Figure 2.47 shows the Q-Q plot of NFDR versus FDR.

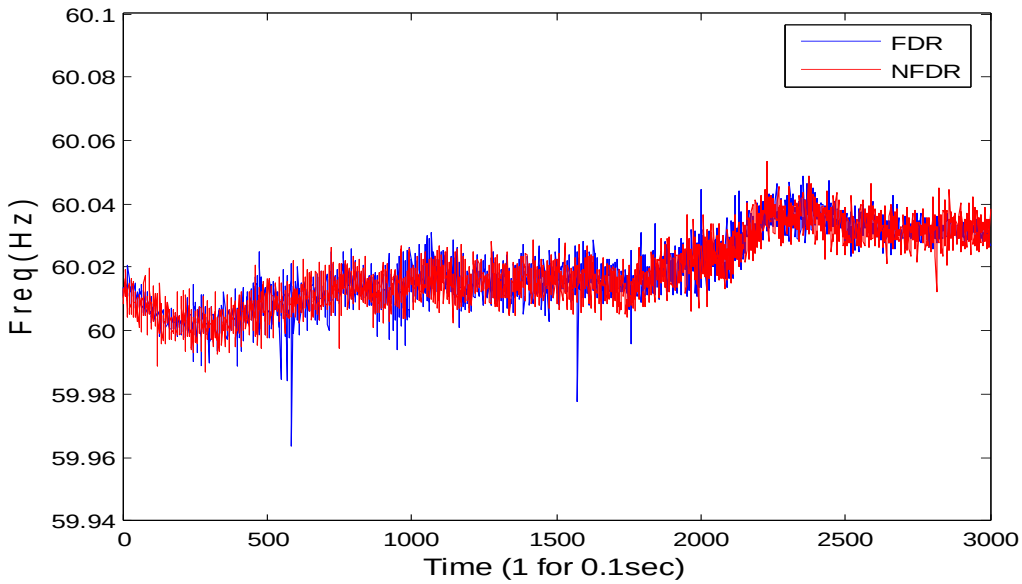

Figure 2.45 NFDR frequency measurement compare with FDR

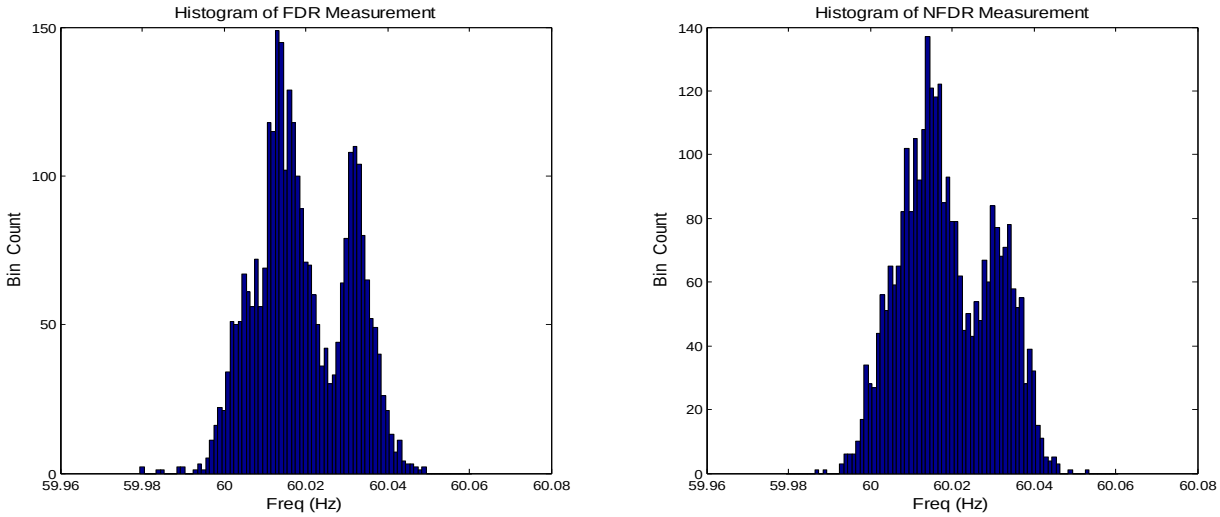

Figure 2.46 NFDR and FDR frequency measurement histogram

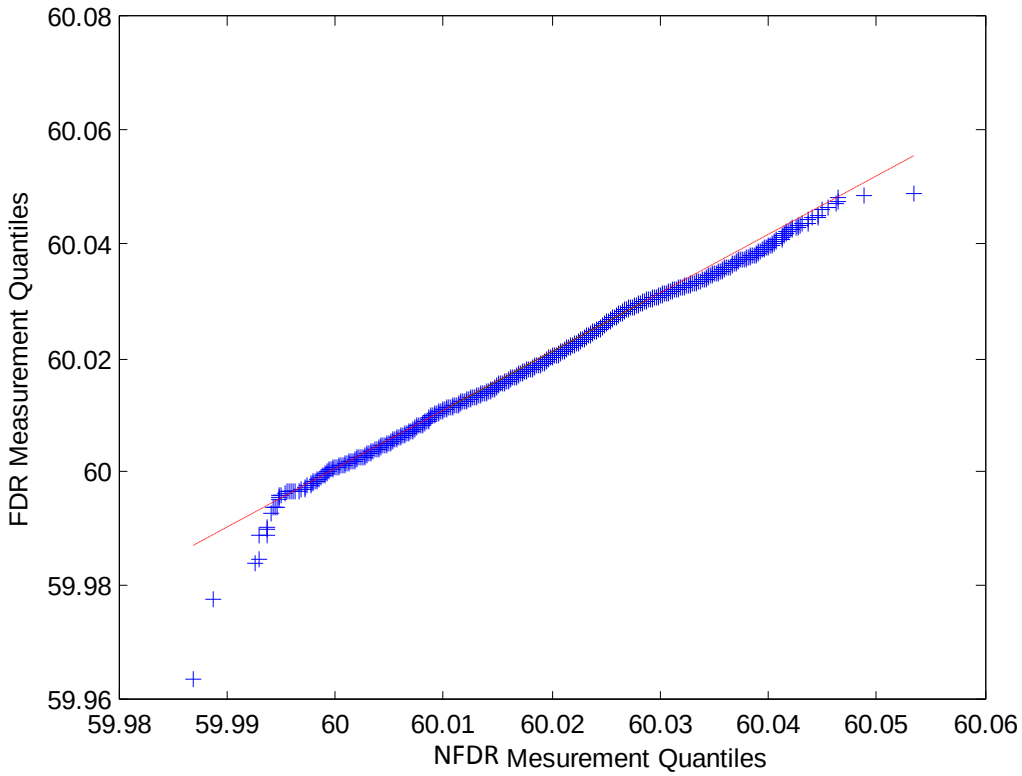

Figure 2.47 NFDR versus FDR Q-Q plotting

The Q-Q plot displays a good alignment of measurement data of NFDR and FDR in the complete range of distribution, aside from a few outliers.

We conclude from the above analysis that the current phasor measurement accuracy of the NFDR using the magnetic field is equal to that of the FDR unit directly connected to the power system.

2.7 Conclusion and future work

Results from both laboratory and field testing demonstrate that measurement of current phasors via magnetic fields is feasible. Frequency calculated from the measurement phasor has adequate accuracy for both steady-state and dynamic conditions. This finding provides a means for flexible phasor measurement at any critical point of a power grid. In the future smart grid infrastructure, non-contact phasor measurement devices can play a major role in wide-area measurement and detailed system status estimation.

Since the magnetic field surrounding transmission lines are neither generated by a single phase current or reflective of the symmetrical components of the line currents, the non-contact

frequency disturbance recorder cannot be defined as a phasor measurement unit in the traditional sense. Therefore, further investigations is needed to directly link the summation of the magnetic fields to current phasors or their symmetrical component in order to categorize the non-contact frequency disturbance recorder as a member of the PMU family.

Chapter 3 Electric field-based phasor measurement

3.1 Electric Field and the field sensor

The electric charges in the conductor of a transmission line produce an electric field in between the line itself and the ground. The electric potential difference between a transmission line and the ground is equal to the line-neutral voltage. Therefore the electric field strength is decreases with the distance away from the conductors. For simplicity, considering an infinite line conductor with a voltage of V, the electric field at distance r can be calculated with (4).

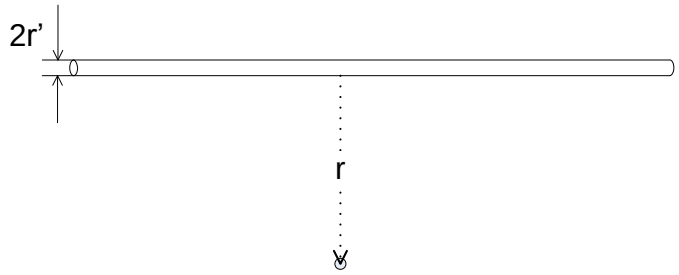

Figure 3.1 **Infinite line with a radius of *r'***

$$E = \frac{\lambda}{2\pi\varepsilon_0 r} \tag{3-1}$$

Where:

E Electric field strength

λ Electric charge density of the infinite line

r Distance from the infinite line to the monitoring point

ε_0 Permittivity of free space

The infinite line as displayed in Figure 3.1 has a radius of *r'*, its voltage can be calculated by the integration of the electric field in the radians direction, as shown in (3-2). Substitute λ back to (3-1) develops (3-3).

$$V = \int_{r'}^{r} \frac{\lambda}{2\pi\varepsilon_0 r} dr = \frac{\lambda}{2\pi\varepsilon_0} \ln(\frac{r}{r'}) \tag{3-2}$$

$$E = V / \ln(\frac{r}{r'})r \qquad (3\text{-}3)$$

In reality, transmission lines contain several conductors from three phases. Therefore, the electric field at the measurement point will be a summation of several electric fields' space vectors as demonstrated in Figure 3.2. Because of each vector is also a phasor that various in time domain, it is easy to conclude from (3-3) that the summation of values will also have a frequency of *f*. If all the sinusoidal wave forms have the same frequency, the superposition of them also remains the same frequency. This conclusion applies to more than three waveforms combined.

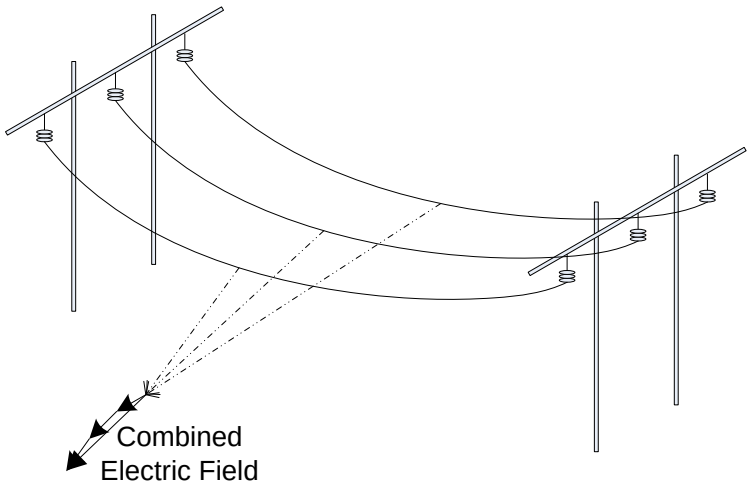

Figure 3.2 Sum of electric fields generated by three phase line voltages

The electric field strength calculation is much more complicated than a single infinite conductor. It requires knowledge of the voltage level, the line configurations, and the standards regarding right-of-way distance. Many studies have been conducted in this field and the generally accepted electric field strength at the right-of-way of 500kV transmission corridors is approximately 5 kV/m on average [45]-[59].

3.2 Non-contact FDR (NFDR) architecture

The hardware framework of electric field based NFDR is illustrated in Figure 3.3.

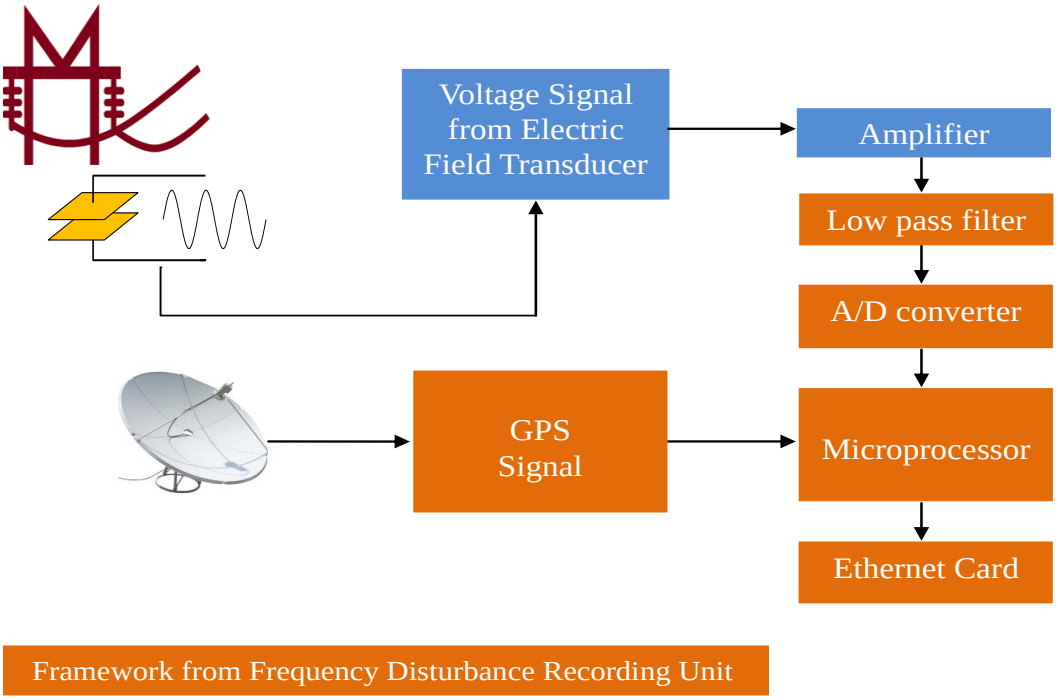

Figure 3.3 NFDR hardware structure

The NFDR is consists of a Electric field transducer, a voltage buffer amplifier, a low pass filter, an analogy to digital (A/D) converter, a microprocessor, and an Ethernet card. During the field testing, the NFDR system is powered by an uninterruptible power supply (UPS). The measurement data is collected by a laptop computer that is connected via a crossover cable. The voltage buffer amplifier is described in Figure 3.4.

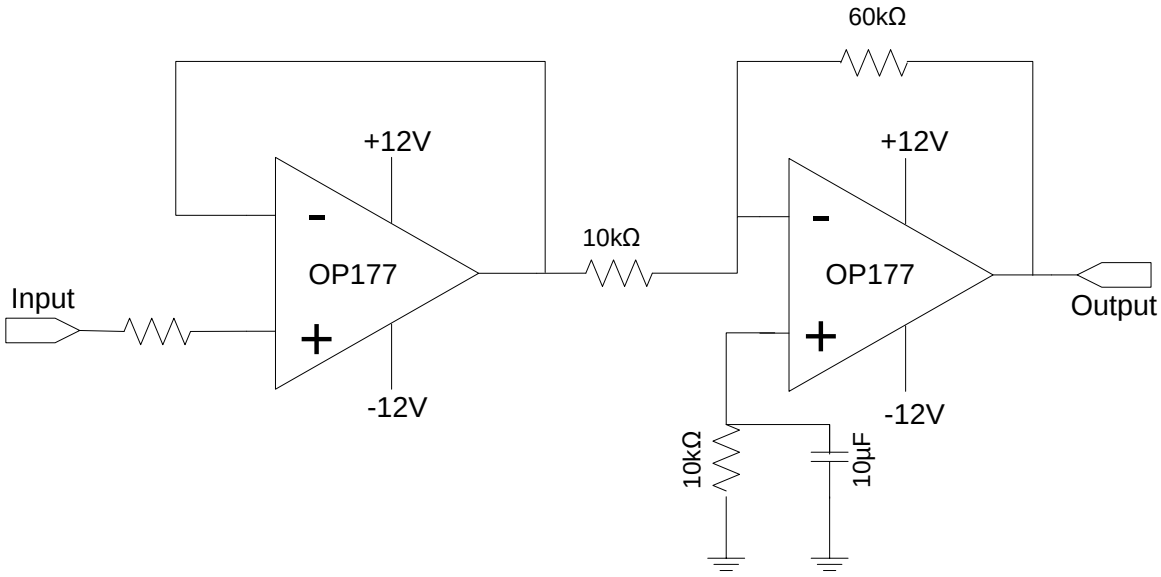

Figure 3.4 Voltage buffer amplifier connected with regular voltage amplifier

Ultimately, the NFDR could use rechargeable battery through solar power to sustain its operation and use wireless communication card to transfer data through the air. There already are commercial products for both parts.

There are two common categories of electric field sensors [60]-[70]. The Free-Body type refers to sensors that consist of two halves of isolated conductive bodies. The Ground-Reference type sensor usually refers to a flat conductor that is placed in the electric field to introduce a potential difference between the sensor and the ground. The Free-Body type of sensor is favorable in NFDR system because it is portable, allows measure above the ground, and does not require a known of ground reference.

Typical electric field meter with Free-Body type sensor measures the charging current in between the two halves of sensor, which is generated by the potential difference of the two halves. The NFDR uses a Voltage buffer amplifier to amplify the potential difference and transfer the voltage signal to the A/D converter.

3.3 NFDR laboratory testing

In order to generate a uniform electric field in laboratory environment to simulate a field that like the one found at the transmission line right-of-ways, a layout as shown in Figure 3.5 is designed.

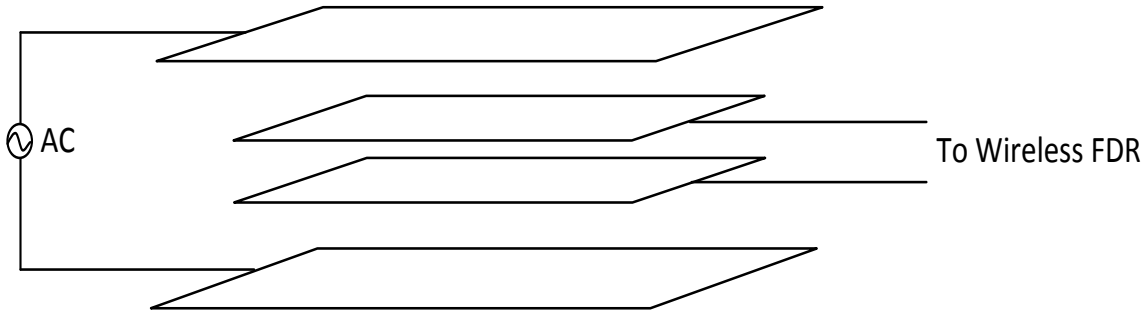

Figure 3.5 Electric field generator and sensor

Each layer in the figure represents a rectangular copper plate. The outside two copper plates, called *source plates*, are connected to the power source as such that there is a uniform electric field generated in between them. The inner two copper plates together play the role of a free-body electric field sensor. The strength of the electric field can be controlled by changing the

source voltage. The size of each copper plate is shown in Table 3-I Size of Source plate and sensor plate.

Table 3-I Size of Source plate and sensor plate

	Source copper plate	Sensor copper plate
Length (cm)	30.48	30.48
Wide (cm)	15.24	7.62

Polysulfone insulators are inserted in between each pair of copper plate. The dielectric constant can be treated the same as air insulation [71]. The distance between each plate is 0.635cm. Theoretically, the voltage that charged on the sensor is 1/3 of the voltage that applies on the source plates. However, in actuality, a 120 V AC signal must be applied to the source plates in order for the sensor to have 10 V_{pp} signal.

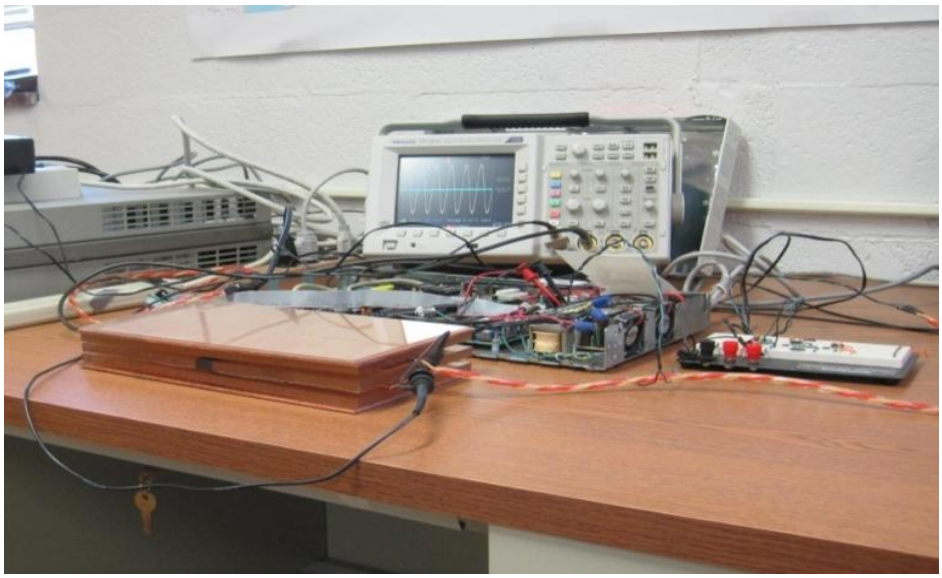

Figure 3.6 The NFDR layout in laboratory testing

Both the static and dynamic performances of the NFDR need to be examined so as to evaluate its measurement accuracy. Consequently, two scenarios of experiments are conducted.

In the first laboratory testing scenario, the source plates are connected to the output channel of a Doble 6150 power source. By adjusting the output voltage magnitude of the power source, the electric field strength is set to 10 kV/m. The frequency of the magnetic field can also be adjusted

by varying the AC source output frequency. Figure 3.7 gives an example of NFDR measurements by a segment of recordings when the input frequency is 60 Hz.

Four frequency steps, 59.90Hz, 59.98Hz, 60Hz, 60.02Hz and 60.10Hz are applied to the NFDR. Statistical analysis results of 300 seconds worth of data from each step are listed in Table II. Error is calculated by direct subtraction of the measurement average from the input signal frequency. Standard deviation of measurement data can illuminate device measurement stability and noise band.

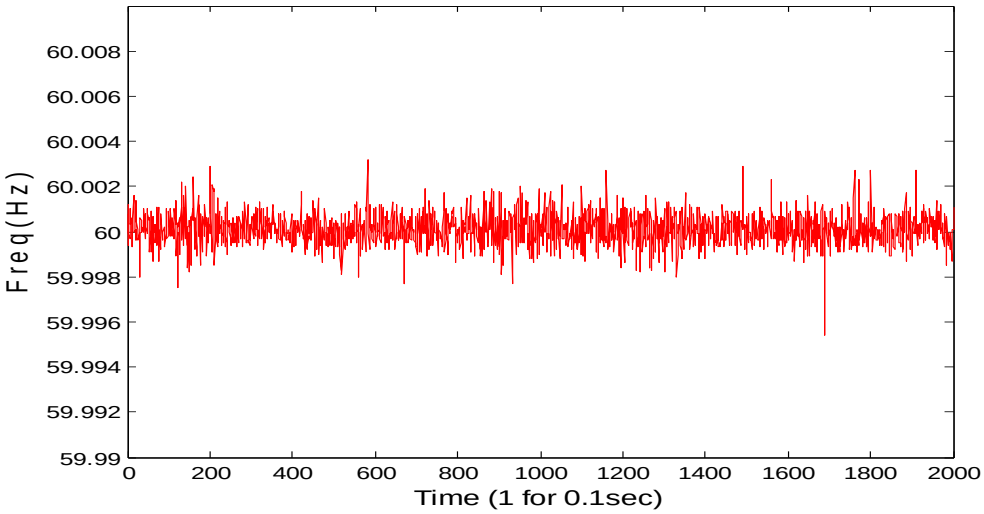

Figure 3.7 **NFDR frequency measurement using 60Hz input**

Table 3-II NFDR laboratory testing scenario one (Unit: Hz)

Input signal Frequency	Measured Average	Error	Measured Median	STD
59.90	59.900079	0.000132%	59.9001	0.000825
59.98	59.980042	0.000070%	59.9800	0.000933
60.00	60.000081	0.000135%	60.0001	0.000689
60.02	60.020053	0.000088%	60.0201	0.000960
60.10	60.100037	0.000061%	60.1001	0.000928
Error =(| Input signal frequency - Measured Average | / Input signal frequency) × 100%				

From the table, average frequency measurement errors of the NFDR tested with standard power source input are within 0.0002%. The standard deviation column indicates that nearly 70% of the measurement data varies within ±0.001 Hz from average. Those criteria satisfy the IEEE standard requirement on PMU frequency measurement accuracy.

In the second scenario, the *source plates* are connected to the 120 V wall outlet directly. Meanwhile an FDR unit is connected to the same power strip. Figure 3.8 shows the measurement data plotted for both devices. The time scale of the plot is 20 seconds. The NFDR and FDR measurements match perfectly in such a high resolution.

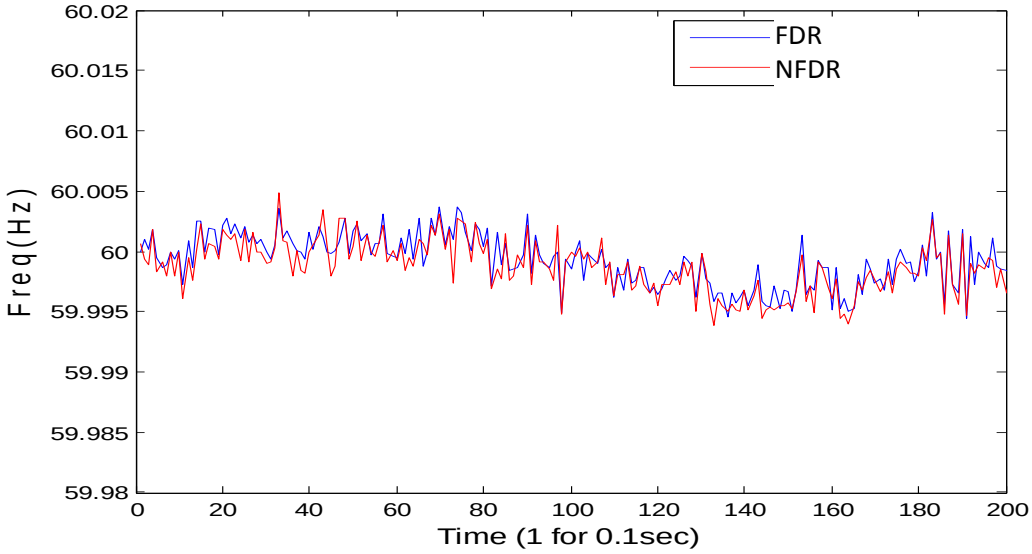

Figure 3.8 NFDR laboratory measurements compared with FDR measurements

Because of the two devices are measuring the same power source, the data can be compared directly point by point in order to estimate the accuracy of the NFDR with the FDR measurements Figure 3.9 displays the difference of each measurement between these two devices and, in order to observe the difference more directly, the absolute value of the difference.

Numerically, the average error is no longer suitable for accuracy estimation in the second scenario because there is no center line with which the NFDR can be compared. However, the Root Mean Square (RMS) of the measurement difference can reflect the average measurement error between the NFDR and the FDR measurements. The higher the RMS value, the more that their measurements differ. The standard deviation of the difference reflects the extensiveness of the difference variation.

As shown in Table III, The NFDR exhibits an average measurement difference less than 0.0012 Hz compared with the FDR. The same value applies to the standard deviation of measurement difference.

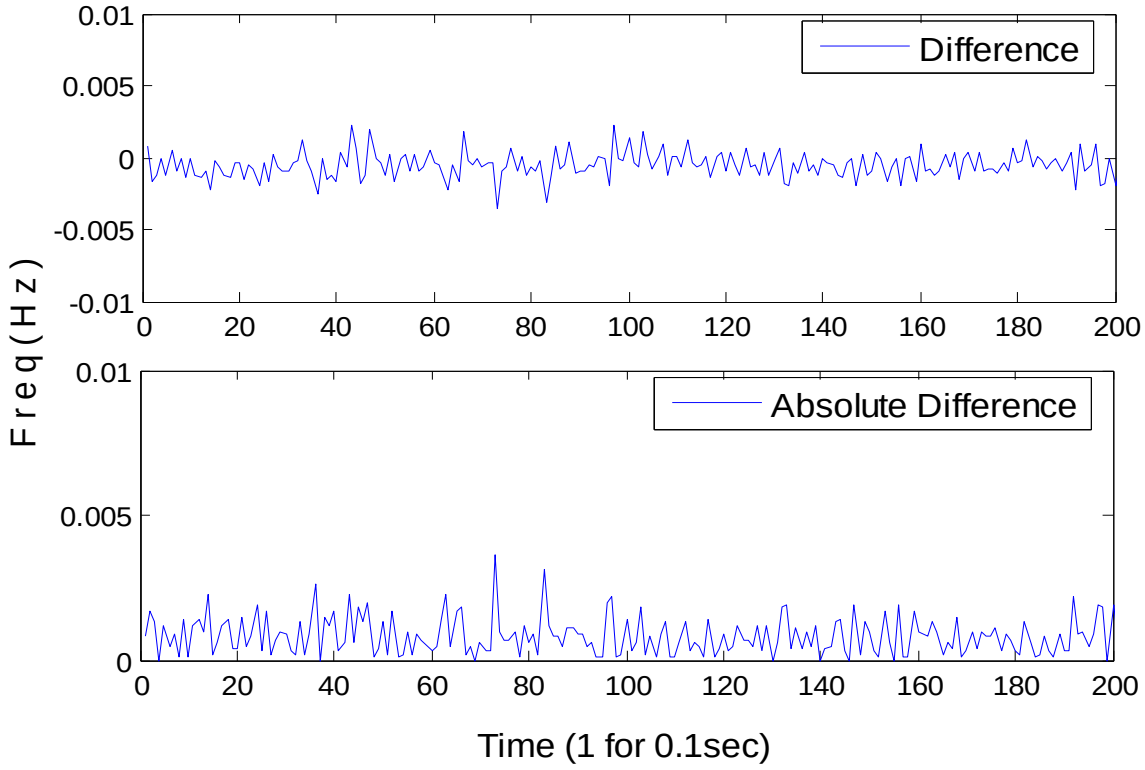

Figure 3.9 Difference of NFDR and FDR frequency measurements

Over all, the NFDR laboratory testing is successful and shows promising results. Its frequency measurement accuracy, given good signal quality, is equivalent to that of the FDR, which is more accurate than some commercial PMUs [11].

Table 3-III NFDR laboratory testing scenario one

RMS of Freq Difference	Standard Deviation of Freq Difference
0.001134595 Hz	0.00101388 Hz

3.4 NFDR field testing

In order to further test the feasibility of the proposed device, bringing it to the field environment to measure the transmission lines' electric field is essential.

The field test location is close to Exit 378 of Interstate 40 in the city of Knoxville. The NFDR device is set up in a parking space approximately at the right-of-way distance of that 500kV transmission corridor.

Field measurements are recorded by a laptop computer that is connected directly to the NFDR through a crossover Ethernet cable. Data is tagged by the GPS module with UTC time so that it can be compared with measurements of FDRs deployed in the FNET system. In other words, the NFDR measurement accuracy can be assessed by comparing with the real time North American Eastern Interconnection (EI) power grid data.

The electric field in the air near transmission lines decrease with as the distance away from the conductors. But because the distance of the two parts of the free-body sensors is fairly small, it can be assumed that the sensor is being placed in a uniform electric field environment.

The actual electric field strength measured at the ROW of this 500 kV line is approximately 1.5 kV/m. By increasing the amplifier gain ratio, the NFDR can still generate adequate measurement.

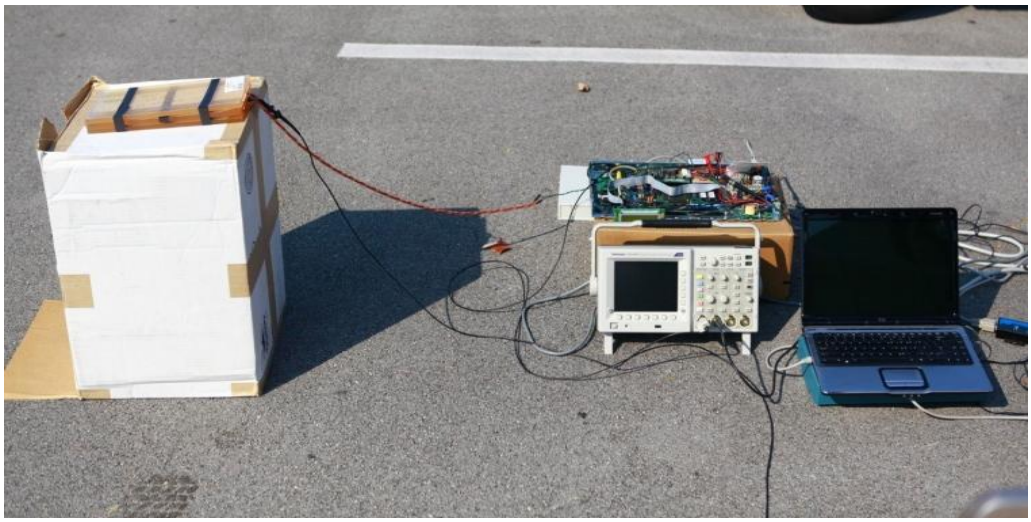

Figure 3.10 **The NFDR in field testing**

Figure 3.10 is a photograph of a NFDR taken during the field testing. As mentioned before, the NFDR is measuring a 500kV transmission line in Knoxville, Tennessee. A FDR unit located in Charleston, West Virginia is picked randomly from the FNET system to be a reference for the NFDR accuracy estimation.

Figure 3.11 shows the plot of NFDR measurements along with the chosen FDR time aligned recording. The two patterns agree with each other closely.

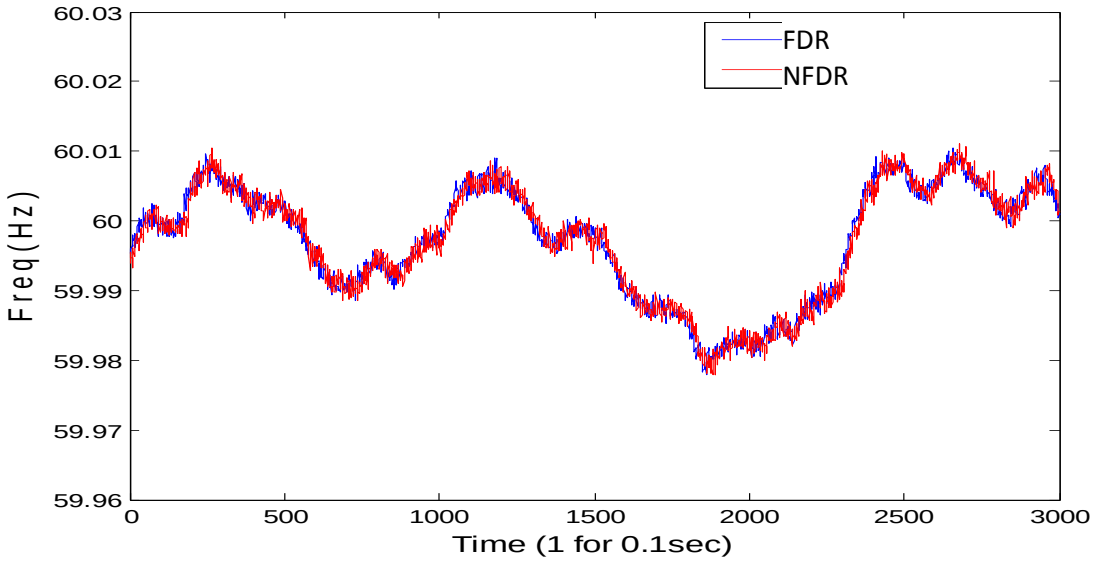

Figure 3.11 NFDR field measurements compared with FDR measurements

Since the power system frequency varies in both time and space [72], NFDR accuracy estimation by directly comparing with one of the FDRs at a different location is inappropriate. However, frequency measurements in certain time period should have similar probability distributions throughout the same interconnection.

In a 300 second time section, the NFDR and FDR measurements data have similar distributions, as shown in the histogram in Figure 3.12. The frequency interval for histogram plotting is 0.001 Hz. Both Figure 3.8 and Figure 3.11 demonstrate the notion that the NFDR frequency measurements fall into the same accuracy category as the FDR measurements.

Quantile to Quantile plotting is a useful method for comparing two distributions. The Q-Q plots of NFDR and FDR measurements as shown in Fig. 12 exhibit a strong linear characteristic.

Table 3-IV NFDR Field testing compared with FDR

RMS of Freq Difference	Standard Deviation of Freq Difference
0.001515868	0.001516015

Table VI illustrates the numerical comparison results from the perspective of the Root Mean Square and Standard Deviation methods from 300 seconds worth of data. The analysis result here can only be used as a reference because the two devices are not measuring at exactly the

same location. A similar result is expected from any two FDRs located separately in the EI system.

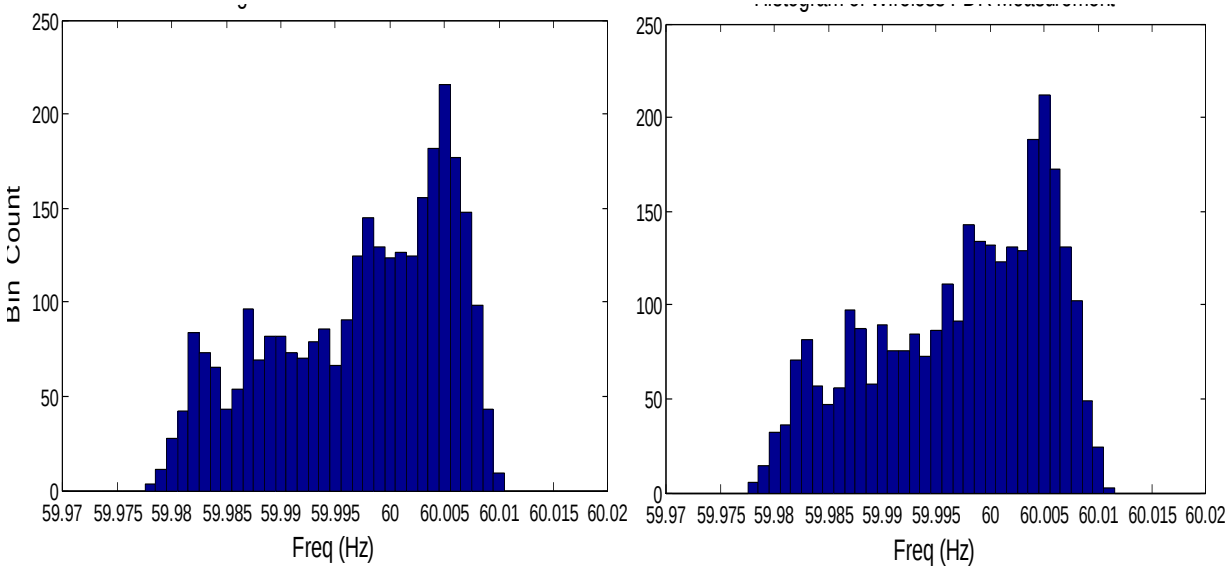

Figure 3.12 Histogram of NFDR (Right) field measurements compared with FDR (Left) measurements.

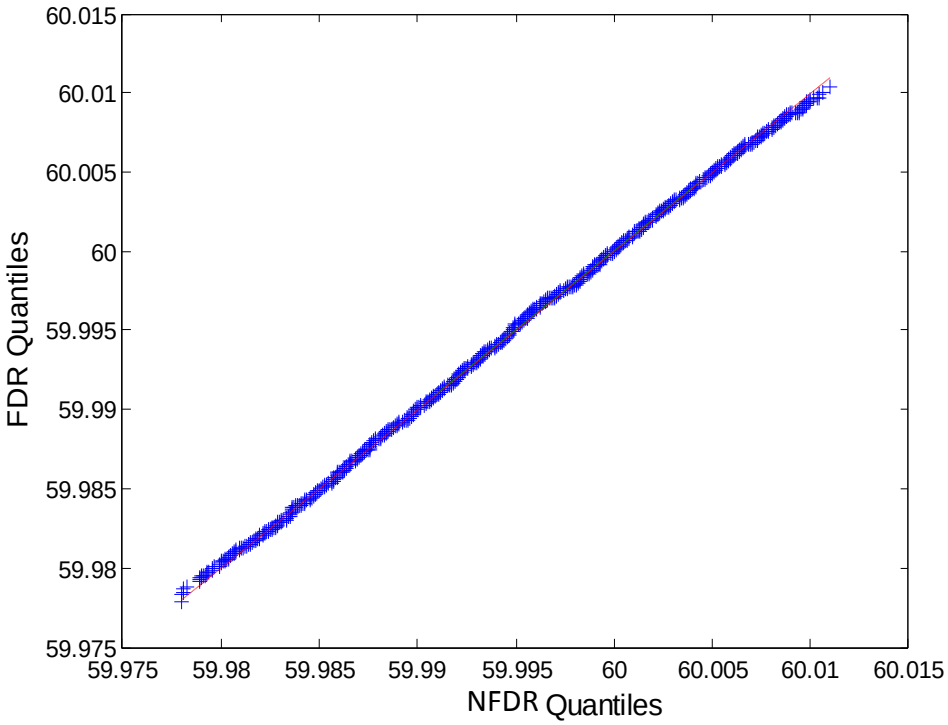

Figure 3.13 NFDR versus FDR frequency measurements Q-Q plot

3.5 Conclusion and future work

This chapter provides a non-contact power system phasor measurement method, measuring the voltage phasor through electric fields. Frequency calculated from the measured phasor has adequate accuracy for the power system real-time frequency variations. This finding provides a means for flexible phasor measurement at any critical point of a power grid. In the future smart grid infrastructure, wireless phasor measurement devices can play a major role in wide-area measurement and detailed system status estimation.

Since the electric fields in generated by transmission lines are neither created by single phase voltages and do not reflect the symmetrical components of line currents, the non-contact frequency disturbance recorder cannot be defined as a phasor measurement unit in the traditional way. Therefore, further investigations are needed to directly link the summation of the electric fields to current phasors or their symmetrical components in order to categorize the non-contact frequency disturbance recorder as part of the PMU family. Additionally, the device needs to have an integrated sustainable energy supply and wireless communications module for self-sustained field operation.

Chapter 4 Nonlinear Least Squares method used in power system frequency estimation

Researchers have been developing various techniques in power system phasor measurement and frequency estimation, due to their importance in reflecting system health. Each method has its own pros and cons regarding accuracy and speed. The DFT (Discrete Fourier Transform) based algorithm that is adopted by the FDR device particularly suitable for tracking system dynamic changes and is immune to harmonic distortions, but it has not proven to be very robust when the input signal is polluted by random noise.

This chapter will discuss the Least Mean Squares-based methods for power system frequency tracking, compared with a DFT-based algorithm.

4.1 DFT-based voltage phase angle and frequency estimation

Periodical sampling of a sinusoidal signal can be used to calculate a complex phasor because its Discrete Fourier Transform fundamental component can be written into conventional phasor representation. If the sampling is continuous, it is possible to have the magnitude and phasor angle of each cycle calculated in real time. The rate of change of the phasor angle is directly related to the input signal frequency. Essentially, the microprocessor in each FDR uses this method for frequency estimation, so does the NFDR prototype device.

Phadke et. al. in [73] introduced a DFT-based recursive method to calculate voltage phase angles and frequency. It calculates a complex phasor using the first cycle of sampled data. After that, the data window is moved point by point, meaning that whenever there is new sampling data coming in, the first data point in the window is removed. Thus, the phasor angle of each moving window can be calculated recursively. This feature of the algorithm ensures its advantage of fast angle tracking. Theoretically, the frequency can be calculated by any two consecutive angle values as well.

Jian in [74] elaborated on this method by developing practical re-sampling means to reduce the error that is associated with the sampling rate establishment. The signal sampling is based on an time interval that ensures integer sampling in each cycle under nominal frequency. If the frequency of the actual signal deviates from the nominal frequency, the accuracy of the

algorithm will be reduced. But if this estimated frequency is treated as the nominal frequency, as Jian proposed in his re-sampling scheme, a new set of sampling points can be interpolated from the actual ones. This method greatly increases the accuracy of off-nominal frequency estimation. However, it requires a data window, usually several cycles of data, for each frequency estimation rather than for each sampling point.

In order to illustrate the algorithm performance, a soft-simulator written in Matlab is used to test different input signals. As shown in its flow chart in Figure 4.1, unlike the hardware algorithm that calculates frequency every 6 cycles, it calculate frequency for each sampling points after the first 8 cycles. This is an extensive calculation that can track the signal frequency variation more closely, yet cannot be adopted by the current hardware framework.

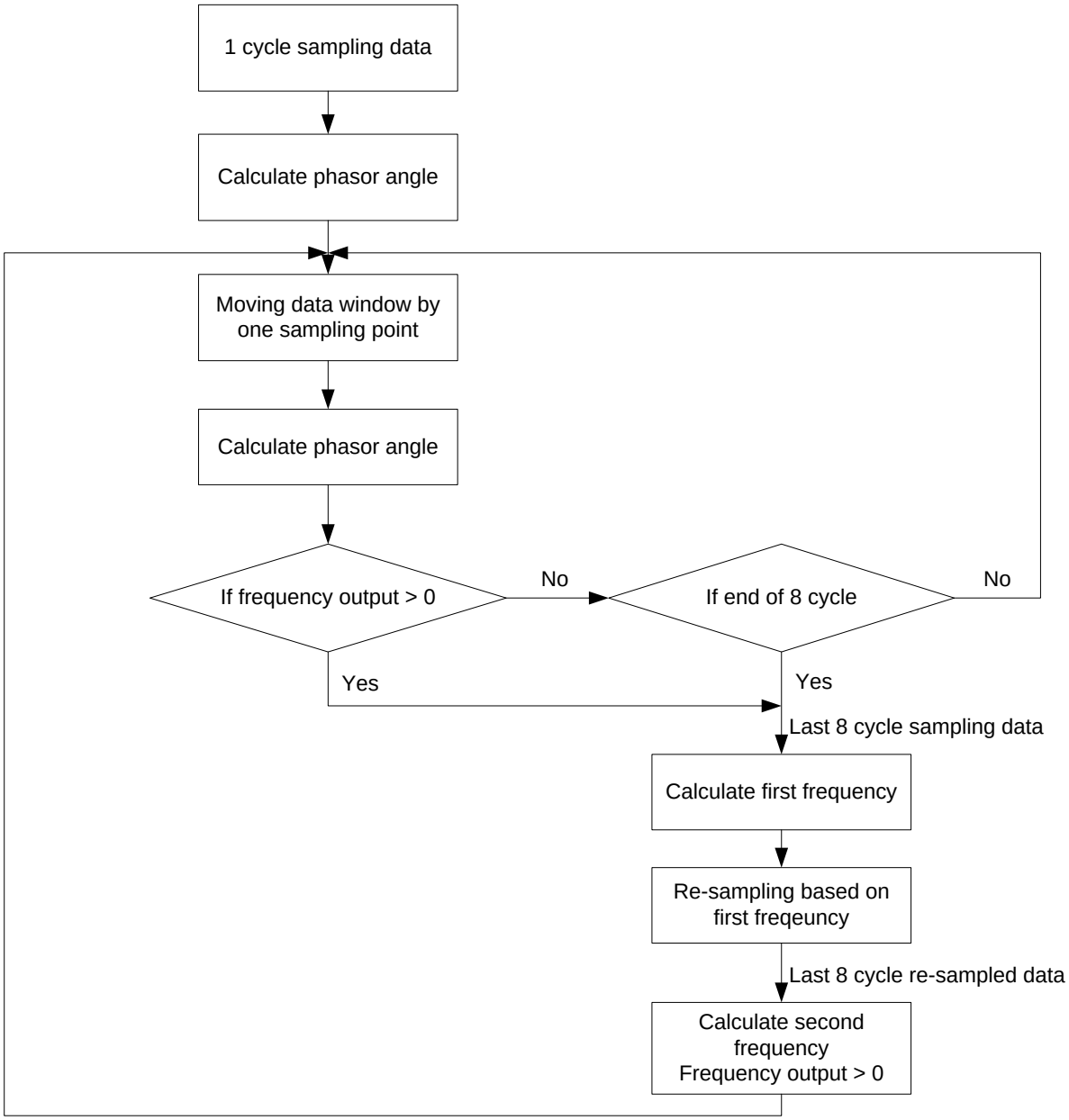

Figure 4.1 Flow chart of DFT-based frequency tracking algorithm

Theoretically, the algorithm has no error when the measured signal is purely sinusoidal at the nominal frequency, as shown in Figure 4.2. Both the first frequency estimation and the final frequency estimation after re-sampling have very accurate calculation results.

When the measured signal is no longer at the nominal frequency, an error with a sinusoidal pattern starts to show up in the first frequency calculation. This error will be compensated for greatly after the re-sampling scheme, demonstrated in Figure 4.3. Table 4-I listed the frequency calculation accuracy with different input signals. Overall, this algorithm exhibits very good

measurement accuracy, considering that the power system frequency will not be vary much from the nominal value under normal operating conditions. As mentioned before, this algorithm has the advantage of fast tracking frequency dynamics in the input signal. Figure 4.4 and Figure 4.5 display the algorithm response of a frequency step change in the input signal from 59.7 Hz to 59.5 Hz, which occurs at 5 seconds from the beginning of the signal. The estimated frequency by the algorithm starts to follow the change at 5 second and finishes at 5 seconds + 8 cycles, where 8 cycles is the calculation window size.

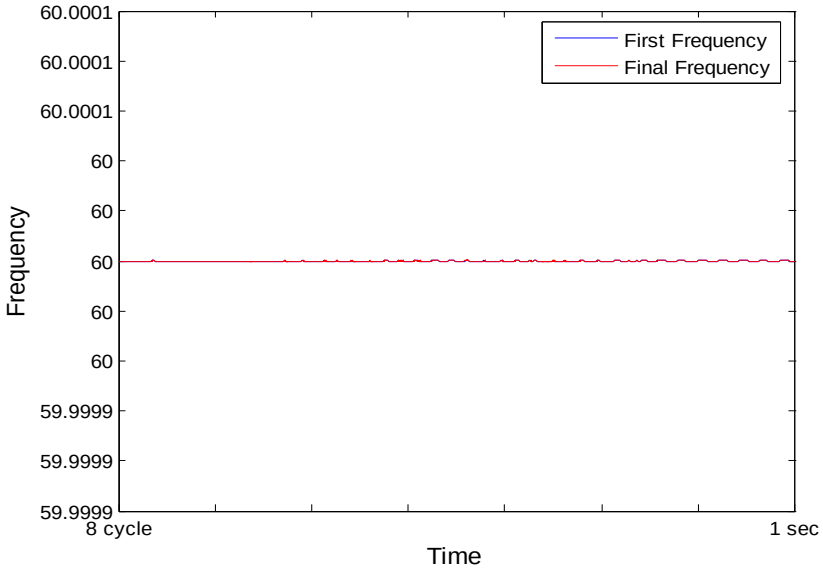

Figure 4.2 Frequency estimation by DFT algorithm when input signal is 60Hz pure sinusoidal

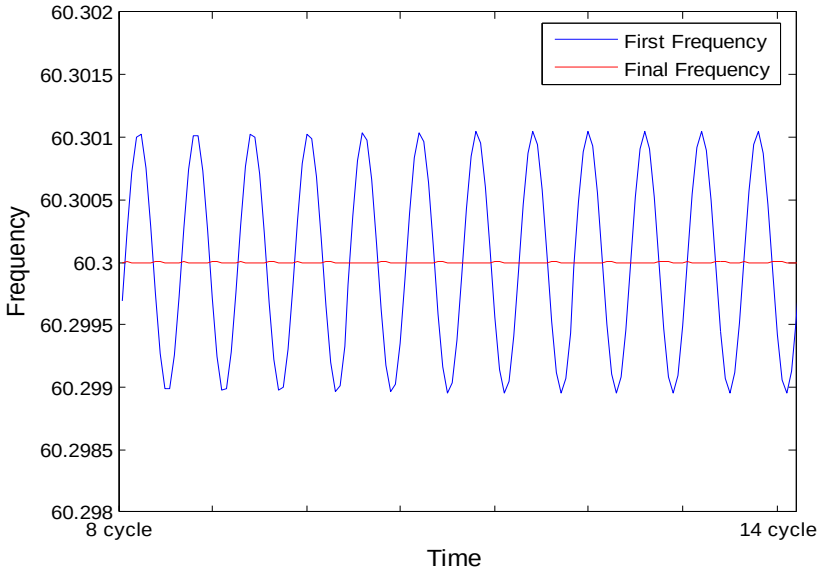

Figure 4.3 Frequency estimation by DFT algorithm when input signal is 60.3Hz

Table 4-I Frequency estimation result by DFT based method with different input signals (Hz)

Input Signal		Average	Median	Max	Min	STD
59.700000	First Frequency	59.700002	59.700005	59.700736	59.699262	0.000521
	Final Frequency	59.700000	59.700000	59.700001	59.699999	0.000001
60.000000	First Frequency	60.000000	60.000000	60.000000	60.000000	0.000000
	Final Frequency	60.000000	60.000000	60.000000	60.000000	0.000000
60.300000	First Frequency	60.300002	60.300003	60.301049	60.298950	0.000742
	Final Frequency	60.299999	60.299999	60.300001	60.299997	0.000001

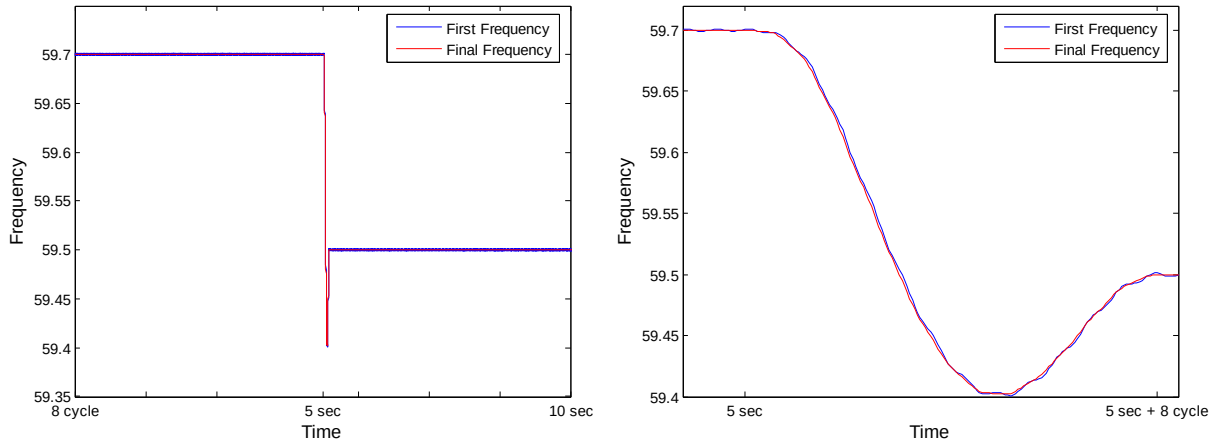

Figure 4.4 Frequency step change at 5 sec: Algorithm response (left) and Zoom in (right)

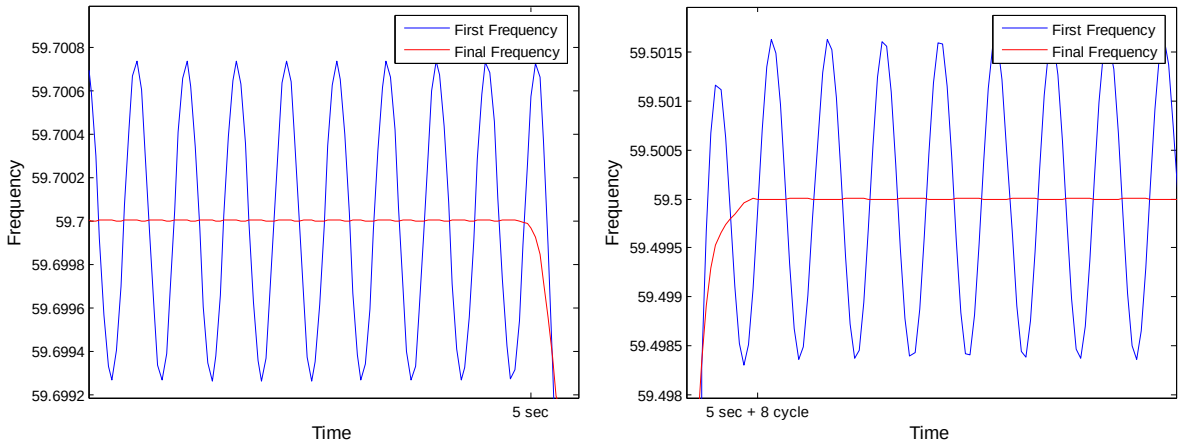

Figure 4.5 Zoom in before frequency change (left) and after frequency change (right)

However, this algorithm will suffer great loss of accuracy when the input signal is polluted by noise. Gaussian white noise with different signal-to-noise ratios (SNR) have been added to the same 59.7 Hz sinusoidal signal tested above; the frequency calculation results by the DFT-based algorithm are plotted in Figure 4.6 and analyzed in Table 4-II .

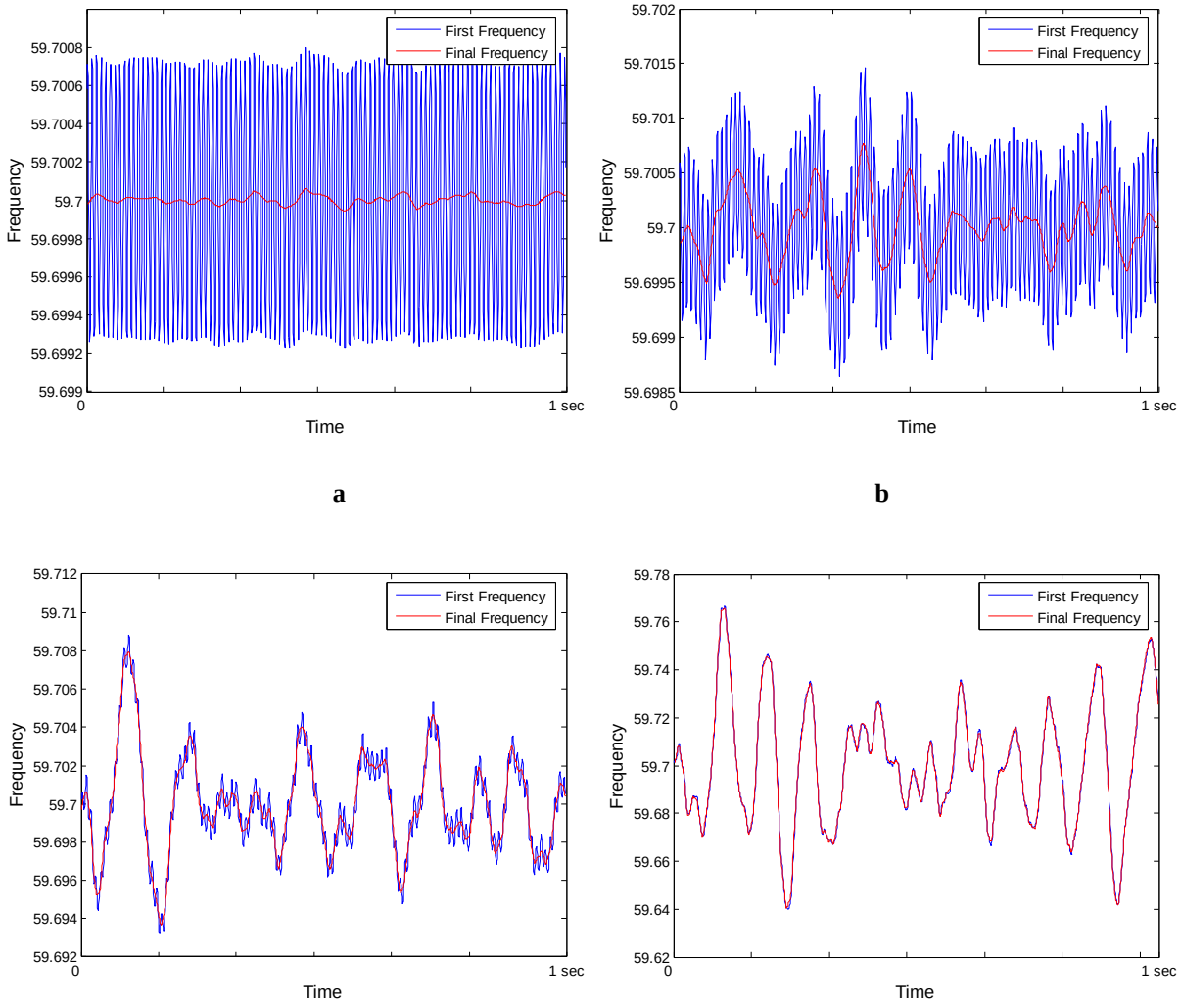

Figure 4.6 Frequency estimation result when the signal is polluted by Gaussian white noise with different signal-to-noise ratio: 80dB (a), 60dB (b), 40dB (c), and 20dB (d)

Table 4-II Frequency estimation result when the signal is polluted by Gaussian white noise (Unit if not specified is Hz)

SNR		Average	Median	Max	Min	STD
80 dB	First Frequency	59.700001	59.700029	59.700778	59.699225	0.000522
	Final Frequency	59.700000	59.700000	59.700046	59.699951	0.000021
60 dB	First Frequency	59.700000	59.699997	59.701218	59.698756	0.000572
	Final Frequency	59.699999	59.700000	59.700492	59.699454	0.000234
40 dB	First Frequency	59.699983	59.699762	59.708798	59.693269	0.002651
	Final Frequency	59.699982	59.699763	59.707927	59.693645	0.002576
20 dB	First Frequency	59.699160	59.700956	59.749006	59.649960	0.023062
	Final Frequency	59.699196	59.701246	59.747396	59.651000	0.022696

4.2 Linear Least Squares technique

Many sources [74]-[76] refer to this frequency tracking technique as the Least Error Square technique. However, this method is based upon the Taylor Series expansion of a sinusoidal wave form. In order to make a distinction between this and the method that is proposed later this chapter, this technique will be referred to as the Linear Least Squares method.

A single frequency sinusoidal voltage signal as represented in (4-1) can be treated as function of variable f at a certain time t_1. Also it is commonly acceptable that frequency f cannot be too far various from the system nominal frequency, f_0. Therefore $\sin 2\pi ft$ and $\cos 2\pi ft$ can be expanded by their Taylor Series centered around f_0. The result as shown in (4-2) takes the first three terms of the Taylor Series expansion.

$$v(t) = V_m \sin(2\pi ft + \theta) = V_m \cos\theta \sin 2\pi ft + V_m \sin\theta \cos 2\pi ft \quad (4\text{-}1)$$

$$v(t_1) \approx a_{11}x_1 + a_{12}x_2 + a_{13}x_3 + a_{14}x_4 + a_{15}x_5 + a_{16}x_6 \quad (4\text{-}2)$$

There are six variables in this equation, where:

$$x_1 = V_m \cos\theta$$

$$x_2 = (f - f_0)V_m \cos\theta$$

$$x_3 = V_m \sin\theta$$

$$x_4 = (f - f_0)V_m \sin\theta$$

$$x_5 = \left(-\frac{(2\pi)^2}{2} f^2 + (2\pi)^2 ff_0 - \frac{(2\pi)^2}{2} f_0^2\right)V_m \cos\theta$$

$$x_6 = \left(-\frac{(2\pi)^2}{2} f^2 + (2\pi)^2 ff_0 - \frac{(2\pi)^2}{2} f_0^2\right)V_m \sin\theta$$

The coefficients $a_{11}\ldots a_{16}$ can be calculated by:

$$a_{11} = \sin(2\pi f_0 t_1),\ a_{12} = 2\pi t_1 \cos(2\pi f_0 t_1),\ a_{13} = \cos(2\pi f_0 t_1),\ a_{14} = 2\pi t_1 \sin(2\pi f_0 t_1)$$

$$a_{15} = t_1^2 \sin(2\pi f_0 t_1),\ a_{16} = t_1^2 \cos(2\pi f_0 t_1)$$

The voltage signal can be obtained by measurement sampling with a constant time interval. Assuming that there are n voltage points sampled, (4-2) can be written into Matrix form as:

$$\mathbf{AX} = \mathbf{V} \tag{4-3}$$

Where:

$$\mathbf{A} = \begin{bmatrix} a_{11}, a_{12}, a_{13}, a_{14}, a_{15}, a_{16} \\ a_{21}, a_{22}, a_{23}, a_{24}, a_{25}, a_{26} \\ . \quad . \quad . \quad . \quad . \quad . \quad . \\ a_{n1}, a_{n2}, a_{n3}, a_{n4}, a_{n5}, a_{n6} \end{bmatrix}, \ \mathbf{X} = \begin{bmatrix} x_1 \\ x_2 \\ \cdots \\ x_6 \end{bmatrix}, \ \mathbf{V} = \begin{bmatrix} v_1 \\ v_2 \\ \cdots \\ v_n \end{bmatrix}$$

The minimum number of *n* required to solve for $\mathbf{X}$ is 6. However, more than n equations are typically used to solve $\mathbf{X}$ as a Linear Least Squares problem according to (4-4) in order to achieve higher accuracy.

$$\mathbf{X} = \left[\left[\mathbf{A}^{\mathbf{T}} \mathbf{A} \right]^{-1} \mathbf{A}^{\mathbf{T}} \right] \mathbf{V} \tag{4-4}$$

Since that there are only two variables *f* and θ unknown in the vector $\mathbf{X}$, multiple methods can be deployed to calculate *f* independently .

Method 1: $f = \frac{x_2}{x_1} + f_0$

Method 2: $f = \frac{x_4}{x_3} + f_0$

Method 3: $f = \sqrt{\frac{{x_2}^2 + {x_4}^2}{{x_1}^2 + {x_3}^2}} + f_0$

This algorithm is tested by a 59.7 Hz pure sinusoidal signal generated by Matlab. The calculation results for all three methods are demonstrated in Figure 4.7.

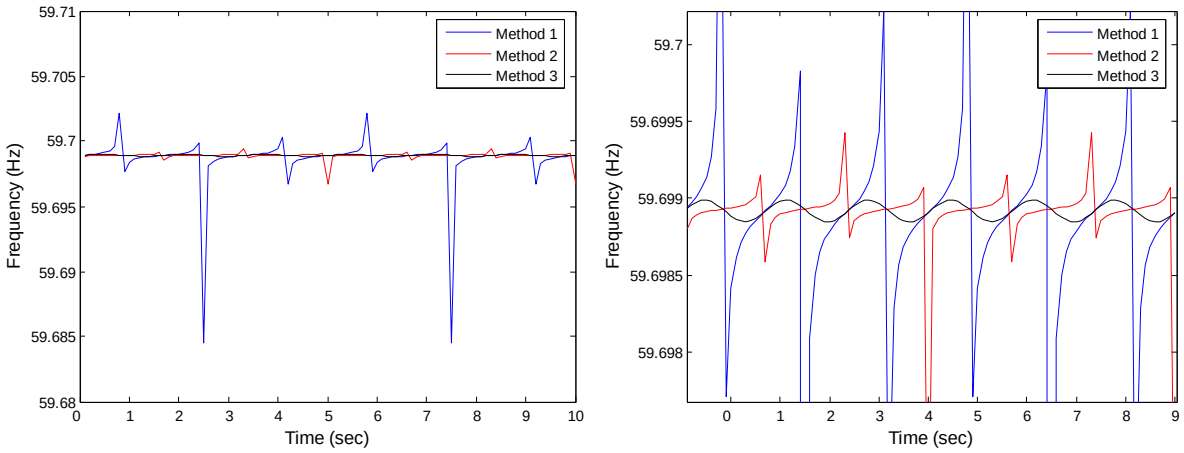

Figure 4.7 Frequency calculations by Linear Least Squares methods (original on the left and zoom in on the right)

Table 4-III Frequency estimation accuracy by Linear Least Squares methods

	Average	Median	Max	Min	STD
Method 1	59.698650	59.698903	59.702116	59.684484	0.002144
Method 2	59.698890	59.698930	59.699428	59.696691	0.000333
Method 3	59.698918	59.698918	59.698989	59.698847	0.000050

The frequency estimation can be considered very accurate for Method 3. But if the results in Table 4-III are compared with the results in Table 4-I, which describes the accuracy of the DFT method discussed in Section 4.1, the Linear Least Squares method is apparently inferior.

4.3 Nonlinear Least Squares technique

From section 4.2, the Linear Least Squares method is actually solving a Taylor Series approximation of the sinusoidal signal. Essentially, the Least Squares method, by definition, is a type of method that fits a set of observations with a model with unknown parameters. Given a set of voltage signal sampling data, if a model that fits closely to the data can be found, we can accurately estimate the characters of the original signal by the calculated parameters [77]-[86].

Virtually, three parameters can decide the nature of a sinusoidal signal, its magnitude, frequency and the initial phase angle. When the data window is fairly small, it is safe to assume that those three parameters remain constant. The voltage signal can be represented by (4-5).

$$V(t) = V_m \sin(2\pi ft + \theta) \qquad (4\text{-}5)$$

Consider a set of ***n*** data points (t_1, v_1), (t_2, v_2),… (t_n, v_n). Stated as a Least Squares problem, the goal is to find the values of the parameter vector (V_m, f, θ) that minimize the sum of squares in (4-6) minimum.

$$S = \sum_{i=1}^{n} r_i^2 \tag{4-6}$$

Where:

$$r_i = v_i - V(t_i) = v_i - V_m \sin(2\pi f t_i + \theta)$$

The minimum sum of squares occurs when its gradient is zero, as illustrated in (4-7).

$$\left.\begin{aligned} \frac{\partial S}{\partial V_m} &= 0 \\ \frac{\partial S}{\partial f} &= 0 \\ \frac{\partial S}{\partial \theta} &= 0 \end{aligned}\right\} \Rightarrow \left\{\begin{aligned} 2\sum_{i=1}^{n} r_i \frac{\partial r_i}{\partial V_m} &= 0 \\ 2\sum_{i=1}^{n} r_i \frac{\partial r_i}{\partial f} &= 0 \\ 2\sum_{i=1}^{n} r_i \frac{\partial r_i}{\partial \theta} &= 0 \end{aligned}\right\}$$

$$\Rightarrow \left\{\begin{aligned} 2\sum_{i=1}^{n} [V_m \sin(2\pi f t_i + \theta) - v_i][\sin(2\pi f t_i + \theta)] &= 0 \\ 2\sum_{i=1}^{n} [V_m \sin(2\pi f t_i + \theta) - v_i][2\pi t_i \cos(2\pi f t_i + \theta)] &= 0 \\ 2\sum_{i=1}^{n} [V_m \sin(2\pi f t_i + \theta) - v_i][\cos(2\pi f t_i + \theta)] &= 0 \end{aligned}\right\} \tag{4-7}$$

Each of the equations in (4-7) is a nonlinear function of all the parameters. Although there is no open solution for (4-7), they can have an optimized approximation using nonlinear iteration methods.

The parameter vector can be represented as β = (V_m, f, θ) for the sake of discussion. The first step to start a nonlinear iteration is to choose an initial point. Assuming that the initial value of β is β_0, $V(t, \beta)$ can be represented by its first Taylor Series expansion centered with β_0 , shown in (4-8). It is a formula that contains the partial derivatives of V with respect to each parameter.

$$V(t_i, \beta) \approx V(t_i, \beta_0) + [\frac{\partial V(t_i, \beta_0)}{\partial V_m}(V_m - V_{m0}) + \frac{\partial V(t_i, \beta_0)}{\partial f}(f - f_0) + \frac{\partial V(t_i, \beta_0)}{\partial \theta}(\theta - \theta_0)]$$

(4-8)

Substitute (4-8) into the representation of r_i can derive equation (4-9).

$$r_i = v_i - V(t_i, \beta)$$

$$\approx [v_i - V(t_i, \beta_0)] - [\frac{\partial V(t_i, \beta_0)}{\partial V_m}(V_m - V_{m0}) + \frac{\partial V(t_i, \beta_0)}{\partial f}(f - f_0) + \frac{\partial V(t_i, \beta_0)}{\partial \theta}(\theta - \theta_0)]$$

$$= \Delta V_i + \boldsymbol{J}_i \Delta \boldsymbol{\beta} \quad (4\text{-}9)$$

Where:

$$\Delta V_i = v_i - V(t_i, \beta_0),\ -\boldsymbol{J}_i = [\frac{\partial r(t_i, \beta_0)}{\partial V_m}, \frac{\partial r(t_i, \beta_0)}{\partial f}, \frac{\partial r(t_i, \beta_0)}{\partial \theta}],\ \Delta\boldsymbol{\beta} = \begin{bmatrix} V_m - V_{m0} \\ f - f_0 \\ \theta - \theta_0 \end{bmatrix}$$

If all *n* observation points are taken into consideration, equation (4-9) can be expand into matrix formation as in (4-10).

$$\boldsymbol{J}^T \boldsymbol{J} \Delta \boldsymbol{\beta} = \boldsymbol{J}^T \Delta \boldsymbol{V} \quad (4\text{-}10)$$

Where:

$$\boldsymbol{J} = \begin{bmatrix} -\frac{\partial r(t_1, \beta_0)}{\partial V_m}, -\frac{\partial r(t_1, \beta_0)}{\partial f}, -\frac{\partial r(t_1, \beta_0)}{\partial \theta} \\ \cdots\cdots\cdots\cdots\cdots \\ -\frac{\partial r(t_n, \beta_0)}{\partial V_m}, -\frac{\partial r(t_n, \beta_0)}{\partial f}, -\frac{\partial r(t_n, \beta_0)}{\partial \theta} \end{bmatrix},\ \Delta \boldsymbol{V} = \begin{bmatrix} v_1 - V(t_1, \beta_0) \\ \cdots\cdots \\ v_n - V(t_n, \beta_0) \end{bmatrix}$$

$\boldsymbol{\Delta\beta}$ can be solved by (4-10), and then β can be updated with equation $\boldsymbol{\beta_1} = \boldsymbol{\beta_0} + \boldsymbol{\Delta\beta}$. Next iteration will use the first order of Taylor Series expansion around $\boldsymbol{\beta_1}$ to represent *V* and repeat steps from (4-8) to (4-10) to solve $\boldsymbol{\Delta\beta}$. The process stops at the *k*th iteration, when $S(\beta_k)$ is smaller enough to be considered zero. This is the commonly used Newton-Gauss procedure to solve the Nonlinear Least Squares optimization problem.

4.4 Algorithm performance comparison

This algorithm is implemented by using the "nonlinearLeastSquares" options in the Matlab curve fitting tool box. The initial value of the parameters are chosen as V_m = 10V, f=60 Hz and θ=0 degrees.

In order to evaluate the proposed algorithm, the performance comparison is made with the DFT-based algorithm that is introduced in Section 4.2.

First, it is necessary to evaluate the Nonlinear Least Squares method with constant frequency input. The DFT-based method, as discussed above, has very accurate frequency estimations for different frequency input signals. The comparison of the Nonlinear LSQ method with the DFT method can be seen in

Table 4-IV, from where it can be concluded that both methods have very high accuracy when measuring pure sinusoidal signal that do not have noise pollution. The Nonlinear LSQ method even shows slightly better performance when the input signal is not 60Hz.

Table 4-IV Constant frequency input comparison of Nonlinear LSQ method with DFT method (Unit : Hz)

Input Signal		Average	Median	Max	Min	STD
59.7	Nonlinear LSQ	59.700000	59.700000	59.700000	59.700000	0.000000
	DFT	59.700000	59.700000	59.700001	59.699999	0.000001
60.0	Nonlinear LSQ	60.000000	60.000000	60.000000	60.000000	0.000000
	DFT	60.000000	60.000000	60.000000	60.000000	0.000000
60.3	Nonlinear LSQ	60.300000	60.300000	60.300000	60.300000	0.000000
	DFT	60.299999	60.299999	60.300001	60.299997	0.000001

Equally in the pure signal frequency measurement accuracy, the Nonlinear LSQ algorithm and the DFT algorithm is then been compared with a noise polluted input signal. It is thus a critically criteria to evaluate their superiority of one over another. Figure 4.8 displays the algorithms' performance at different noise levels.

As summarized in Table 4-V, at each noise level, the Nonlinear LSQ algorithm demonstrates better accuracy of one order of magnitude higher than the DFT algorithm results.

Figure 4.9 is the power spectrum density of the 59.7Hz signal with different level of signal-to-noise ratios.

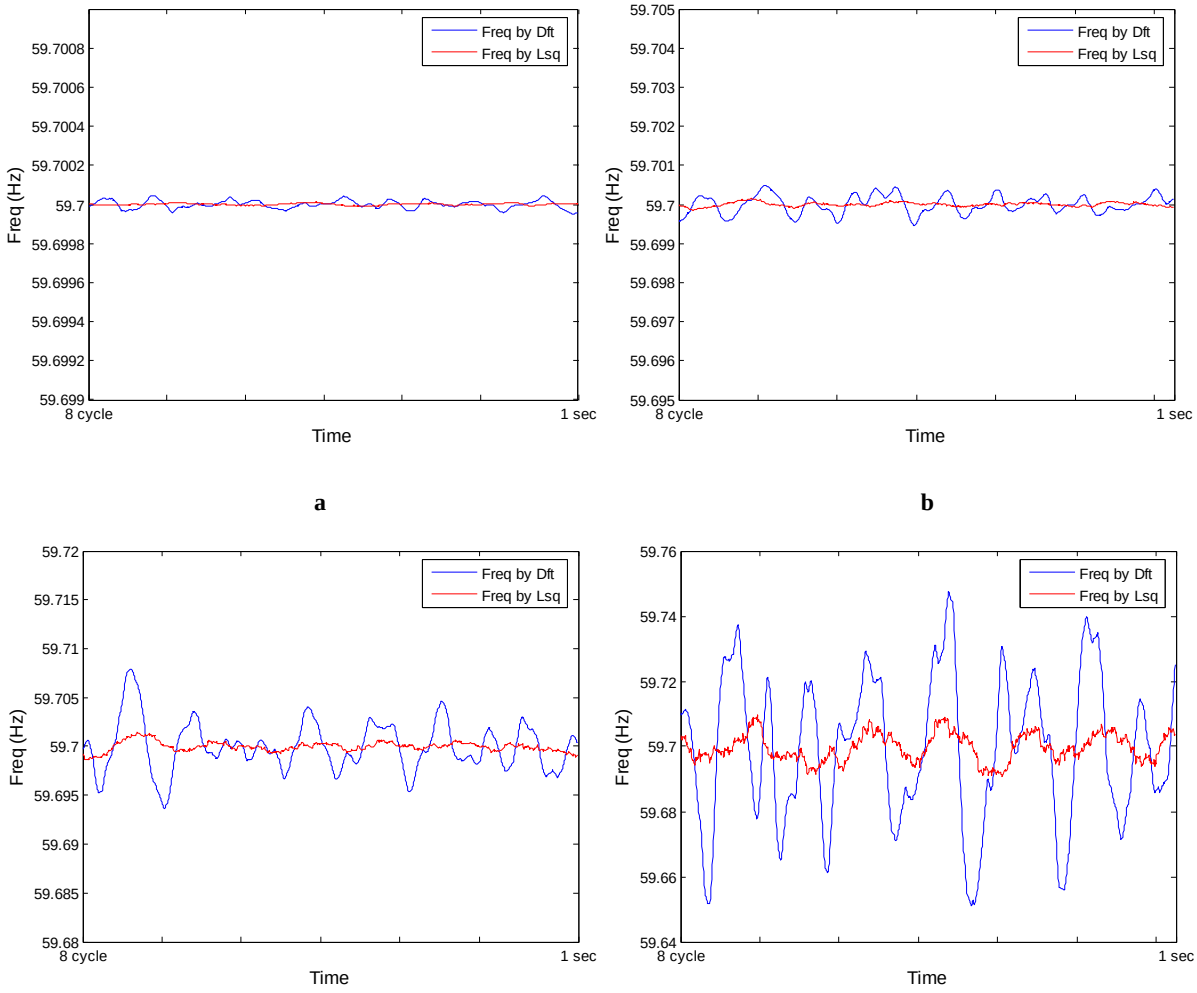

Figure 4.8 Comparison of Nonlinear LSQ with DFT method's frequency estimation results when the signal is polluted by Gaussian white noise with different signal-to-noise ratio: 80db (a), 60db (b), 40db (c), and 20db (d)

Table 4-V Comparison of Nonlinear LSQ method with DFT method (Input signal is 59.7Hz sinusoidal plus White Gaussian noise) (Unit if not specified is Hz)

SNR		Average	Median	Max	Min	STD
80 dB	Nonlinear LSQ	59.700000	59.700001	59.700013	59.699989	0.000005
	DFT	59.700000	59.700000	59.700046	59.699951	0.000021
60 dB	Nonlinear LSQ	59.700000	59.699998	59.700165	59.699852	0.000052
	DFT	59.699999	59.700000	59.700492	59.699454	0.000234
40 dB	Nonlinear LSQ	59.699977	59.699995	59.701453	59.698629	0.000493
	DFT	59.699982	59.699763	59.707927	59.693645	0.002576
20 dB	Nonlinear LSQ	59.699676	59.699393	59.709700	59.690813	0.004223
	DFT	59.699196	59.701246	59.747396	59.651000	0.022696

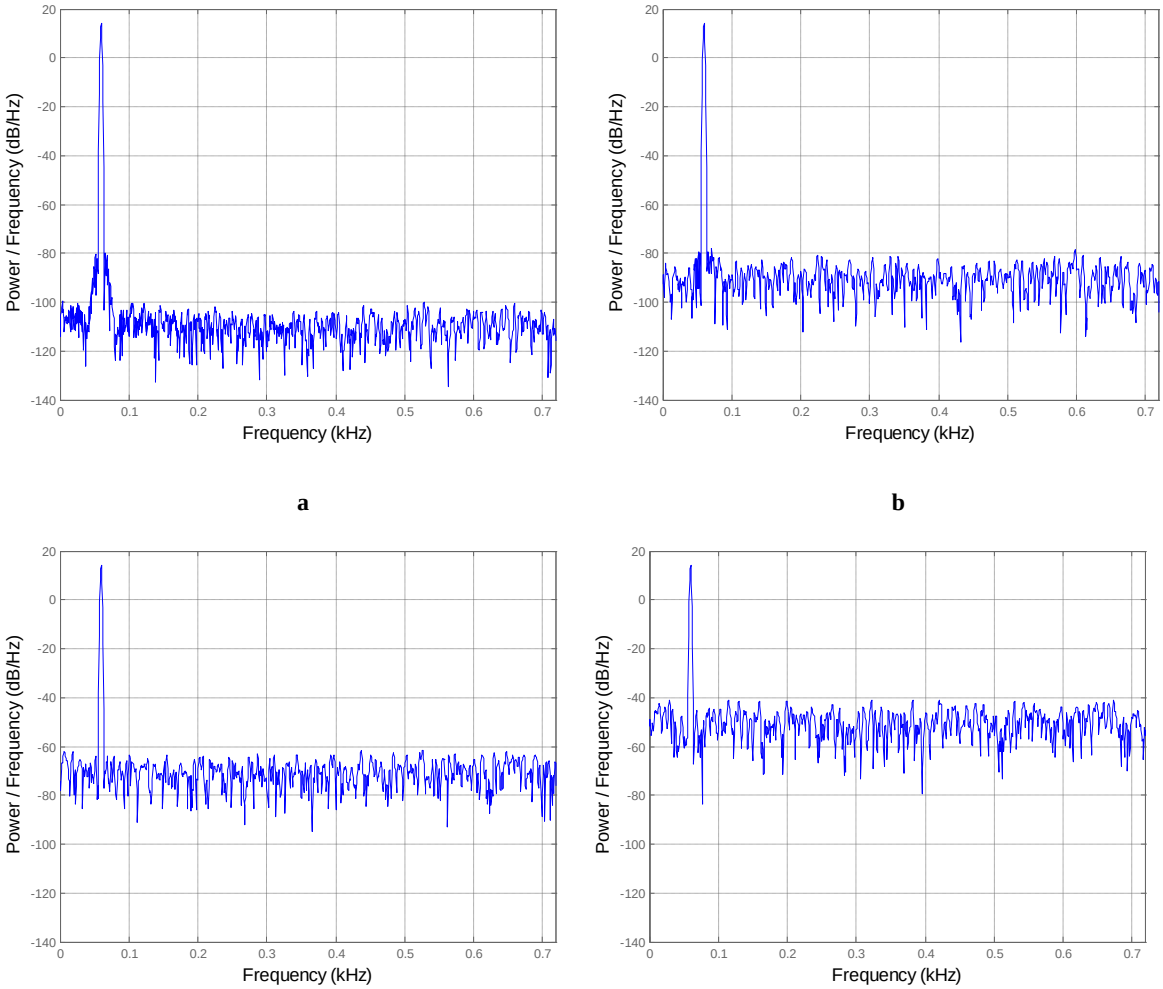

Figure 4.9 Power Spectrum Density of 59.7Hz sinusoidal signal polluted by Gaussian white noise with different signal-to-noise ratio: 80dB (a), 60dB (b), 40dB (c), and 20dB (d)

The base frequency of the signal in the previous test is 59.7Hz, which may not be commonly seen in real power systems such as the EI and WECC. To better approximate reality, the input signal frequency is changed into 59.95 Hz and the results can be seen in Figure 4.10 and Table 4-VI. The influence of noise on the final measurement accuracy is almost the same as when the signal frequency is further away from nominal frequency.

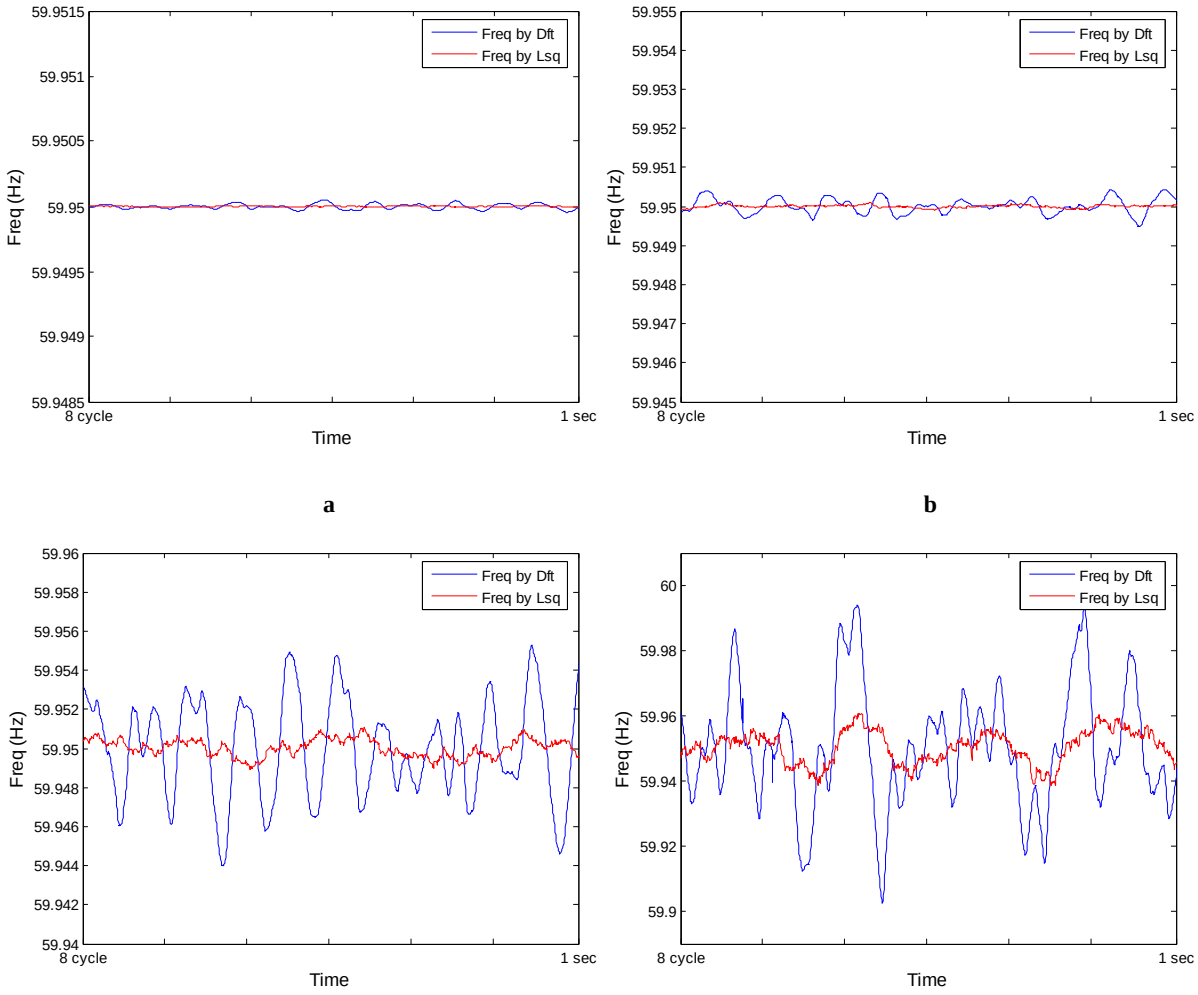

Figure 4.10 Comparison of Nonlinear LSQ with DFT method's frequency estimation results when the signal is polluted by Gaussian white noise with different signal-to-noise ratio: 80dB (a), 60dB (b), 40dB (c), and 20dB (d)

Table 4-VI Comparison of Nonlinear LSQ method with DFT method (Input signal is 59.95Hz sinusoidal plus White Gaussian noise) (Unit if not specified is Hz)

SNR		Average	Median	Max	Min	STD
80 dB	Nonlinear LSQ	59.950000	59.950000	59.950009	59.949992	0.000004
	DFT	59.949999	59.949999	59.950050	59.949955	0.000020
60 dB	Nonlinear LSQ	59.950001	59.950005	59.950095	59.949909	0.000035
	DFT	59.950011	59.950008	59.950430	59.949486	0.000200
40 dB	Nonlinear LSQ	59.950013	59.950022	59.951062	59.948927	0.000445
	DFT	59.950059	59.950141	59.955321	59.944015	0.002583
20 dB	Nonlinear LSQ	59.950170	59.951013	59.960792	59.938593	0.005092
	DFT	59.949732	59.948579	59.994005	59.902424	0.018351

Even with the significant advantage of noise tolerance, the Nonlinear LSQ algorithm is not necessarily a good fit for real-time frequency tracking because that requires a quick response on the frequency dynamic changes, such as such a drop of frequency. The same step change test (change frequency from 59.7 Hz to 59.5 Hz) that used in Section 4.3 for the DFT method is applied to the Nonlinear LSQ method too. The responses of both of the algorithms are compared together in Figure 4.11; the left side of the figure contains plots for the entire signal frame, the right side of the figure shows plots zoomed in close to the frequency change. It has been understood from the step test, that the two algorithms require the same amount of time, which is the duration of one data window, to respond to the sudden frequency drop. It is not affected by the noise to signal ratio, or the amount of frequency changes in the input signal, like described in Figure 4.12 where signal frequency increases from 60.3 Hz to 60.5 Hz.

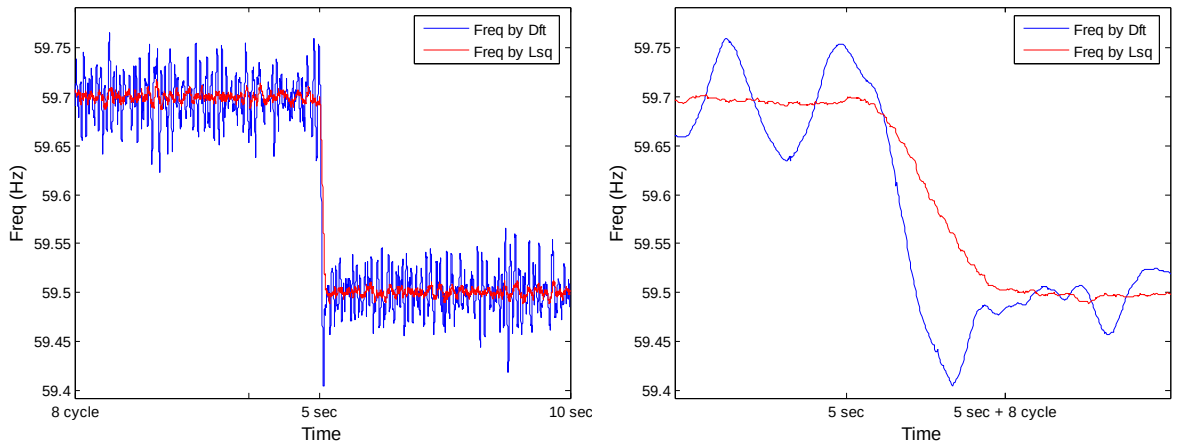

a

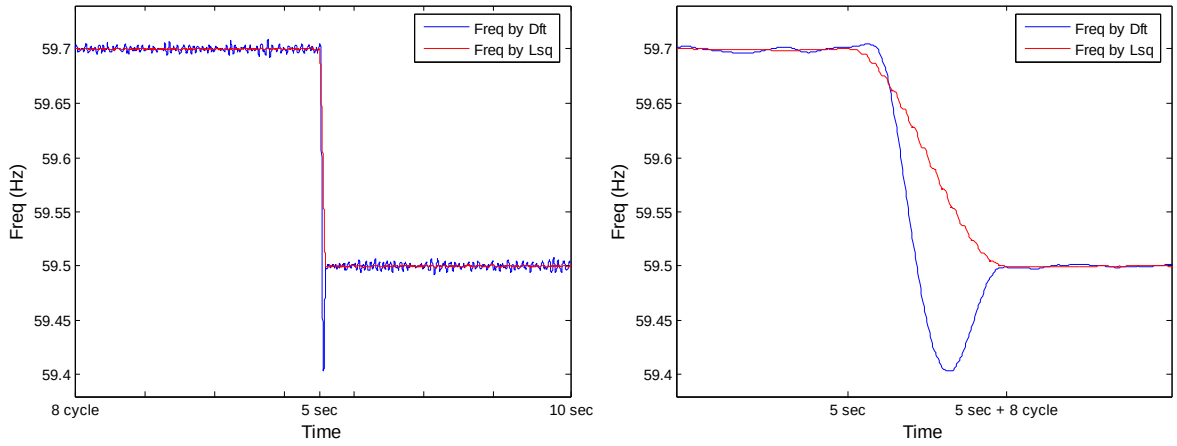

b

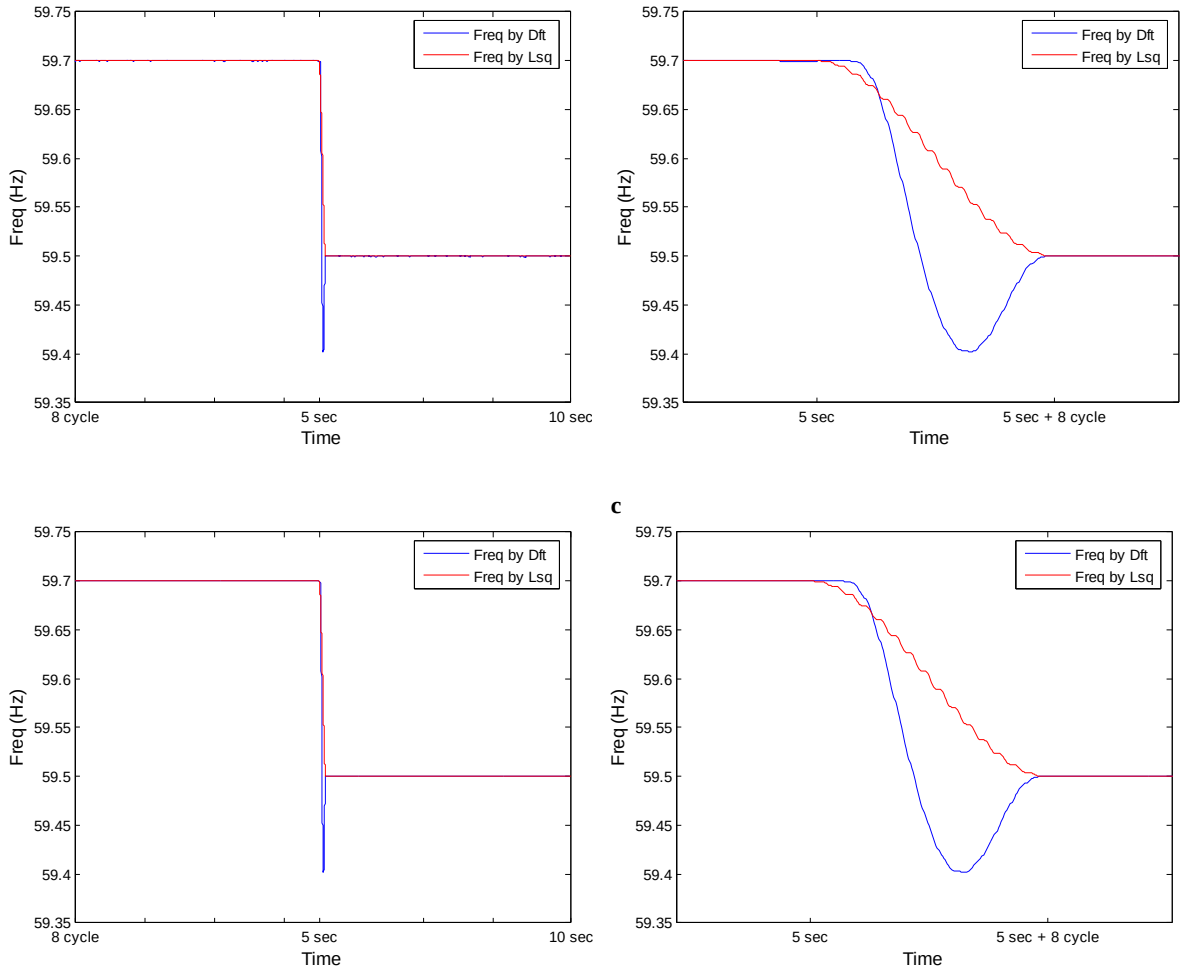

Figure 4.11 Comparison of Nonlinear LSQ with DFT method's step change frequency estimation results when the signal is polluted by Gaussian white noise with different signal-to-noise ratio: 80dB (a), 60dB (b), 40dB (c), and 20dB (d)

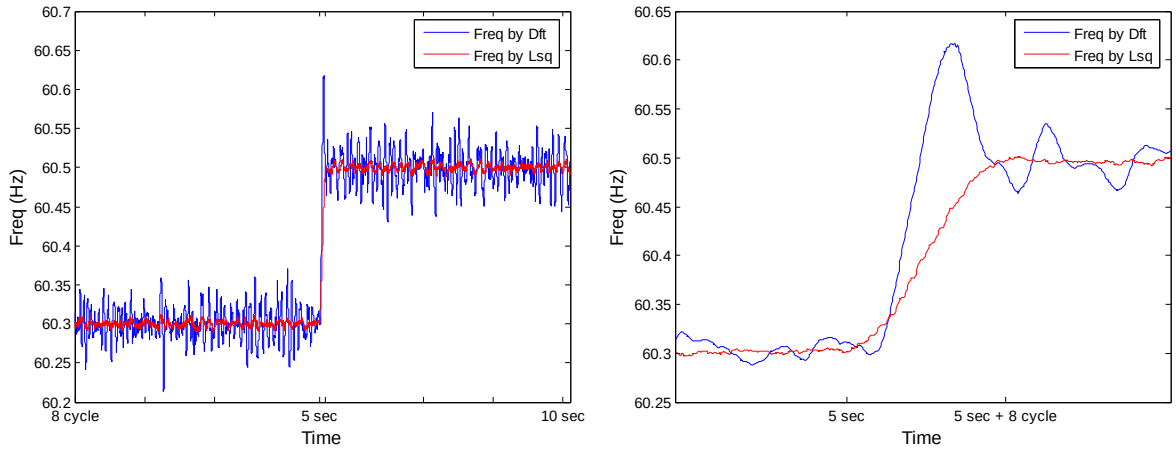

Figure 4.12 Comparison of Nonlinear LSQ with DFT method's step change frequency estimation results when the signal is polluted by Gaussian white noise with signal-to-noise ratio 20dB

Both the voltage and current signals in power systems contain a variety of noises, including impulse noise, harmonics, and white noises. Figure 4.13 shows the power spectrum density analysis result of 10 seconds' worth of data that is acquired from a wall outlet by NI-9125 data acquisition (DAQ) card. A GE Volt-PAC Variac is used for stepping down transform the 120 V signals to 10 V. The power spectrum density basically represents the strength of each frequency components within the signal. The signal collected from the wall outlet contains strong harmonic components and white noise throughout the entire frequency range.

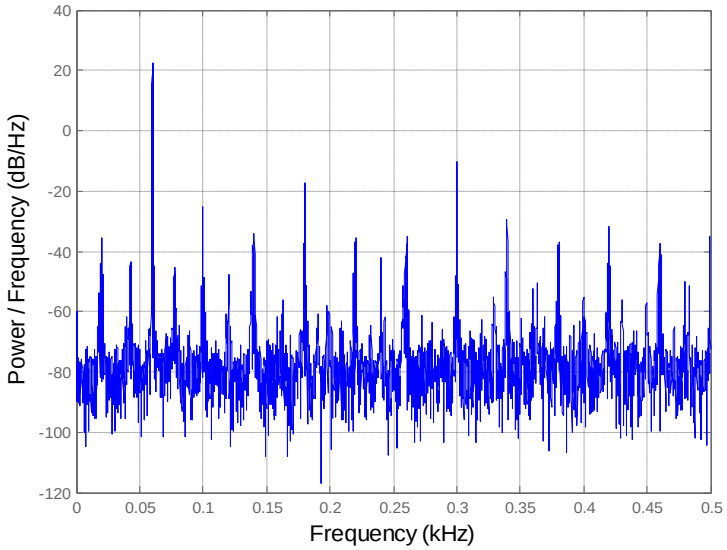

Figure 4.13 Power spectrum density of the real system signal

Usually, measurement devices such as PMUs, FDRs and digital meters will have integrated filtering components integrated in order to minimize the noise influence on the measurement results. Thus, a Chebyshev band pass filter with passing band from 40 Hz-80 Hz is applied to the 10 seconds worth of data being tested with the algorithms. The PSD of the filtered signal is shown in Figure 4.14.

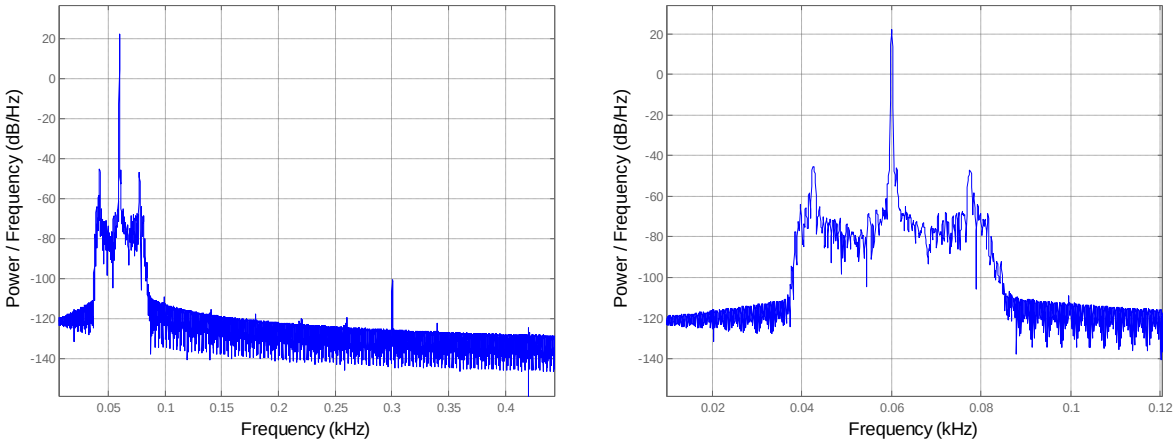

Figure 4.14 Power spectrum density of the filtered signal: full length(left), zoom in (right)

The band pass filter effectively reduced the components beyond the passing band, and the signal strength at the desired frequency is much higher than those others that are still in the passing band. This data is feed into both algorithms and the results are plotted in Figure 4.15. The LSQ algorithm illustrates a more clear measurements pattern and narrower band which can be seen in their histograms in Figure 4.16.

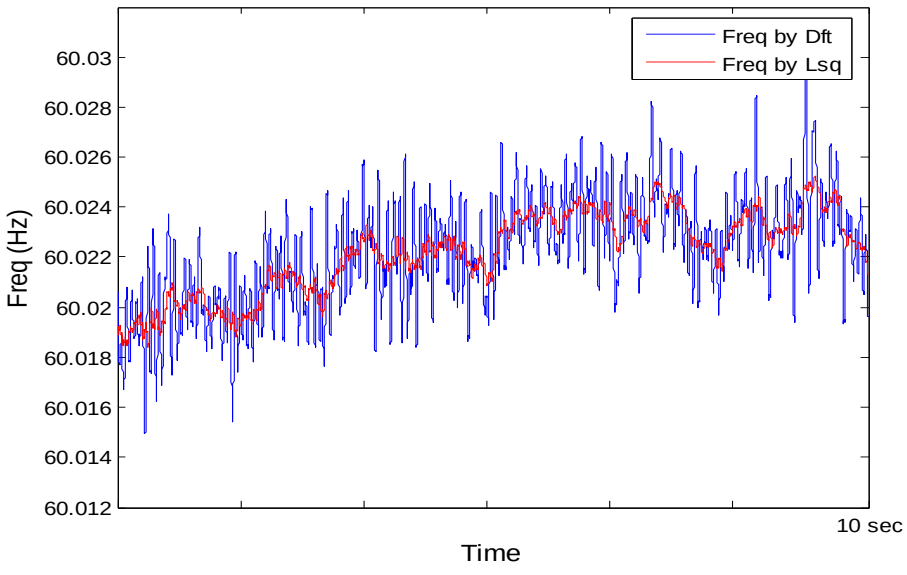

Figure 4.15 Comparison of frequency measurements of real system signal between DFT and Nonlinear LSQ methods

Typically, the calculation result of DFT based method is further processed by moving median filter for noise reducing purpose. In appendix I, two plots based on Figure 4.15 and demonstrate the NLSQ method's superiority even compared 5 point moving median filter result.

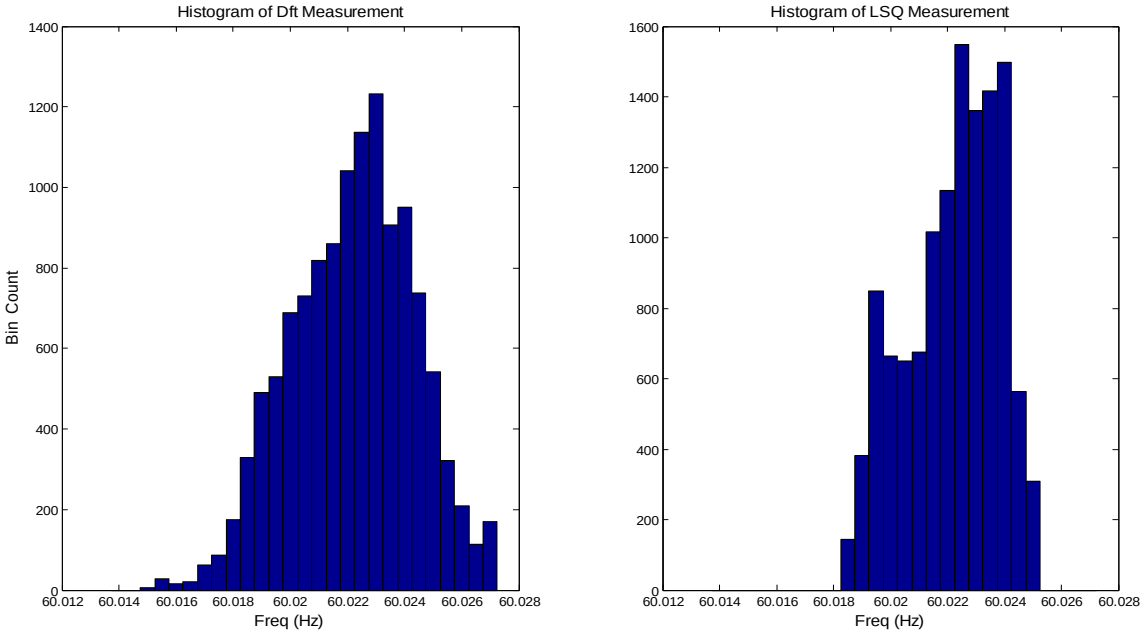

Figure 4.16 Histograms of DFT and Nonlinear LSQ methods' measurements on real system signal

Assuming practically that the original signal can be filtered further, similar to adding a band pass filter with passing band of 50 Hz-70 Hz, as shown in Figure 4.17, the measurement resolution of both algorithms can be increased as shown in Figure 4.18.

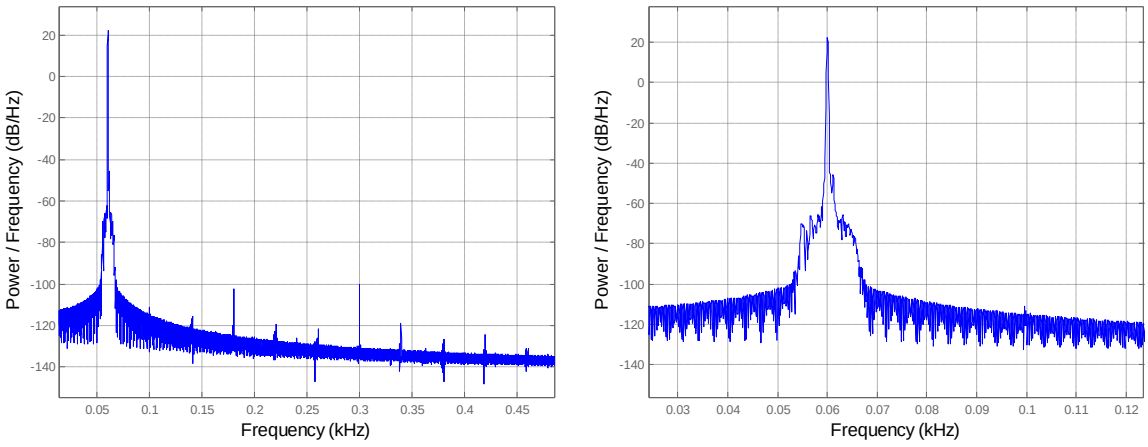

Figure 4.17 Power spectrum density of the filtered signal: full length (left), zoomed in (right)

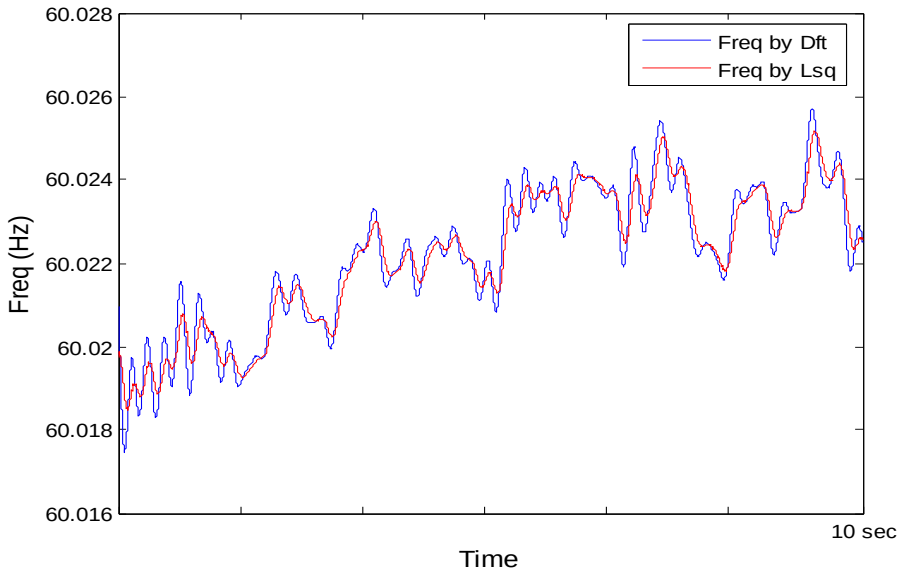

Figure 4.18 Comparison of frequency measurements of real system signal between DFT and Nonlinear LSQ methods

The histograms of the calculation results for both algorithms in Figure 4.19 still demonstrates a narrower deviation results from the LSQ method than from the DFT method.

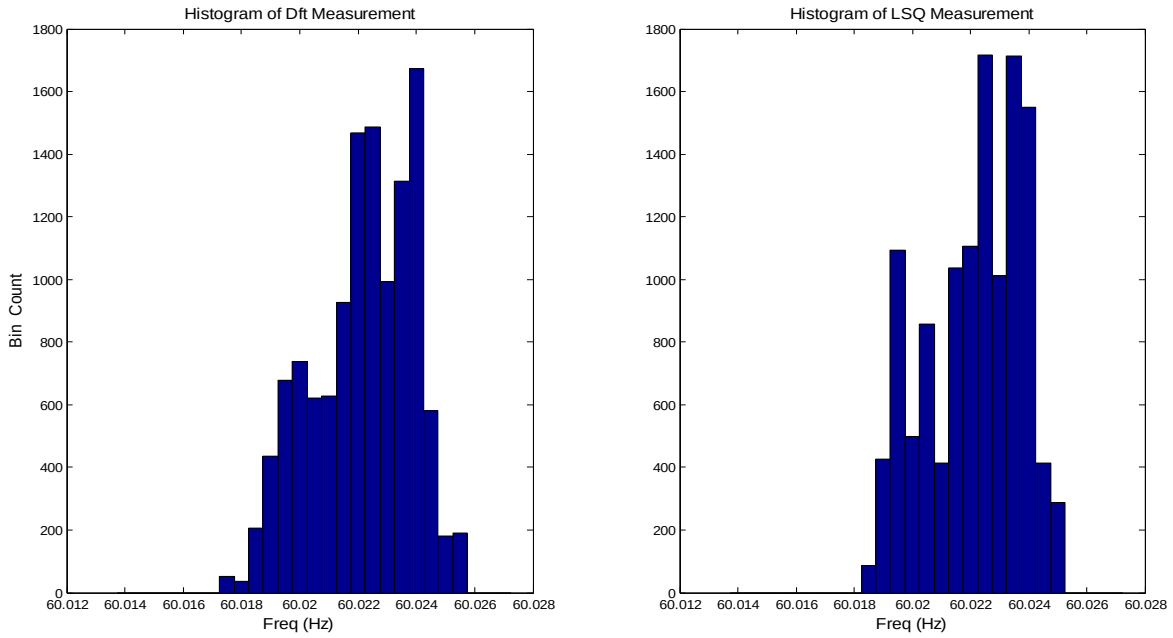

Figure 4.19 Histograms of DFT and Nonlinear LSQ methods' measurements on real system signal

4.5 Conclusion and future work

The nonlinear least squares approach has more accurate measurement result when there is random noise in the signal. It is as fast as the DFT method in terms of measuring the frequency change in the system. More dynamic tests, such as a ramp test, should be conducted to enhance the conclusion. Also, further investigations need to be performed on the calculation burden this will impose on the hardware system, including if this method can be implemented in real-time measurements. In terms of enhancing any algorithm's performance with a noise-polluted signal, if the signal can be finely filtered as shown in Figure 4.17, the results could be improved. Thus, digital filtering can be adopted if it requires less computational burden and can reach the same accuracy level as using the NLSQ algorithm. In addition, reduce data window size could increase the calculation speed however will reduce the calculation accuracy. Therefore, investigation on data window size optimization is needed. Similarly, change of sampling rate could also increase calculation accuracy. If by increase sampling rate, the DFT method could reach to the same accuracy level as the NLSQ method without adding as much calculation burden, the DFT method is still superior. Harmonics components in the signal could influence the accuracy of the NLSQ method. In the discussion in this chapter it is not considered because of the assumption that the entire raw signal sampled will go through a filtering process. It is very easy to eliminate the harmonics this way. But it is benefit to study on the harmonics influence on the algorithm in the future.

Chapter 5 Voltage angle based power system instability detection method

5.1 Introduction to power system angle instability issues

Power system stability covers the vast issues that occur when the system is experiencing a disturbance. If the disturbance is small and the system perturbation is oscillatory in nature, it is described as a small signal stability problem (dynamic stability). It is reflected as a fluctuation in the power flow over the transmission lines. If the disturbance is causing one or group of the generators to lose of synchronization, due to a lack of synchronizing forces, it is a transient stability issue. The angle instability mainly refers to the second phenomenon where there is one or a group of generators losing synchronism [87]-[90].

Wide-area monitoring systems based on real time PMU measurements can provide great visibility to the angle instability conditions. This chapter will focus on developing an early warning algorithm on the FNET platform.

5.2 The Center-of-Bus-Angles approach

The term Center-of-Inertia (COI) is introduced in [87] by Kundur for the convenience of transient instability study. It essentially describes the center of rotor angles which are weighted by their inertias, as equations (5.1) illustrates:

$$\delta_{COI} = \frac{1}{H_T}\sum_{i=1}^{n} H_i \delta_i \tag{5-1}$$

where H_T is the sum of the inertia constants of all n generators in the system, δ_{COI} is the Center-of-Inertia angle, and δ_i is the rotor angle of the ith generator.

Direct observation of the rotor angle is not yet available. However, the generator bus voltage angles can be used as a parameter that reflects the rotor angle motion. Replacing the rotor angles by the phasor angle of the generator bus voltage [88], and assuming that the inertia is equally distributed to each of the generators in a bulk system, the equation can be simplified into (5.2).

$$\delta_{CBA} = \frac{1}{H_T}\sum_{i=1}^{n} H\delta_{bi} = \frac{H}{nH}\sum_{i=1}^{n}\delta_{bi} = \frac{\delta_{bT}}{n} \tag{5-2}$$

Where δ_{AAC} is the Center-of-Bus-Angles (CBA) and δ_{bi} is the voltage angle at bus i.

Under steady state conditions, generators are all working in parallel with their speeds remaining synchronized, and their relative rotor angle differences remain constant. After a disturbance, most of the generators are able to retain synchronization. Those who cannot need to be identified immediately and isolated from the system, they will be disconnected from the system until control actions enable them to regain synchronous speed. By only looking at the increase or decrease of angles of single generators, it is impossible to conclude that the system is unstable status because the angle and speed of a single generator varies all the time, yet still remains synchronized with the system.

An algorithm that utilizes wide-area phasor measurements for angle instability detection is developed. Let's start with PSS/E simulations of a 16,013 bus system. This system model was developed by and entitled to Tennessee Valley Authority to simulate Eastern Interconnection power grid. This dynamic simulation starts at 0 second, solves at every 0.005 second steps. A three-phase bus fault is applied to bus 21310 at 1 second and cleared at 1.3 second. Figure 5.1 plots voltage phasor angles on the buses that have higher than 200kV rated voltage. Obviously, several machines suffer instability reflecting on bus voltage angles' bifurcating.

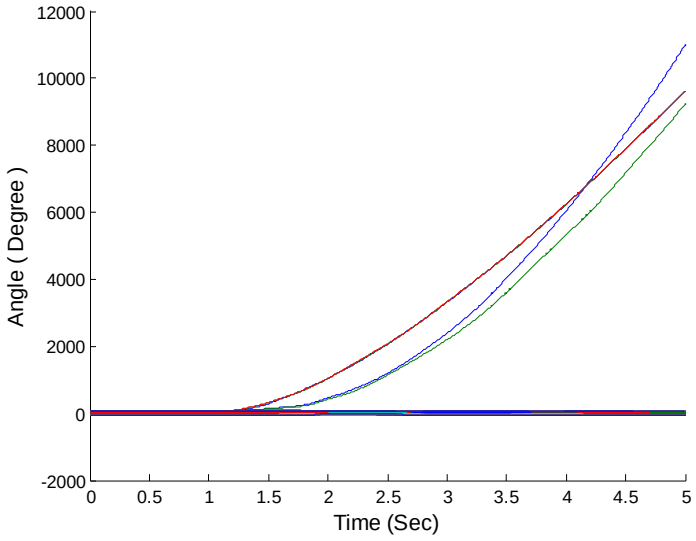

Figure 5.1 Voltage phasor angles in EI system PSS/E simulation (Bus fault on bus 21310 at 1 sec, cleared at 1.3 second)

In order to detect the instability within the system, a baseline is drawn to represent δ_{CBA} in Figure 5.2. Intuitively, buses that have angular instability compared with the rest of the system

should have an angle separation from the δ_{CBA}. Figure 5.3 plots the angle separation of each bus by subtracting their bus angles from the δ_{CBA}. From Figure 5.3, not only do the voltage angles at the unstable buses separate from the δ_{CBA}, the rest of the buses' voltage angles in the system also demonstrate an separation in the reversed the direction of the unstable group.

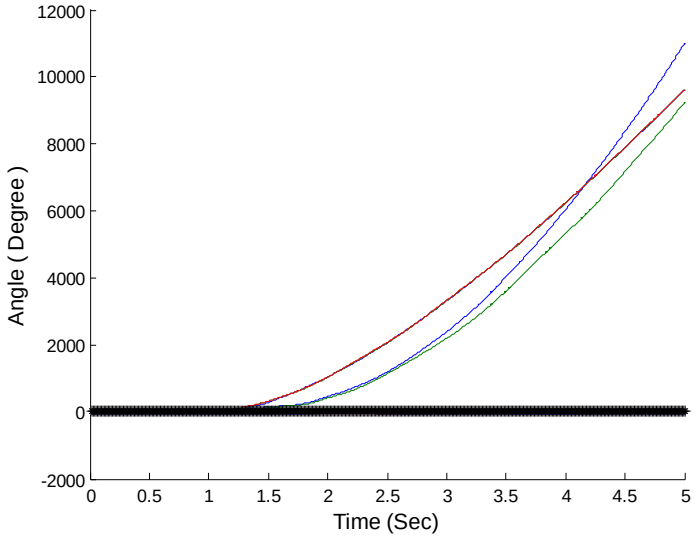

Figure 5.2 Bus angles and Center-of-Bus-Angles (dark black line)

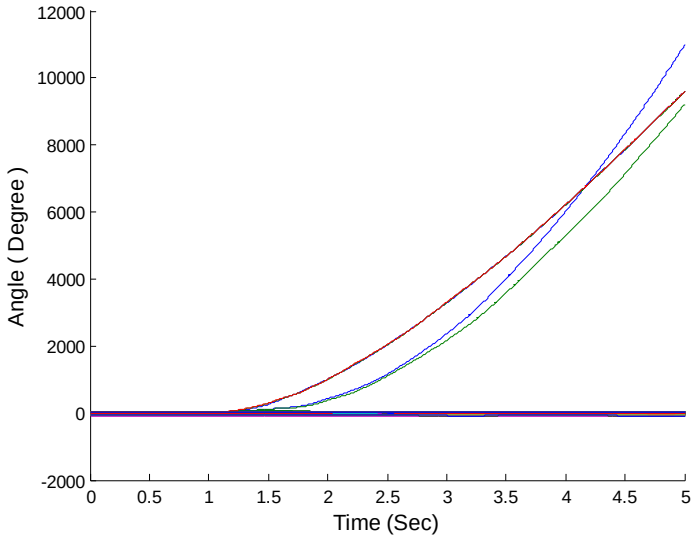

Figure 5.3 Bus angle separations from the CBA

There could be cases that the system is separated into two groups which are almost equally weighted in terms of bus numbers. The angle difference from the CBA at each bus may not be as

dramatic as those few unstable buses as shown in Figure 5.3. Therefore, scanning a single bus could be less informative than scanning the total differences from all the buses. By summing all the absolute angle separations at each time step, a line shown in Figure 5.4 can be drawn and is named Total-Angle-Separation (δ_{TAS}).

$$\delta_{TAS} = \sum_{i=1}^{n} \left| (\delta_i - \delta_{CBA}) \right| \qquad (5\text{-}3)$$

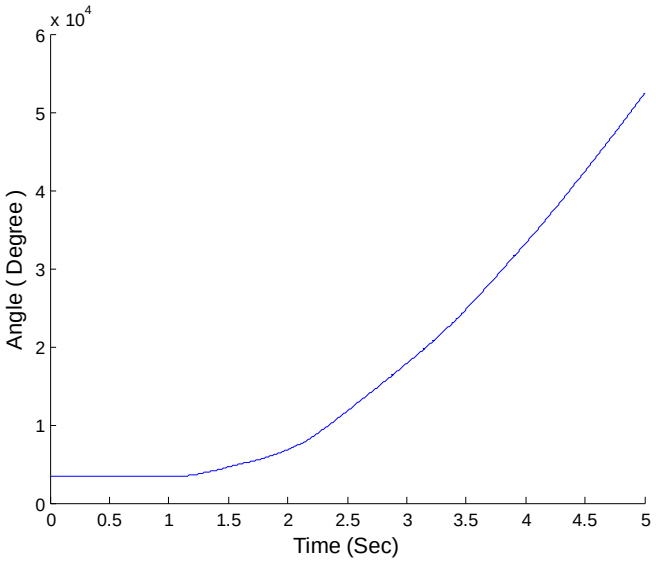

Figure 5.4 The Total-Angle-Separation

The TAS should be expected flat all the time under system steady state condition, but increase when angle instability occurs. The bus angles could experience a sudden redistribution and reach to equilibrium very quickly, but the TAS could remain lager than before. Merely judging angle instability by the increase of TAS is not sufficient. However, the detection algorithm can be implemented by calculating the derivative of 0.5 seconds worth of TAS data and moving the data window by 0.1 seconds each time, as illustrated in (5-4) and Figure 5.5. The data window length and moving pace can be modified according to different data conditions. The selection here reflects an empirical treatment of the FNET data flow. The basic rule is to minimize the window length but reserve enough tolerance on data variations.

$$\textit{Derivative of } \delta_{TAS} = \frac{d\delta_{TAS}}{dt} \quad \text{Where: } dt = 0.5\text{sec.} \qquad (5\text{-}4)$$

Time index	0.1	0.2	0.3	0.4	0.5	0.6	0.7

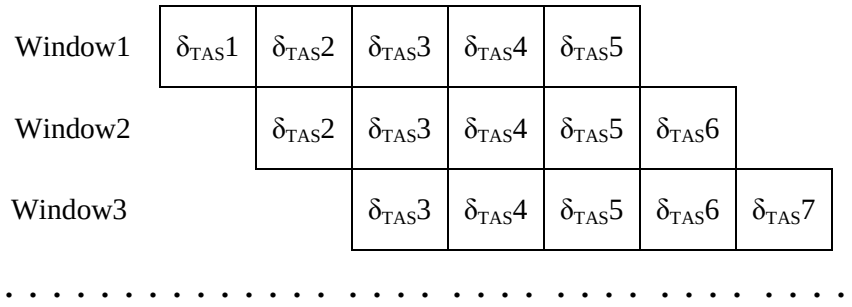

Figure 5.5 Moving window for TAS derivative calculation

The actuator of (5-4) is the Least Square line fit method. It fit a linear equation $y = ax+b$ to the data set and solves for parameters *a* and *b*, where *a* is the derivative value that is needed. Because there are extensive discussions in the previous chapters on the Least Squares line fit method, it will not be elaborated upon here.

When the derivative exceeds a predefined threshold, it indicates that the angle separation is increasing at a certain rate. If the rate is small (Threshold 1), the separate generators are likely to have enough inertia to retain stability. But when the angle separation happens with a high speed (Threshold 2), system operators should be alerted of an angle instability condition. Figure 5.6 displays the derivative of TAS and according to Table 5-I, where TH1 = 10 degree/sec and TH2 = 100 degree/sec, angle instability in this simulation case is detected 0.2 second after the disturbance occurs. The angle instability alert should remain until the derivative of separation falls below the first threshold, which indicates that the system has reached a new equilibrium. The derivative of TAS could go negative after a short period of the alerting status has been initiated. It is a sign of inter-area oscillation within the system, which means that the system has already passed the potential of first swing instability. However, the angle instability detection strategy still can be activates if there is not enough damping for the oscillation.

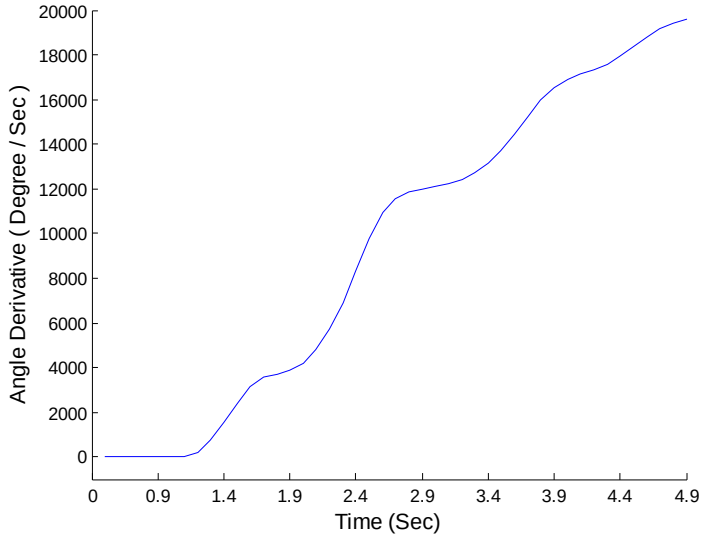

Figure 5.6 The derivative Total-Angle-Separation

Table 5-I Typical magnetic field strength for different voltage level lines

Time (Sec)	Angle Derivative (Degree / Sec)	Decision
0.6	0.000310065	Normal
0.7	0.000292176	Normal
0.8	0.000531162	Normal
0.9	0.000839139	Normal
1	0.001039792	Normal
1.1	48.06503511	Warning: exceeds TH1
1.2	463.3106043	Alert: exceeds TH2
1.3	1450.530641	Alert remain
1.4	2851.241269	Alert remain
1.5	4335.871222	Alert remain

A flow chart that summarizes the Angle Instability Detection scheme is presented in Figure 5.7.

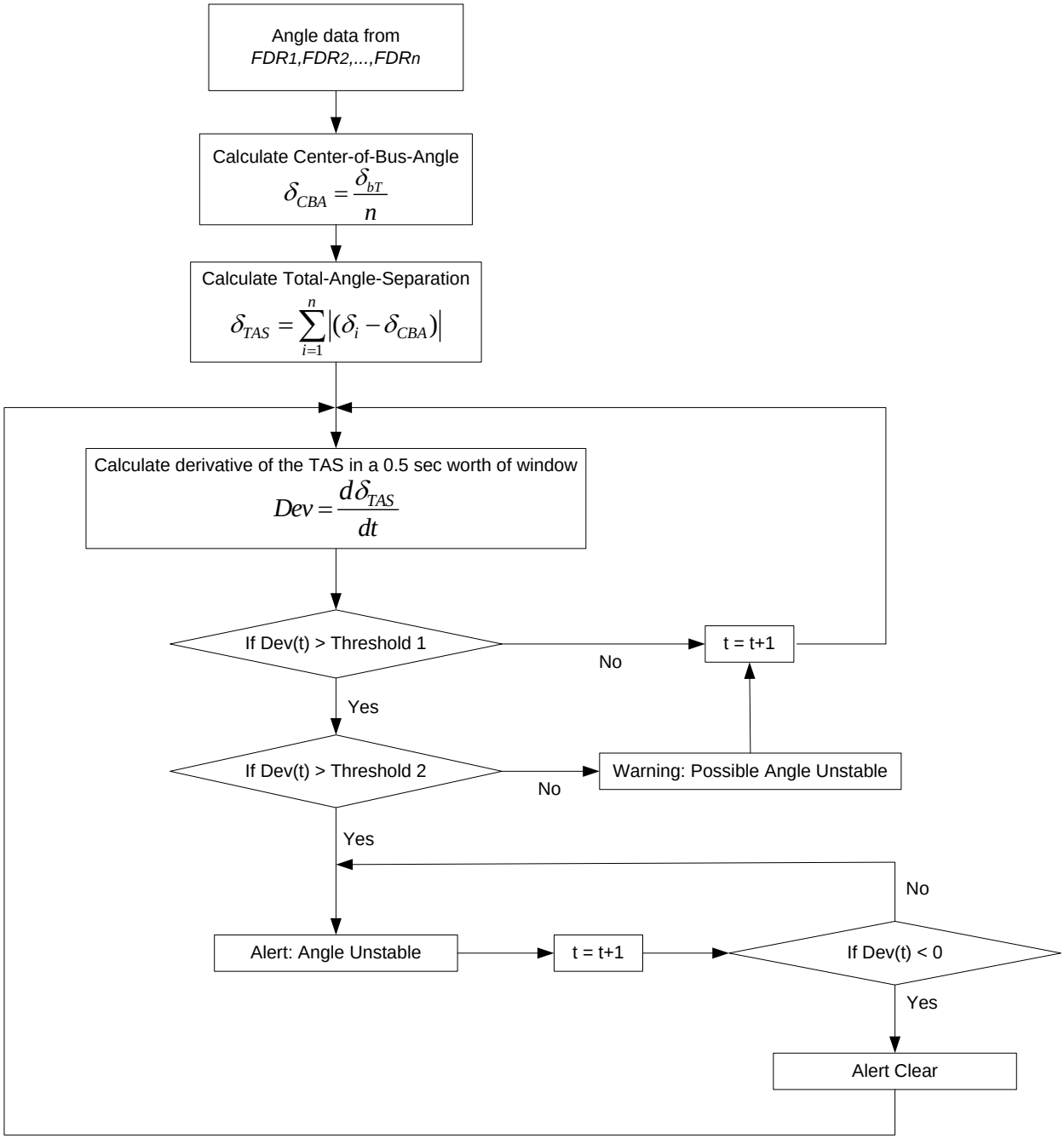

Figure 5.7 Angle Instability Detection scheme

5.3 Test simulation cases on PSS/E EI system model

More simulation cases with PSS/E EI system are presented in the following paragraphs. Each of the figure mark represents:

(a) Voltage angles in each generation bus that higher than 200kV

(b) Bus angles and Center-of-Bus-Angles (dark black line)

(c) Bus angle separations from the CBA

(d) The Total-Angle-Separation

(e) The derivative of the Total-Angle-Separation

The simulation scenarios of each case are summarized in Table 5-II Summary of simulation scenarios of each case, the sample case presented in the previous paragraphs is shown as case 1 in the table.

Table 5-II Summary of simulation scenarios of each case

Case Num.	Event scenarios	Real power involved (MW)	Voltage Level (kV)
Case 1	Bus 21310 fault occurred at 1sec cleared at 1.3sec	4207.229	345
Case 2	Bus 21650 fault occurred at 1sec cleared at 1.3sec	2550.880	345
Case 3	Bus 22607 fault occurred at 1sec cleared at 1.3sec	2600.000	765
Case 4	Bus 26648 fault occurred at 1sec cleared at 1.3sec	2334.346	345
Case 5	Bus 32274 fault occurred at 1sec cleared at 1.3sec	1839.000	345
Case 6	Bus 37606 fault occurred at 1sec cleared at 1.3sec	2183.000	345
Case 7	Bus 22607 fault occurred at 1sec cleared at 1.1sec	2600.000	765
Case 8	Generation Trip at Bus 26648 at 1 sec	2334.346	345
Case 9	Disconnected load Bus 80676 (Load Shedding) at 1 sec	2017.549	220
Case 10	Generation Trip at Bus 27008 at 1 sec	1470.000	345

Case 2:

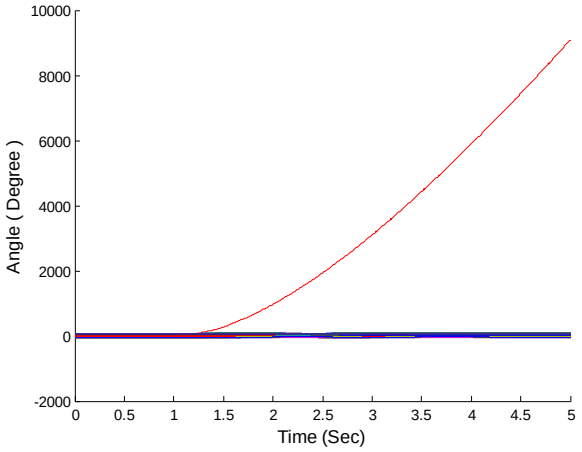
Angle (Degree)
Time (Sec)

(a)

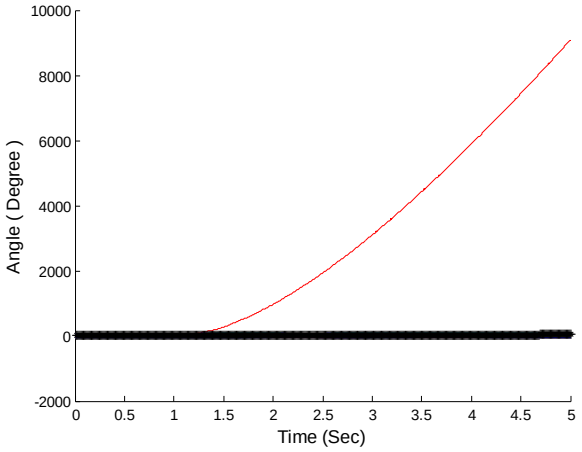
Angle (Degree)
Time (Sec)

(b)

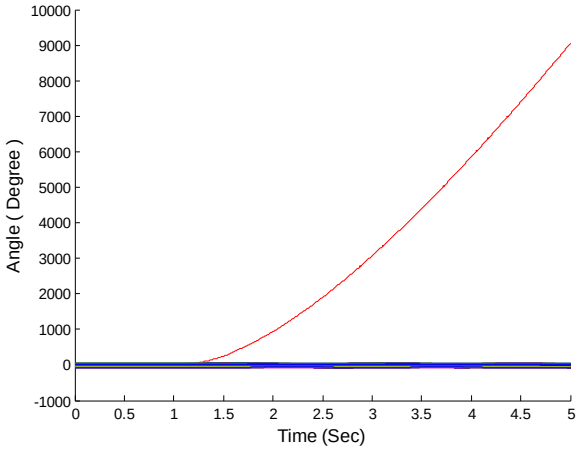
Angle (Degree)
Time (Sec)

(c)

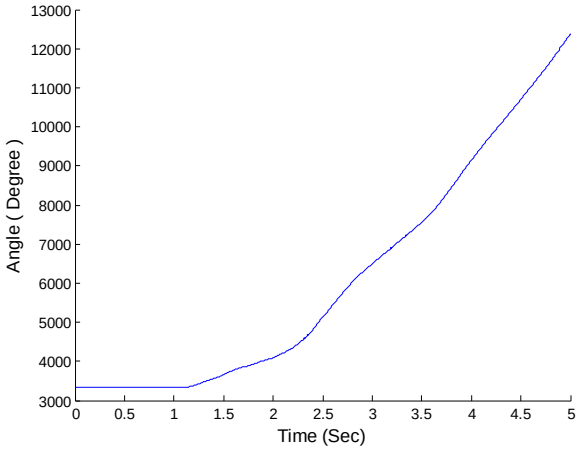
Angle (Degree)
Time (Sec)

(d)

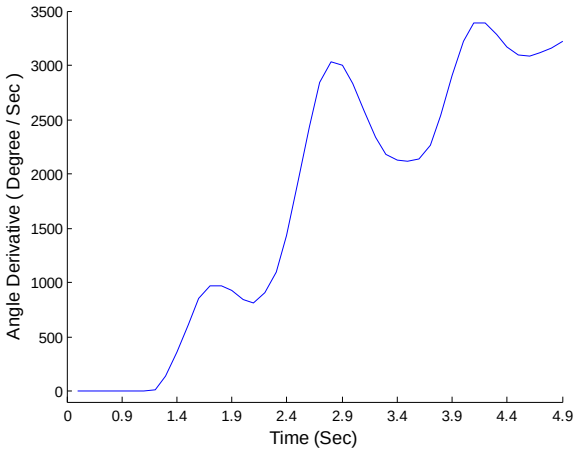
Angle Derivative (Degree / Sec)
Time (Sec)

(e)

Case 3:

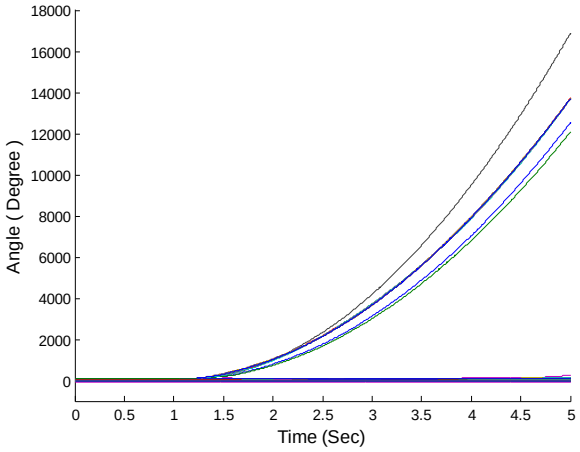
Angle (Degree)
Time (Sec)

(a)

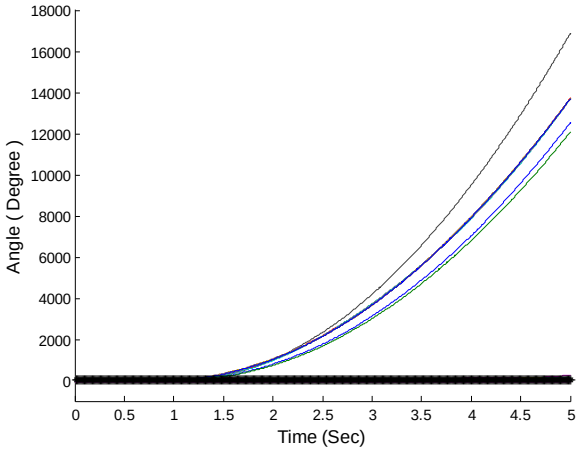
Angle (Degree)
Time (Sec)

(b)

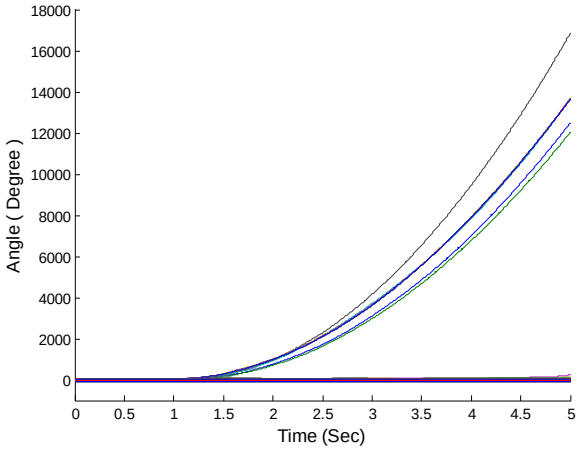
Angle (Degree)
Time (Sec)

(c)

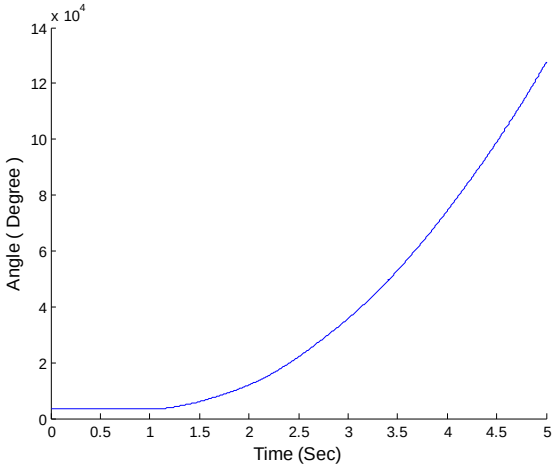
x 10^4
Angle (Degree)
Time (Sec)

(d)

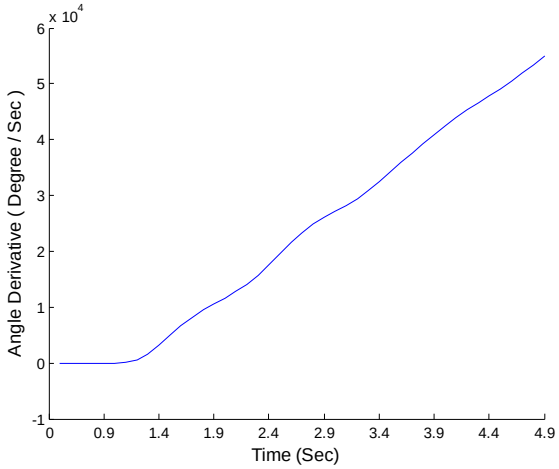
x 10^4
Angle Derivative (Degree / Sec)
Time (Sec)

(e)

Case 4:

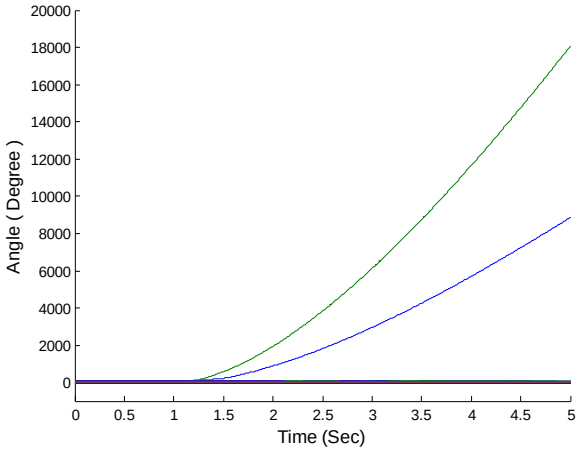
Angle (Degree)
Time (Sec)

(a)

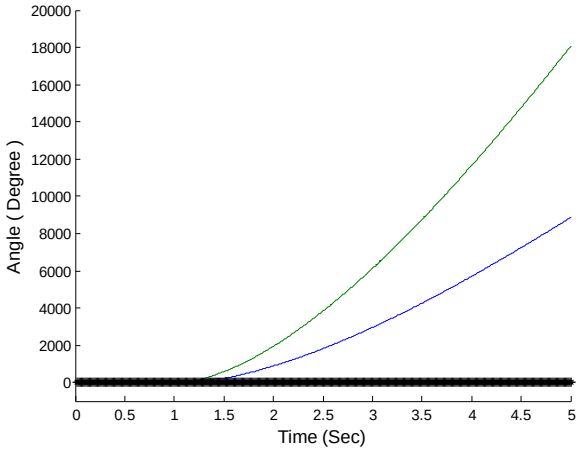
Angle (Degree)
Time (Sec)

(b)

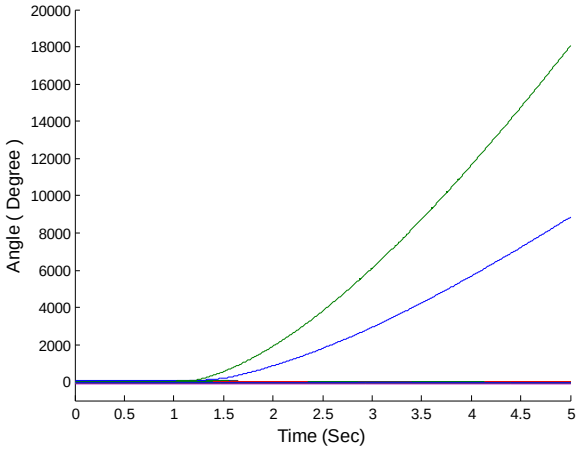
Angle (Degree)
Time (Sec)

(c)

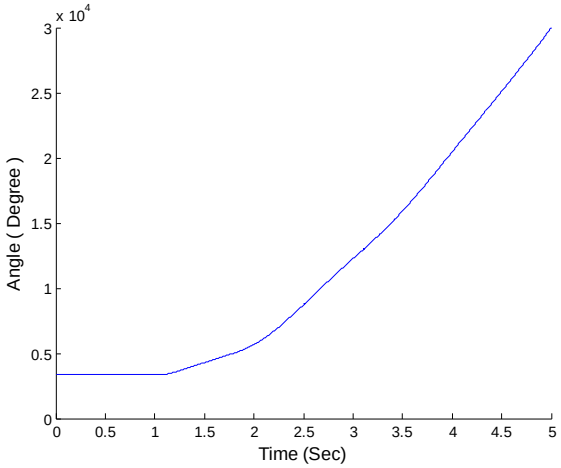
x 10^4
Angle (Degree)
Time (Sec)

(d)

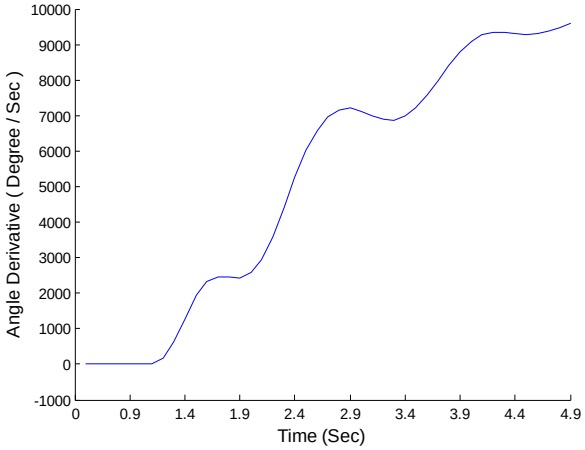
Angle Derivative (Degree / Sec)
Time (Sec)

(e)

Case 5:

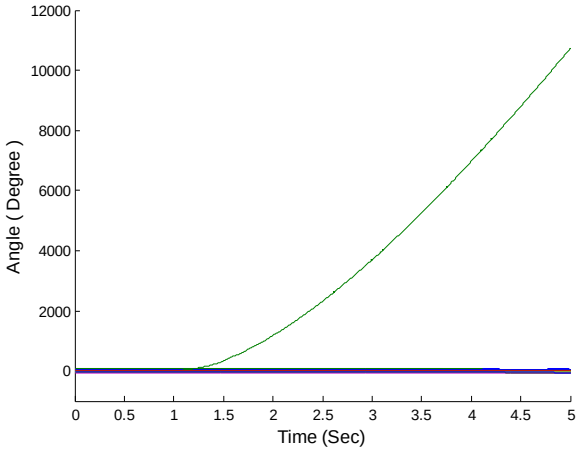
Angle (Degree)
Time (Sec)

(a)

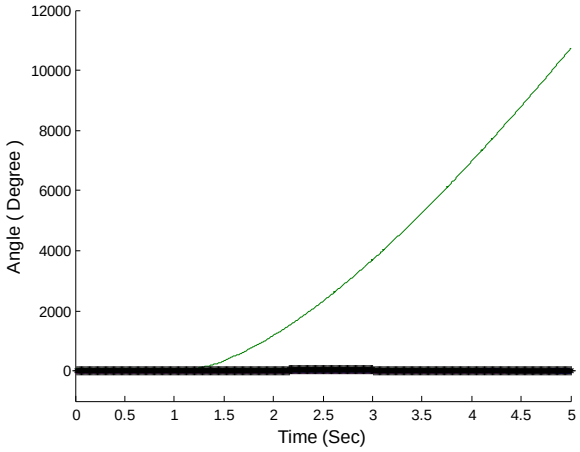
Angle (Degree)
Time (Sec)

(b)

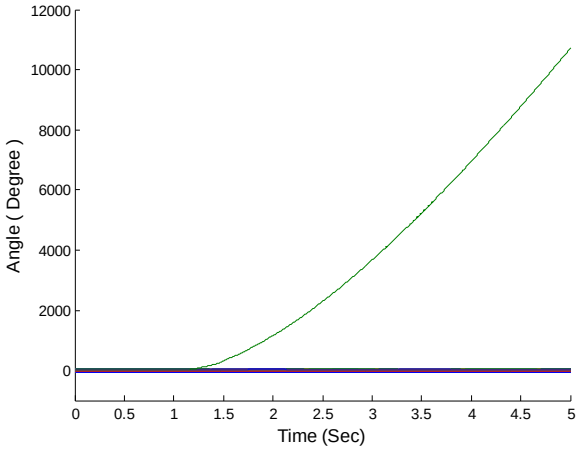
Angle (Degree)
Time (Sec)

(c)

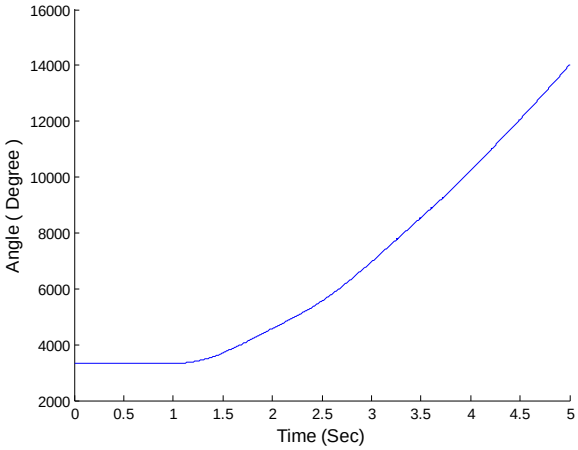
Angle (Degree)
Time (Sec)

(d)

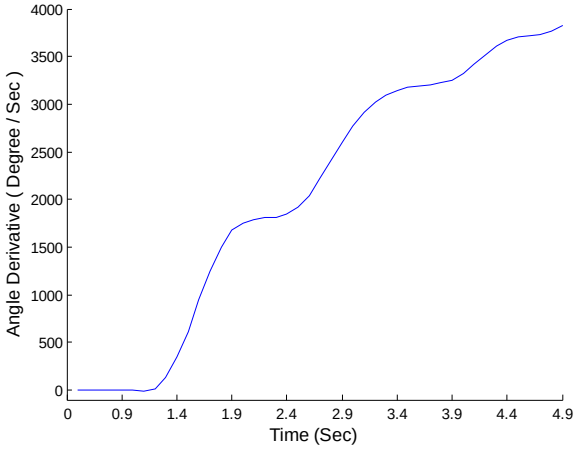
Angle Derivative (Degree / Sec)
Time (Sec)

(e)

Case 6:

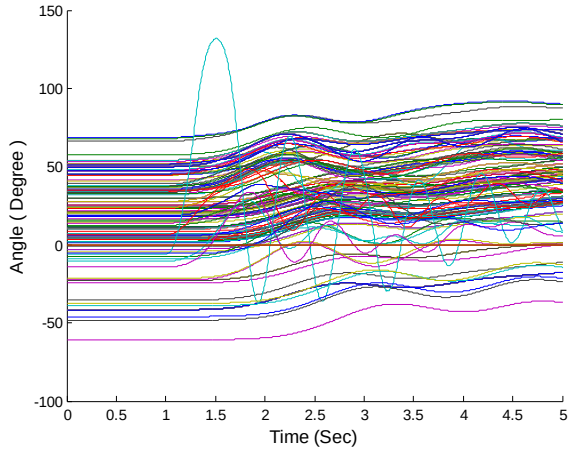
Angle (Degree)
Time (Sec)

(a)

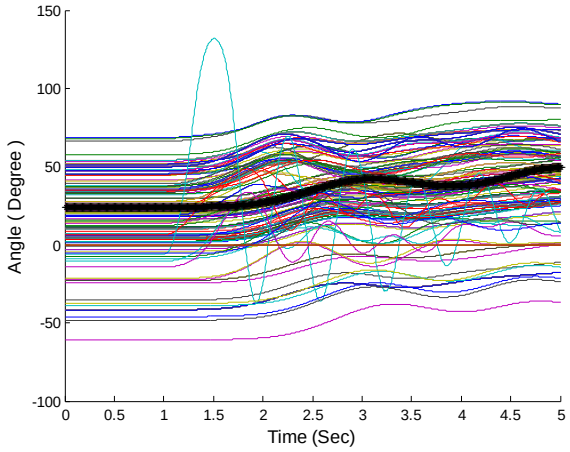
Angle (Degree)
Time (Sec)

(b)

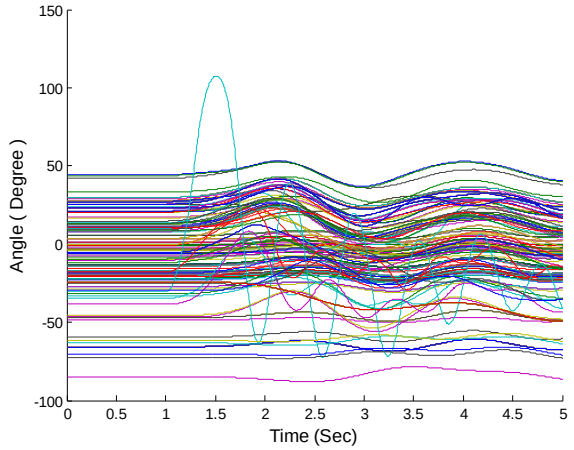
Angle (Degree)
Time (Sec)

(c)

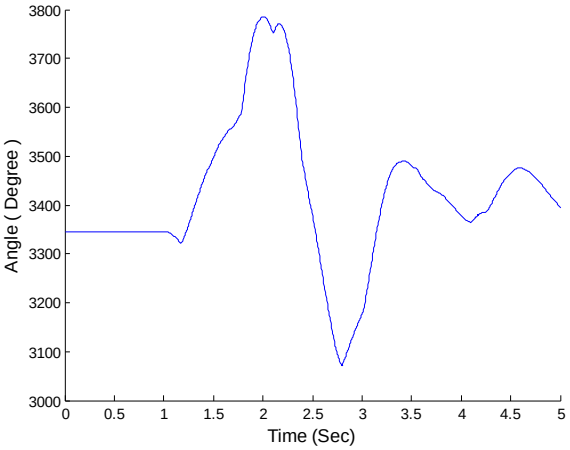
Angle (Degree)
Time (Sec)

(d)

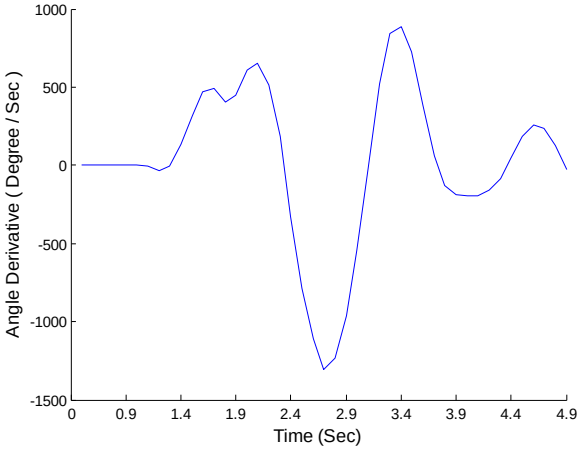
Angle Derivative (Degree / Sec)
Time (Sec)

(e)

Case 7:

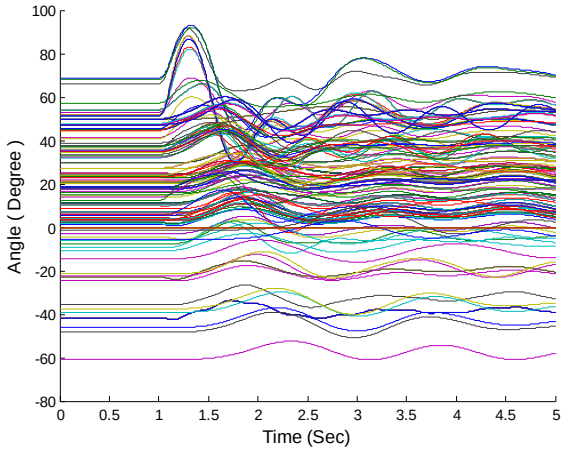
Angle (Degree)
Time (Sec)

(a)

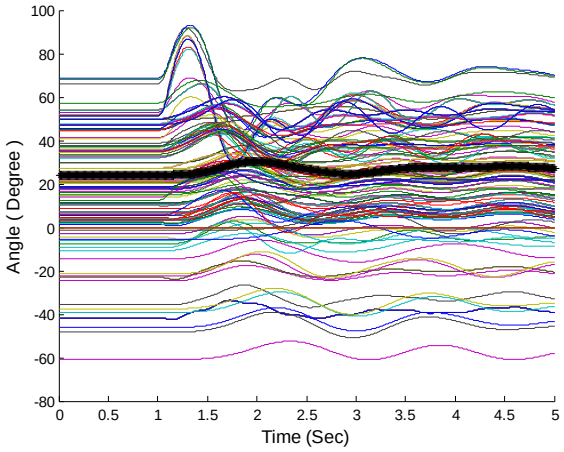
Angle (Degree)
Time (Sec)

(b)

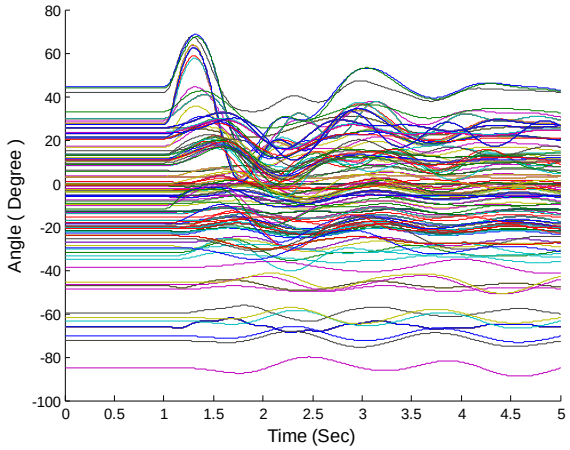
Angle (Degree)
Time (Sec)

(c)

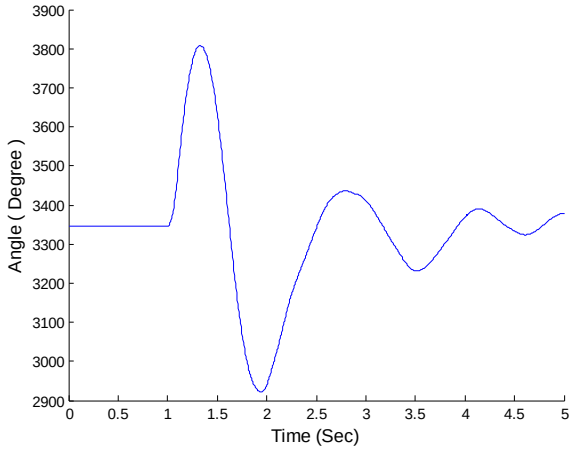
Angle (Degree)
Time (Sec)

(d)

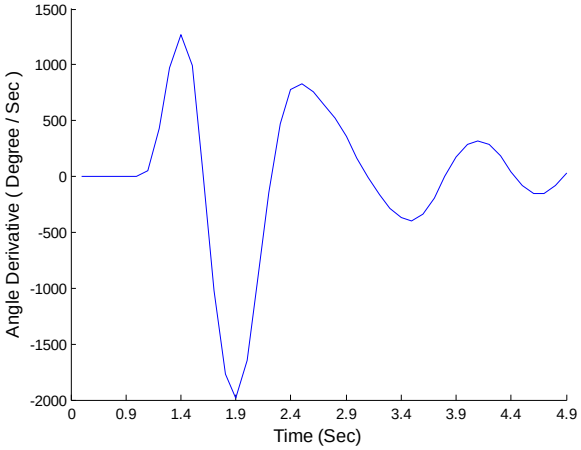
Angle Derivative (Degree / Sec)
Time (Sec)

(e)

Case 8:

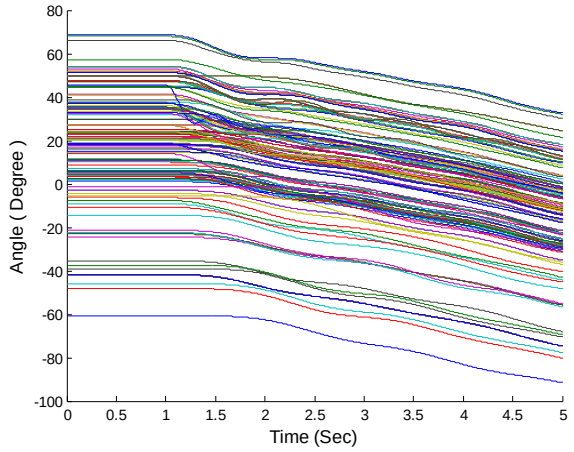
Angle (Degree)
Time (Sec)

(a)

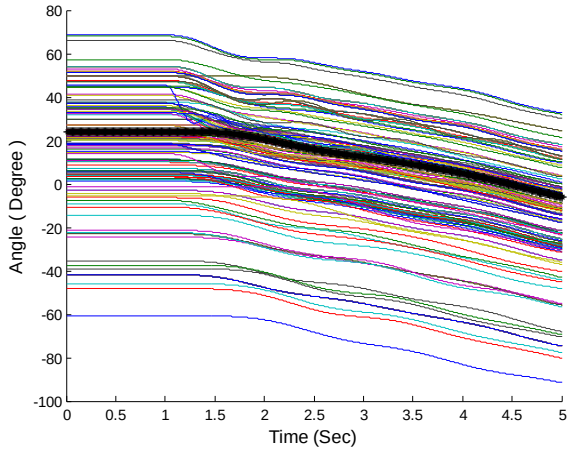
Angle (Degree)
Time (Sec)

(b)

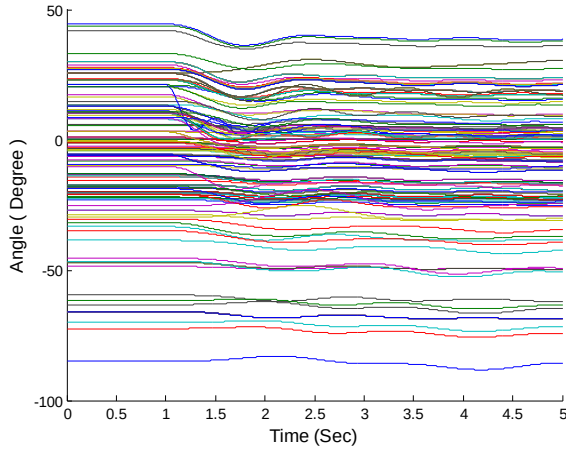
Angle (Degree)
Time (Sec)

(c)

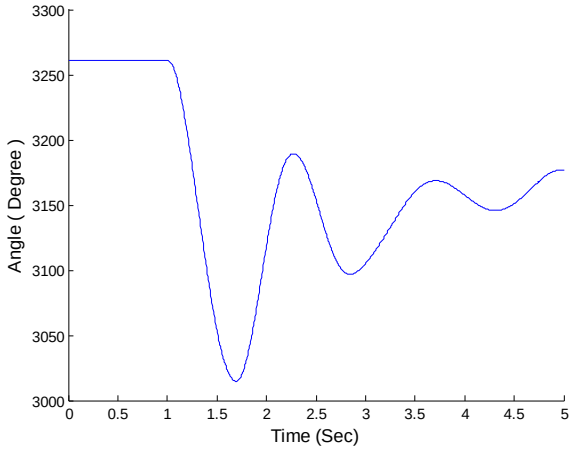
Angle (Degree)
Time (Sec)

(d)

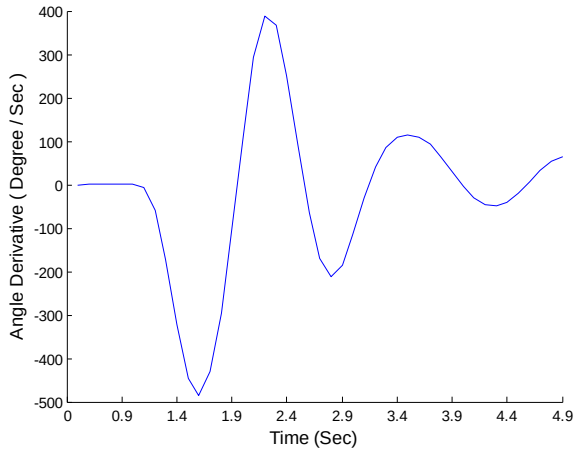
Angle Derivative (Degree / Sec)
Time (Sec)

(e)

Case 9:

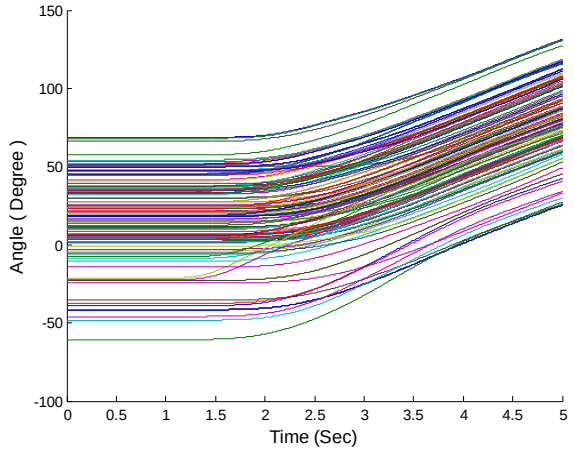
Angle (Degree)
Time (Sec)

(a)

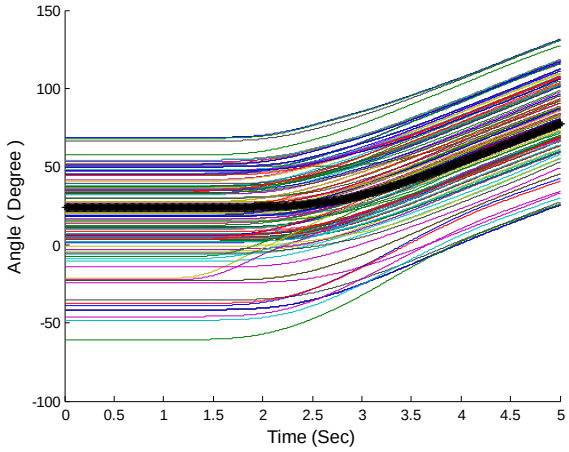
Angle (Degree)
Time (Sec)

(b)

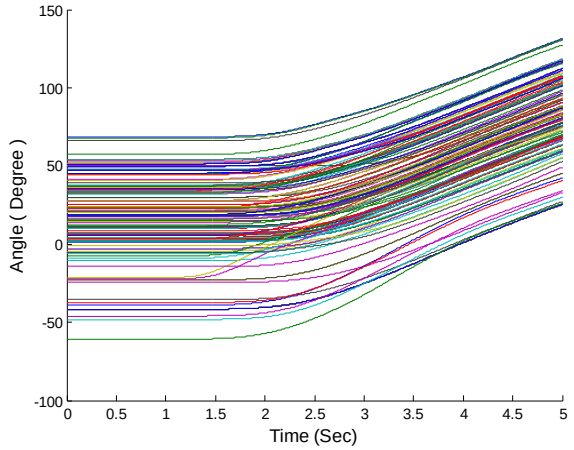
Angle (Degree)
Time (Sec)

(c)

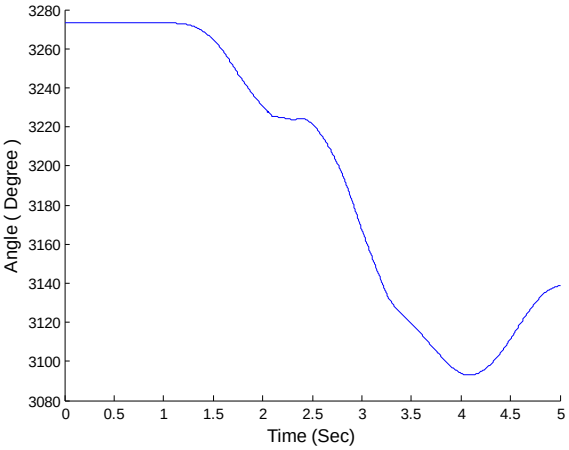
Angle (Degree)
Time (Sec)

(d)

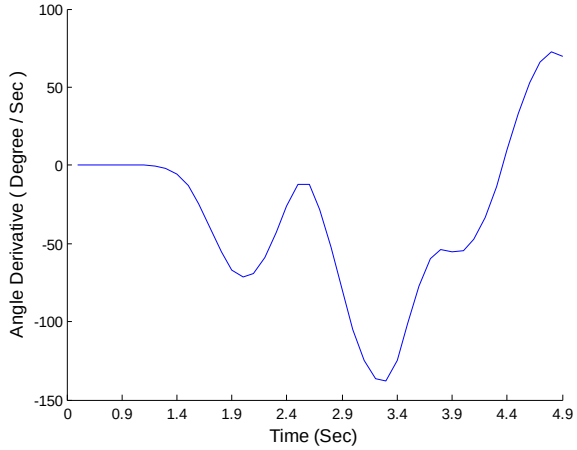
Angle Derivative (Degree / Sec)
Time (Sec)

(e)

Case 10:

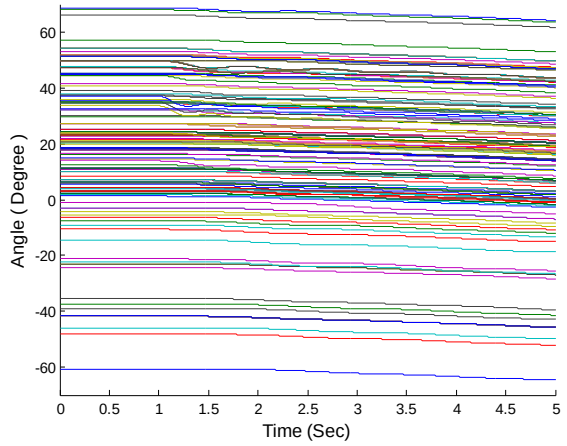

(a)

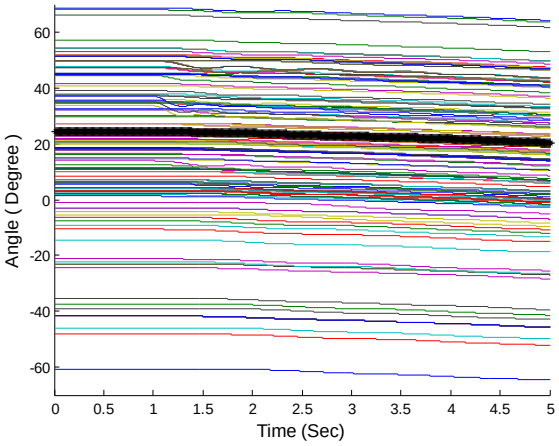

(b)

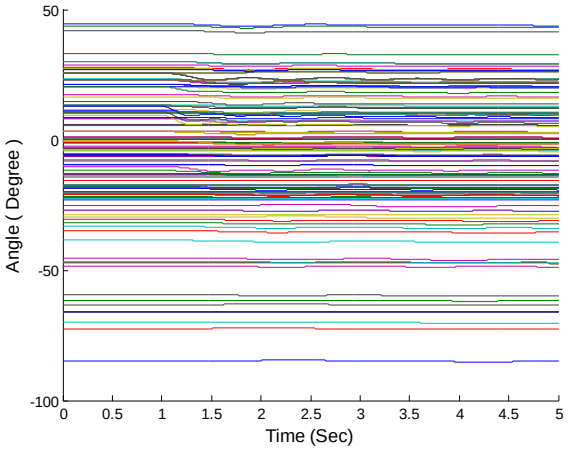

(c)

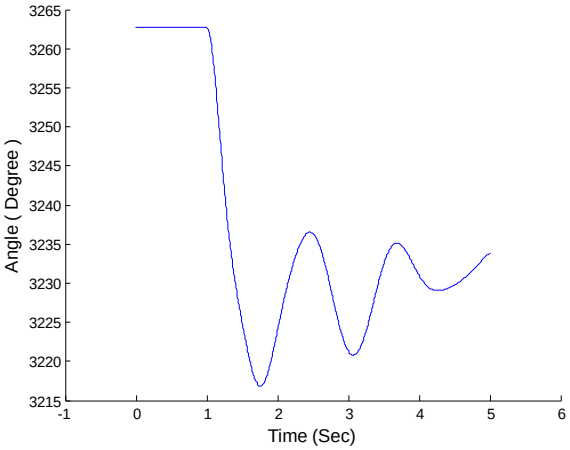

(d)

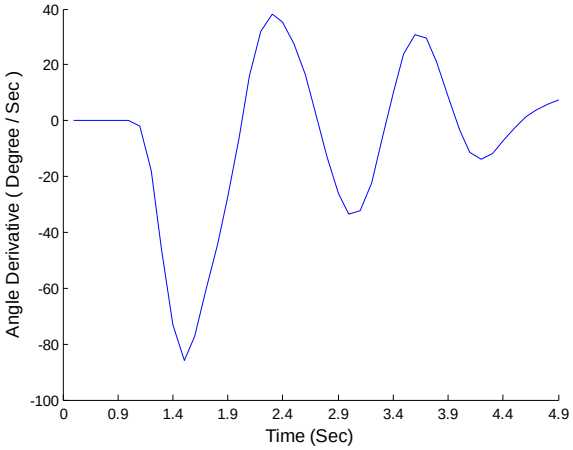

(e)

A single generator or group of generators appears unstable in cases 1 to 5, the detection algorithm reports alert at 0.2 seconds after the disturbance happens in two of the cases and 0.3 sec in the remaining three. Disturbances in cases 6 and 7 triggers great angle separation on some of the generators but they dose not lose synchronization immediately. Instead, they move into an oscillatory condition that lasted throughout the 5 seconds simulation period.

One can argue that under such circumstances, the power system is under small signal stability test and should not be alarmed as an angle instability condition. However, if the algorithm waits several seconds (most likely longer than 2 seconds) to identify an inter-area oscillation, it will lose the advantage of early situational awareness. Thus, this algorithm still activates and deactivates the instability alarm back and forth while the oscillations are big enough to exceed the thresholds. By doing that, besides the angle instability, operators will be immediately informed if the small signal instability occurs.

Table 5-III listed the algorithm response on the derivative of TAS during each case.

Table 5-III Derivative of Total-Angle-Separation in each case

Case1	Case2	Case3	Case4	Case 5	Case 6	Case 7	Case 8	Case 9	Case 10
0.00	0.00	0.00	0.00	0.00	0.00	0.00	0.00	0.00	0.00
0.00	0.00	0.00	0.00	0.00	0.00	0.00	0.00	0.00	0.00
0.00	0.00	0.00	0.00	0.00	0.00	0.00	0.00	0.00	0.00
0.00	0.00	0.00	0.00	0.00	0.00	0.00	0.00	0.00	0.00
0.00	0.00	0.00	0.00	0.00	0.00	0.00	0.00	0.00	0.00
0.00	0.00	0.00	0.00	0.00	0.00	0.00	0.00	0.00	0.00
18.95	-1.54	53.49	5.67	-5.52	-3.40	53.52	-6.45	-0.02	-2.15
205.95	5.65	512.78	169.64	15.30	-31.90	434.36	-58.82	-0.34	-17.81
741.90	133.22	1613.92	623.82	134.72	-3.56	977.73	-173.07	-1.78	-46.11
1529.05	362.35	3234.02	1279.51	343.82	133.93	1264.78	-321.06	-5.66	-73.38
2395.75	615.65	5031.27	1945.12	615.68	315.72	990.80	-446.06	-13.25	-85.82
3153.79	851.28	6698.06	2336.59	952.99	468.28	62.40	-485.98	-24.94	-77.44
3570.69	972.25	8186.31	2458.74	1249.66	490.30	-1023.37	-429.41	-39.72	-60.51
3709.96	972.97	9446.09	2460.06	1496.86	403.50	-1772.92	-297.12	-55.22	-44.54
3859.69	926.02	10605.45	2439.09	1683.62	450.05	-1985.26	-104.99	-66.75	-27.43
4158.38	846.92	11643.81	2600.59	1751.35	610.63	-1650.30	110.34	-71.52	-6.07
4815.65	810.33	12745.13	2940.47	1793.14	654.27	-935.88	293.00	-69.10	16.11
5712.11	910.05	14091.35	3572.62	1813.32	510.87	-142.87	389.38	-59.11	32.07
6903.14	1095.92	15692.30	4410.02	1809.63	183.21	470.49	368.27	-43.06	38.03
8326.06	1433.02	17548.85	5262.23	1853.53	-324.35	783.48	252.16	-25.98	35.47

9759.01	1928.22	19572.33	6024.18	1919.32	-790.05	834.50	90.35	-11.99	27.69
10933.61	2431.57	21565.20	6587.48	2044.97	-1112.47	755.51	-63.73	-12.29	16.49
11540.11	2840.03	23343.55	6950.50	2215.52	-1303.06	645.85	-170.79	-28.13	2.44
11843.08	3028.73	24882.46	7149.37	2409.87	-1231.17	520.92	-211.39	-52.16	-12.95
11979.59	3003.53	26147.12	7208.06	2608.48	-960.16	354.68	-185.97	-80.04	-26.31
12090.20	2831.15	27233.65	7134.33	2776.17	-542.67	162.53	-115.08	-104.98	-33.62
12240.27	2575.85	28272.69	7008.57	2912.97	-19.18	-12.50	-30.31	-124.81	-32.32
12423.13	2332.96	29439.47	6890.85	3024.09	518.15	-162.96	40.43	-136.27	-22.50
12713.52	2180.58	30840.91	6867.31	3099.55	844.57	-286.29	85.68	-137.93	-6.93
13133.29	2122.52	32450.85	6979.26	3144.71	884.75	-370.08	108.48	-124.75	10.03
13718.24	2116.71	34170.93	7218.43	3174.20	723.37	-398.68	115.53	-101.43	23.76
14468.23	2141.66	35898.27	7568.02	3191.47	380.51	-337.42	110.12	-77.43	30.69
15253.00	2261.62	37584.74	7977.95	3207.03	59.70	-193.57	92.26	-59.62	29.41
15967.32	2537.75	39237.05	8399.92	3223.82	-127.16	-3.60	64.04	-54.11	21.01
16531.04	2901.68	40857.29	8785.88	3252.45	-187.88	176.85	30.30	-55.46	8.72
16901.36	3218.88	42440.31	9082.09	3317.61	-198.17	290.03	-2.81	-54.38	-3.24
17140.14	3386.74	43958.88	9264.27	3413.91	-191.81	321.99	-29.70	-47.62	-11.34
17337.13	3384.50	45370.78	9334.77	3519.10	-161.29	284.16	-46.08	-33.66	-14.01
17581.14	3285.45	46662.08	9333.03	3610.80	-87.69	182.88	-49.43	-13.46	-11.98
17924.49	3170.61	47868.40	9304.47	3671.47	43.55	44.07	-39.73	9.82	-7.43
18366.12	3095.17	49079.36	9284.56	3702.05	187.08	-82.75	-19.74	33.03	-2.63
18806.77	3081.11	50380.81	9298.15	3717.07	257.31	-153.61	5.89	52.59	1.14
19169.14	3111.84	51825.37	9356.76	3734.84	233.36	-148.82	31.81	66.17	3.74
19433.02	3159.44	53390.39	9460.56	3769.82	124.77	-77.14	52.66	72.24	5.67
19623.37	3220.45	55047.61	9596.76	3826.72	-26.74	26.61	63.46	69.67	7.29

Normal Warning Alert

5.4 Algorithm eligibility in small system

The development of the TAS algorithm is based on the assumption that the generator inertia can be equally distributed to each machine of the system. When the system is large, meaning that $H_i << H_T$, the assumption is obviously valid. But if the system is small, from (5-2) the CBA will lean towards the generators that have higher inertia constants. Even still, the proposed CBA approach can still effectively detect angle instability conditions because of the fact it calculates the Total-Angle-Separation. The position of CBA relatively to each bus angle could barely influence the value of TAS.

A four machine, 11 bus system from Kundur's book [] is used to test the CBA in a small system. The system structure and parameters of the PSS/E model are included in the appendix.

A bus fault is applied to Bus 8 at 1 second after the simulation starts and is cleared at 1.3 second. Lines 2, 3, 4 that connecting Bus 7 and Bus 8 are disconnected at 1.3 second as well. The voltage angles on four generator buses separate into two groups about 1 second after the disturbance, when the derivative of TAS start increasing.

Each figure marks stands for:

(a) Voltage angles in each generation bus

(b) Bus angles and Center-of-Bus-Angles (dark black line)

(c) Bus angle separations from the CBA

(d) The Total-Angle-Separation

(e) The derivative of the Total-Angle-Separation

The algorithm responses to the angle separation speeds through the simulation period are displayed in Table 5-IV.

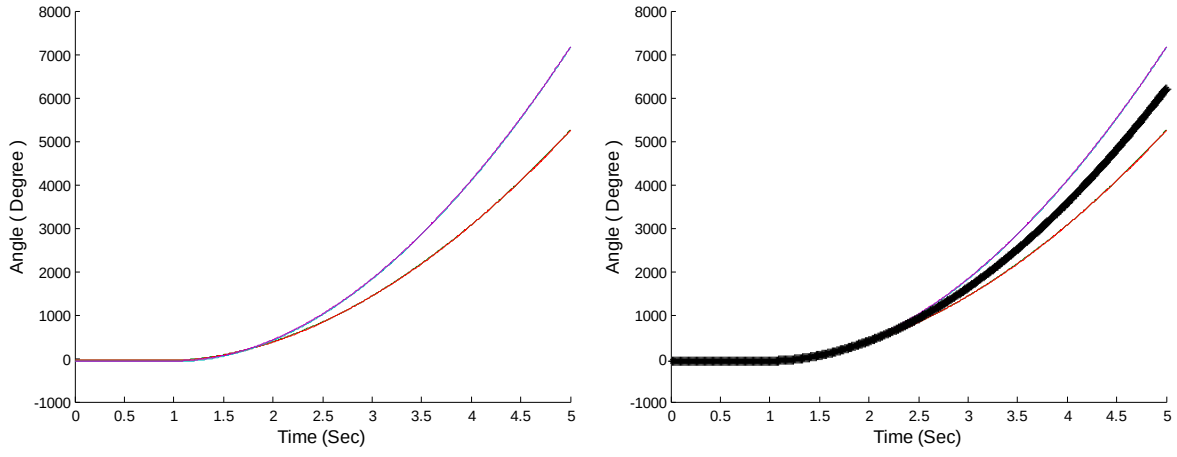

(a)

(b)

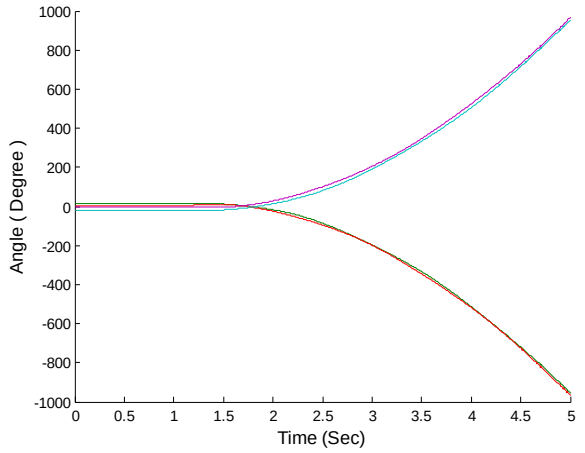

(c)

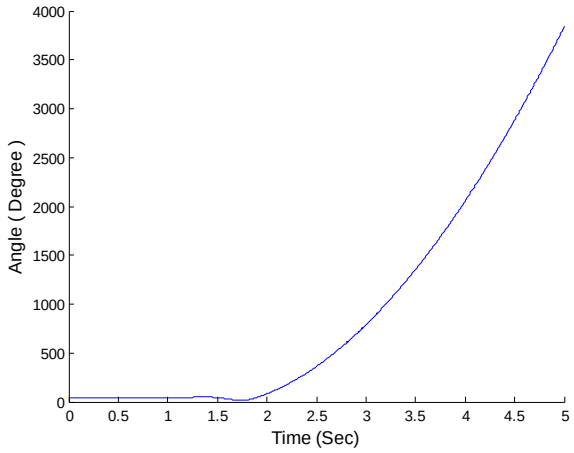

(d)

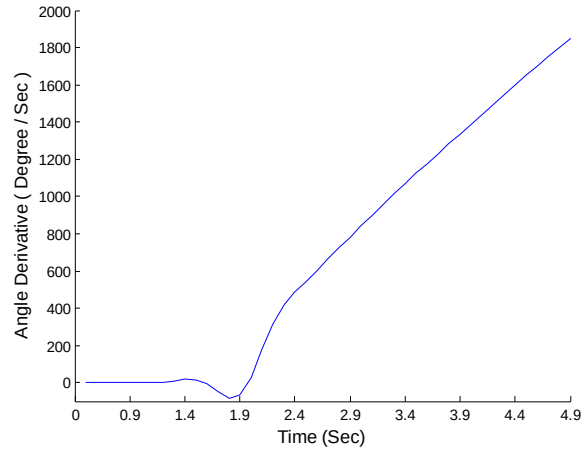

(e)

Table 5-IV Derivative of Total-Angle-Separation

Time (Sec)	Derivative of TAS (Degree/s)
0.5	0.006967283
0.6	0.008913944
0.7	0.01017796
0.8	0.010744138
0.9	0.010658271
1	0.010008896
1.1	0.270759351
1.2	2.56770951
1.3	8.491940054

1.4	16.70483345
1.5	15.8434606
1.6	-5.258262332
1.7	-46.70667398
1.8	-85.36134486
1.9	-69.24262732
2	26.91331932
2.1	170.9092178
2.2	313.2847167
2.3	416.0944651
2.4	483.4299357
2.5	543.9748252
2.6	604.2398735
2.7	664.308142
2.8	724.1566796
2.9	783.635866
3	842.5186831
3.1	900.5887038
3.2	957.7192269
3.3	1013.88746
3.4	1069.135522
3.5	1123.530997
3.6	1177.15816
3.7	1230.150573
3.8	1282.724783
3.9	1335.156314
4	1387.691477

Normal Warning Alert

5.5 A WECC angle separation case

Testing the algorithm with actual system data is an issue because that the probability of an unstable condition occurring in a real system is very low. However, the FNET system has recorded an islanding that happened in WECC system at roughly 23:37:00 UTC, 06/01/2010. Islanding is a special type of instability in the sense that at its initial stage, the rotor angles of a group of generators start to separate from the rest of the system. After a certain amount of time, the rotor speed within the group regain synchronism usually because they are physically

separated from the rest of the system. Therefore, it can be identified as an unstable situation by the CBA algorithm.

Each figure marks stands for:

(a) Voltage angles in each generation bus

(b) Bus angles and Center-of-Bus-Angles (dark black line)

(c) Bus angle separations from the CBA

(d) The Total-Angle-Separation

(e) The derivative of the Total-Angle-Separation

The algorithm responses to the angle separation speeds through the simulation period are displayed in Table 5-V .

As illustrated in (e), the angle separation is accelerating at the beginning, and then changed into a steady rate, which means the islanded area began to settle down at a different synchronous speed, but because of its difference from the rest of the interconnection, the angle separations between them is still increasing.

Different thresholds have been used for the WECC case. TH1 has been set to 5 degree/s and TH2 is 10 degree/s. The thresholds are system dependent variables that can be affected by the size (MVA) of the system and the number of observable generation buses.

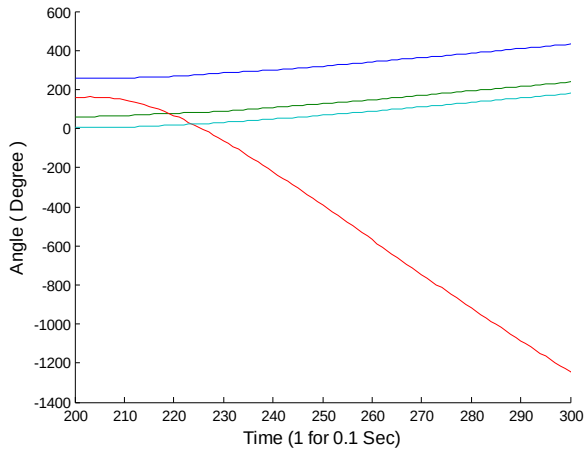

(a)

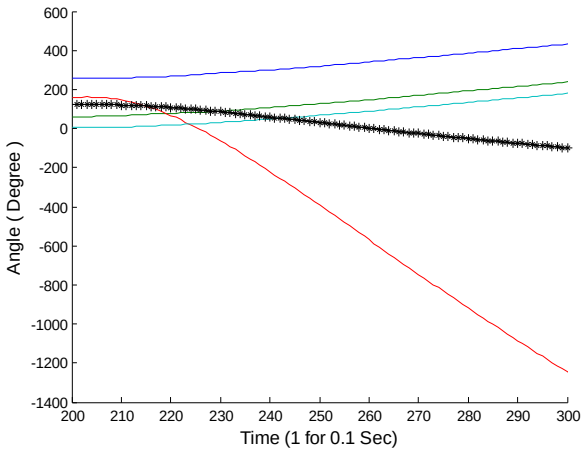

(b)

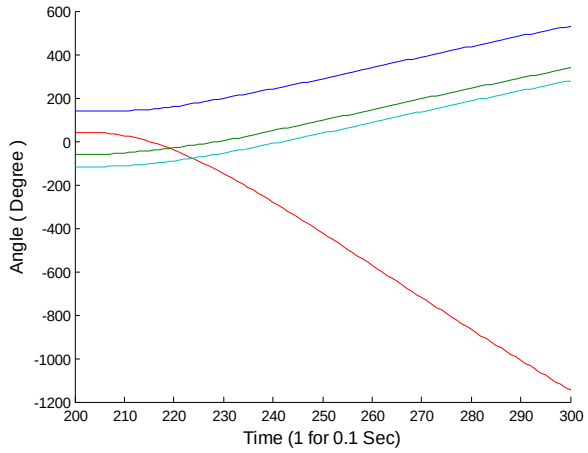

(c)

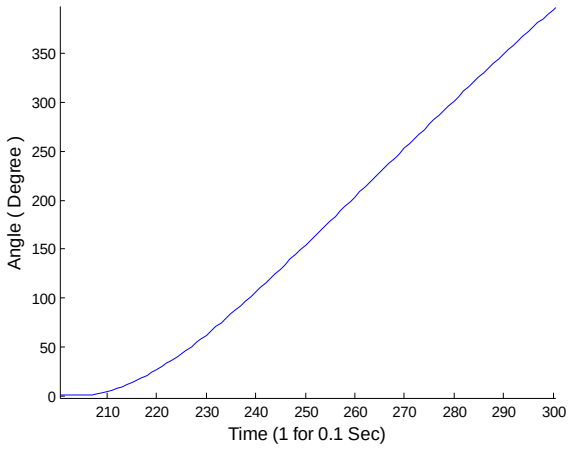

(d)

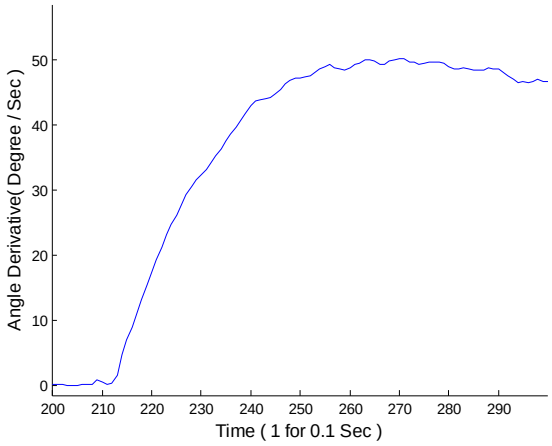

(e)

Table 5-V Derivative of Total-Angle-Separation

Time (Sec)	Angle Derivative (Degree / s)
199	-0.140369886
200	0.028641438
201	0.010024797
202	0.13464608
203	0.807874988
204	0.475561419
205	0.0386641
206	0.209124171
207	1.522618854
208	4.573634367
209	6.865472967

210	8.890867595
211	10.92917416
212	13.01903478
213	15.26932588
214	17.27754962
215	19.12533244
216	21.14213853
217	23.08303923
218	24.62857914
219	26.10538599
220	27.6423523
221	29.14062643
222	30.37679505
223	31.40953801
224	32.1930717
225	33.12413491
226	34.1378384
227	35.24344289
228	36.17018515
229	37.40082724

Normal Warning Alert

5.6 Summary

This chapter introduced a method that calculates the center of generation bus voltage angles and searches for the point that bus angles are separating from this center, in order to detect an angle unstable situation at its early stage.

Because this CBA approach utilizes wide-area phasor measurement data, in particular the voltage angle data from generation buses in particular, it has fast response to the events.

It is reliable in a sense that it not only alarms the first swing angle instability but also for system-wide oscillations that could lead to small signal instability. Also, this method calculates the Total Angle Separation instead of tracking single buses to minimize the influence of the inertia distributions and separate group sizes.

It is also a secure method. When the system re-balanced from a sudden disturbance, the Derivative of TAS, will return to near zero even the TAS could be higher than it is in the early equilibrium. The alarm of unstable detection will be muted under such circumstances.

5.7 Conclusion and future work

The CBA based unstable detection algorithm will effectively detect the early separation of the voltage phase angle, thus alerting to the appearance of angular instability within the system.

Upon the detection of an angle instability event, the individual angle separation rates $\frac{d(\delta_i - \delta_{CBA})}{dt}$ can be calculated. Those buses that display similar results can be grouped together as separating from the rest of the system. The next step of development should be identifying the unstable groups.

References

[1] P. Bonanomi, "Phase angle measurements with synchronized clocks-principle and applications," *IEEE Trans. Power Apparatus and Systems*, vol. PAS-100, issue 12, Page(s): 5036 – 5043, Dec. 1981.

[2] A.G. Phadke, J.S. Thorp, Synchronized Phasor Measurements and Their Applications, New York: Springer, 2008, p.4.

[3] V. Venkatasubramanian, H. Schattler, J. Zaborszky, "Fast time-varying phasor analysis in the balanced three-phase large electric power system," *IEEE Trans. Automatic Control*, vol. 40, issue 11, Page(s): 1975 – 1982, Nov. 1995.

[4] J.H. Chow, L. Vanfretti, A. Armenia, S. Ghiocel, S. Sarawgi, N. Bhatt, D. Bertagnolli, M. Shukla, Xiaochuan Luo, D. Ellis, D. Fan, M. Patel, A.M. Hunter, D.E. Barber, G.L. Kobet, "Preliminary synchronized phasor data analysis of disturbance events in the US Eastern Interconnection," in *Proc. 2009 IEEE Power Engineering Society Power Systems Conference and Exposition*, Page(s): 1-8.

[5] Qiu Bin, Ling Chen, V. Centeno, X. Z. Dong, Yilu Liu, "Internet based frequency monitoring network (FNET)," in *Proc. 2001 IEEE Power Engineering Society Winter Meeting*, Page(s): 1166-1171.

[6] Zhian Zhong, Chunchun Xu, B.J. Billian, Li Zhang, S.-J.S. Tsai, R.W. Conners, V.A. Centeno, A.G. Phadke, Yilu Liu, "Power system frequency monitoring network (FNET) implementation," *IEEE Trans. Power Systems*, vol. 20, issue 4, Page(s): 1914 – 1921, Nov. 2005.

[7] Yilu Liu, "A US-wide power systems frequency monitoring network," in *Proc. 2006 IEEE Power Engineering Society General Meeting*, Page(s): 8.

[8] R.M. Gardener, Yilu Liu, "FNET: a quickly deployable and economic system to monitor the electric grid," *in Proc. 2007 IEEE Conference on Technologies for Homeland Security*, Page(s): 209-214.

[9] Y.J. Shin, A.C. Parsons, E.J. Powers, W.M. Grady, "Time-frequency Analysis of Power System Disturbance Signals for Power Quality," in *Proc. 1999 IEEE Power Engineering Society Summer Meeting*, pp 402 – 407.

[10] H. Karimi, etc., "Estimation of Frequency and its Rate of Change for Applications in Power Systems", *IEEE Trans. on Power Delivery*, vol. 19, No. 2, pp 472-480, April, 2004.

[11] Lei Wang, J. Burgett, Jian Zuo, Chunchun Xu, B.J. Billian, R.W. Conners, Yilu Liu, "Frequency disturbance recorder design and developments," in *Proc. 2007 IEEE Power Engineering Society General Meeting*, Page(s): 1-7.

[12] Chunchun Xu, Zhian Zhong, V.A. Centeno, R.W. Conners, Yilu Liu, "Practical issues in frequency disturbance recorder design for wide-area monitoring, " *Electrical Power Quality and Utilisation, Journal*, vol. XI, No. 1, Page(s): 69-76, 2005.

[13] R.M. Gardner, J.N. Bank, J.K. Wang, A.J. Arana, Yilu Liu, "Non-parametric power system event location using wide-area measurements," in *Proc. 2006 IEEE Power Systems Conference and Exposition*, Page(s): 1668-1675.

[14] J.N. Bank, R.M. Gardner, J.K. Wang, A.J. Arana, Yilu Liu, "Generator Trip Identification Using Wide-Area Measurements and Historical Data Analysis," in *Proc. 2006 IEEE Power Systems Conference and Exposition*, Page(s): 1677-1681

[15] R.M. Gardner, J.K. Wang, Yilu Liu, "Power system event location analysis using wide-area measurements," in *Proc. 2006* Power Engineering Society General Meeting, Page(s): 7..

[16] Jian Zuo, Zhian Zhong, R.M. Gardner, Hengxu Zhang, Yilu Liu, "Off-line event filter for the wide area frequency measurements," in *Proc. IEEE 2006 Power Engineering Society General Meeting*, Page(s): 6.

[17] S.S. Tsai, Zhian Zhong, Jian Zuo, Yilu Liu, "Analysis of wide-area frequency measurement of bulk power systems," in *Proc. 2006 IEEE Power Engineering Society General Meeting*, Page(s): 8.

[18] J.K. Wang, R.M. Gardner, Yilu Liu, "Analysis of system oscillations using wide-area measurements," in *Proc. 2006 IEEE Power Engineering Society General Meeting*, Page(s): 6.

[19] J.N. Bank, R.M. Gardner, S.-J.S., Tsai, Kyung Soo Kook, Yilu Liu, "Visualization of wide-area frequency measurement information," in *Proc. 2007 IEEE Power Engineering Society General Meeting*, Page(s): 1-8.

[20] Jian Zuo, M. Baldwin, Hengxu Zhang, Jingyuan Dong, Kyung Soo Kook, Yilu Liu, "Use of frequency oscillations to improve event location estimation in power systems," in *Proc. 2007 IEEE Power Engineering Society General Meeting*, Page(s): 1-7.

[21] Jingyuan Dong, Jian Zuo, Lei Wang, Kyung Soo Kook, II-Yop Chung, Yilu Liu, S. Affare, B. Rogers, M., Ingram, "Analysis of power system disturbances based on wide-area frequency measurements," in *Proc. 2007 IEEE Power Engineering Society General Meeting*, Page(s): 1-8.

[22] R.M. Gardner, Wei Li, J. West, Jingyuan Dong, Yilu Liu, Guorui Zhang, "Power system frequency oscillation characteristics," in *Proc. 2008 IEEE Power Engineering Society General Meeting*, Page(s): 1-7.

[23] Jian Zuo, R. Carroll, P. Trachian, Jingyuan Dong, S. Affare, B. Rogers, L. Beard, Yilu Liu, "Development of TVA SuperPDC: Phasor applications, tools, and event replay," in *Proc. 2008 IEEE Power Engineering Society General Meeting*, Page(s): 1-8.

[24] Jingyuan Dong, Tao Xia, Yingchen Zhang, T. Weekes, J.S. Thorp, Yilu Liu, "Monitoring power system disturbances at the distribution level," in *Proc. 2008 IEEE Power Engineering Society General Meeting*, Page(s): 1-8.

[25] Jingyuan Dong, Tao Xia, Yingchen Zhang, Lei Wang, Yilu Liu, L. Beard, T. Bilke, "Wide-area measurements of three north America interconnections at distribution level," *Proc. 2009 Power Systems Conference and Exposition*, Page(s): 1-8.

[26] Wei Li, R.M. Gardner, Jingyuan Dong, Lei Wang, Tao Xia, Yingchen Zhang, Yilu Liu, Guorui Zhang, Yusheng Xue, "Wide area synchronized measurements and inter-area oscillation study," *Proc. 2009 Power Systems Conference and Exposition*, Page(s): 1-8.

[27] R.M. Gardener, Zhian Zhong, Yilu Liu, "Location determination of power system disturbances based on frequency responses of the system," U.S. Patent 7 519 454, April 14, 2009.

[28] J.S. Thorp, C.E. Seyler, A.G. Phadke, "Electromechanical wave propagation in large electric power systems," *IEEE Transactions on Circuits and Systems I: Fundamental Theory and Applications*, vol. 45, issue 6, Page(s): 614 – 622, June, 1998.

[29] A. G. Phadke, J.S. Thorp, "History and Application of Phasor Measurements", *IEEE PSCE 2006*. Page(s):331-335.

[30] A. G. Phadke, "Synchronized phasor measurements ~ A historical overview", Transmission and Distribution Conference and Exhibition 2002: Asia Pacific, 2002. Page(s): 476-479.

[31] W.T.Kaune, L. Zaffanella, "Analysis of magnetic fields produced far from electrical power lines", Transmission and Distribution Conference, 1991. Page(s): 735 – 742.

[32] G.B. Iyyuni, S.A. Sebo, " Study of transmission line magnetic fields", Power Symposium, 1990. Proceedings of the Twenty-Second Annual North American 15-16 Oct. 1990. Page(s):222 – 231.

[33] IEEE STD 664 "IEEE Standard Procedures for Measurement of Power Frequency Electric and Magnetic Fields From AC Power Lines", 1994, Reaffirmed 2008.

[34] "Transmission Line Reference Book, 345kV and Above/Second Edition", EPRI, 1982.

[35] "Northeast Utilities Overhead Transmission Line Standards", 2008

[36] "American Electric Power Interstate Project Proposed Land Use & Environmental Mitigations", January 31, 2006, AEP.

[37] "KlondikeIII/Biglow Canyon Wind Integration Project. Appendix C: Electrical Effects", T. Dan Bracken, Inc, March 2006.

[38] "Transmission right of way clearing and maintenance", AEP Texas. http://www.appalachianpower.com/news/reliability/.

[39] Chunchun Xu, "High Accuracy Real-time GPS Synchronized Frequency Measurement Device for Wide-area Power Grid Monitoring", Doctor of Philosophy Dissertation, February 2006.

[40] Lei Wang, Jon Burgett, Jian Zuo, Chunchun Xu, Bruce J. Billian, Richard W. Conners, and Yilu Liu, "Frequency Disturbance Recorder Design and Developments", Power Engineering Society General Meeting, 2007. IEEE, June 2007

[41] Bin Qiu, Ling Chen, Centeno, V., Xuzhu Dong, Yilu Liu, "Internet based frequency monitoring network (FNET)", Power Engineering Society Winter Meeting. IEEE Volume 3, 28 Jan.-1 Feb. 2001. Page(s):1166 – 1171.

[42] Jonathan W. Stahlhut, Gerald T. Heydt, Elias Kyriakides,"Innovative Sensory Concepts for Power Systems", Power Symposium, 2006. NAPS 38th North American, 2006.

[43] Y.J. Shin, A.C. Parsons, E.J. Powers, W.M. Grady, "Time-frequency Analysis of Power System Disturbance Signals for Power Quality," in Proc. 1999 IEEE Power Engineering Society Summer Meeting, pp 402 – 407.

[44] Robert Matthew Gardner, "A Wide-Area Perspective on Power System Operation and Dynamics", Doctor of Philosophy Dissertation, March 2008.

[45] IEEE Std 1344-1995, "IEEE Standard for Synchrophasors for Power systems"1995, Reaffirmed 2005.

[46] Miller, C. J., "The measurements of electric fields in live line working," IEEE Transactions on Power Apparatus and Systems, vol. PAS-86, Apr, 1967. Page(s): 493–498.

[47] Bracken, T.D.; "Field measurements and calculations of electrostatic effects of overhead transmission lines", Power Apparatus and Systems, IEEE Transactions on. Volume 95, Issue 2, Mar 1976. Page(s):494 – 504

[48] Yilu Liu, L.E. Zaffanella, "Calculation of electric field and audible noise from transmission lines with non-parallel conductors", IEEE Transactions on Power Delivery, Volume 11, Issue 3, July 1996, Page(s):1492 – 1497

[49] Melo, M.O.B.C.; Fonseca, L.C.A.; Fontana, E.; Naidu, S.R.; "Electric and Magnetic Fields of Compact Transmission Lines", Power Delivery, IEEE Transactions on. Volume 14, Issue 1, Jan, 1999. Page(s):200 – 204

[50] Gerrard, C.A.; Gibson, J.R.; Jones, G.R.; Holt, L.; Simkin, D.; "Measurements of power system voltages using remote electric field monitoring", Generation,Transmission and Distribution, IEE Proceedings-Volume 145, Issue 3, May 1998. Page(s):217 - 224

[51] Sorchini, Z.; Krein, P.T.; "Live Power Line and Lead Proximity Estimation via Real-Time Electric Field Sensor", Power Electronics Specialist Conference, IEEE 34th Annual Volume 2, June, 2003. Page(s):907 - 912

[52] Wijeweera, G.; Shafai, C.; Rajapakse, A.; "Measuring power system voltage remotely using micromachined electric field sensor", Microsystems and Nanoelectronics Research Conference, Oct, 2008. Page(s):209 – 212

[53] Indira Nair, M. G. Morgan, H. K. Florig, "Biological Effects of Power Frequency Electric and Magnetic Fields", Department of Engineering and Public Policy, Carnegie Mellon University, May 1989

[54] Yilu Liu, L.E. Zaffanella, "Calculation of electric field and audible noise from transmission lines with non-parallel conductors", IEEE Trans. on Power Delivery, Volume 11, Issue 3, Jul 1996, Page(s): 1492–1497.

[55] H. Singer, H. Steinbigler, P. Weiss, "A charge simulation method for the calculation of high voltage fields", IEEE Trans. on Power Apparatus and Systems, Volume PAS-93, Issue 5, Sept. 1974, Page(s): 1660–1668.

[56] E. G. Lambert, "Measurement of electric and magnetic fields from alternating current power lines", IEEE Transactions on Power Apparatus and Systems, Volume PAS-97, No. 4, July/Aug 1978, Pages(s): 1104-1113.

[57] T. Keikko, J. Isokorpi, L. Korpinen, "Practical problems in calculating electric fields of transmission lines", Eleventh International Symposium on High Voltage Engineering, 1999, Page(s): 103 – 106.

[58] IEEE Standard Procedures for Measurement of Power Frequency Electric and Magnetic Fields from AC Power Lines, IEEE STD 664, 1994, Reaffirmed 2008.

[59] "Relative permittivity", http://en.wikipedia.org/wiki/Relative_permittivity

[60] Sawa, T.; Kurosawa, K.; Kaminishi, T.; Yokota, T. "Development of optical instrument transformers" Power Delivery, IEEE Transactions on Volume 5, Issue 2, April 1990. Page(s):884-891.

[61] Rahmatian, F.; Chavez, P.P.; Jaeger, N.A.F.; "138 kV and 345 kV Wide-Band SF6-Free Optical Voltage Transducers" Power Engineering Society Winter Meeting, 2002. IEEE Volume 2, Jan. 2002. Page(s):1472 - 1477

[62] Rahmatian, F.; Chavez, P. P.; Jaeger, N. A. F.; "230 kV Optical Voltage Transducers Using Multiple Electric Field Sensors" Power Engineering Review, IEEE. Volume 22, Issue 2, Feb. 2002. Page(s):61 - 61

[63] Jaeger, N.A.F.; Rahmatian, F.; "Integrated optics Pockels cell high-voltage sensor" Power Delivery, IEEE Transactions on. Volume 10, Issue 1, Jan. 1995. Page(s):127 – 134

[64] Mihailovic, P.; Petricevic, S.; Stojkovic, Z.; Radunovic, J.B.; "Development of a Portable Fiber-Optic Current Sensor for Power Systems Monitoring" Instrumentation and Measurement, IEEE Transactions on. Volume 53, Issue 1, Feb, 2004. Page(s):24 – 30

[65] Farnoosh Rahmatian; Nicolas A. F. Jaeger; "US Patent 6946827 - Optical electric field or voltage sensing system", Nov, 2002.

[66] Paul A. Zank; Eldon M. Sutphin; David W. Buchanan; Thomas G. Cehelnik; "US Patent 6922059 - Electric field sensor", Dec, 2002.

[67] Bruce C. Beihoff; Charles J. Tennies; Jerome K. Hastings; "US Patent 5206596 - Arc detector transducer using an E and B field sensor", Mar, 1991.

[68] William J. McNulty; "US Patent 6329924 - Wearable electric field detector", Mar, 2000.

[69] Bahreyni, B.; Wijeweera, G.; Shafai, C.; Rajapakse, A.; "Design and Testing of a Field-Chopping Electric Field Sensor using Thermal Actuators with Mechanically Amplified Response", Solid-State Sensors, International Actuators and Microsystems Conference, June 2007. Page(s):1397 - 1400

[70] Jonathan W. Stahlhut, Gerald T. Heydt, Elias Kyriakides,"Innovative sensory concepts for power systems", Power Symposium, 2006. NAPS 38th North American, 2006.

[71] "Relative permittivity", http://en.wikipedia.org/wiki/Relative_permittiv ity

[72] YongJune Shin, A.C. Parsons A.C., E.J. Powers, W. M. Grady, "Time-frequency analysis of power system disturbance signals for power quality", *Power Engineering Society Summer Meeting, 1999. IEEE, Volume 1, 18-22 July 1999.* Page(s):402 – 407.

[73] A. G. Phadke, J.S. Thorp, M.G. Adamiak, "A new measurement technique for tracking voltage phasors, local system frequency, and rate of change of frequency", *IEEE Trans. Power Apparatus and Systems, Volume PAS-102, Issue 5, 1983.* Page(s):1025-1038.

[74] Jian Chen, "Accurate Frequency Estimation with Phasor Angles", Master of Science thesis, April, 1994.

[75] M.S. Baldwin, H.S. Schenkel, "Determination of Frequency Decay Rates During Periods of Generation Deficiency", IEEE Transaction on Power Apparatus and Systems, Vol PAS-95, No. 1, January/February 1976, Page(s): 26-36.

[76] M.S. Sachdev, M.M. Giray, "A Least Error Squares Technique for Determining Power System Frequency", IEEE Transactions on Power Apparatus and Systems, Vol. PAS-104, No. 2, February 1985, Page(s): 437-443.

[77] "Non-linear least squares", http://en.wikipedia.org/wiki/Non-linear_least_squares.

[78] Åke Björck, Numerical methods for least squares problems, SIAM, 1996.

[79] George A. F. Seber, C. J. Wild, Nonlinear Regression, Wiley Series in Probability and Statistics, 2003

[80] "Matlab Curve fitting toolbox user's guide", The Mathwork Inc.

[81] K. Madsen, H.B. Nielsen, O. Tingleff, Methods for non-linear least squares problems, 2nd Edition, Informatics and Mathematical Modelling Technical University of Denmark, April 2004.

[82] "Matlab help: lsqcurvfit", http://www.mathworks.com/help/toolbox/optim/ug/lsqcurvefit.html

[83] Coleman, T.F. and Y. Li, "An Interior, Trust Region Approach for Nonlinear Minimization Subject to Bounds," *SIAM Journal on Optimization*, Vol. 6, Page(s): 418-445, 1996.

[84] Dennis, J. E. Jr., "Nonlinear Least-Squares," *State of the Art in Numerical Analysis*, ed. D. Jacobs, Academic Press, Page(s): 269-312, 1977.

[85] Levenberg, K., "A Method for the Solution of Certain Problems in Least-Squares," *Quarterly Applied Math. 2*, Page(s): 164-168, 1944.

[86] Powell, M.J.D., "A Fortran Subroutine for Solving Systems of Nonlinear Algebraic Equations," *Numerical Methods for Nonlinear Algebraic Equations*, (P. Rabinowitz, ed.), Ch.7, 1970.

[87] Prabha Kundur, Power system stability and control,

[88] M. Sherwood, Dongchen Hu, V. Venkatasubramanian, "Real-time detection of angle instability using synchrophasors and action principle", *iREP Symposium on Bulk Power System Dynamics and Control - VII. Revitalizing Operational Reliability*, 2007. Page(s): 1-11.

[89] A.D. Rajapakse, F. Gomez, K. Nanayakkara, P.A. Crossley, V.V. Terzija, "Rotor angle instability prediction using post-disturbance voltage trajectories", *IEEE Transactions on Power Systems, Volume 25, Issue 2, 2010*, Page(s): 947 – 956.

[90] T. Ohno, T. Yasuda, O. Takahashi, M. Kaminaga, S. Imai, "Islanding protection system based on synchronized phasor measurements and its operational experiences", *Power and Energy Society General Meeting, 2008,* Page(s):1 – 5.

Appendix A DFT method and its 5 point moving median compared with NLSQ method

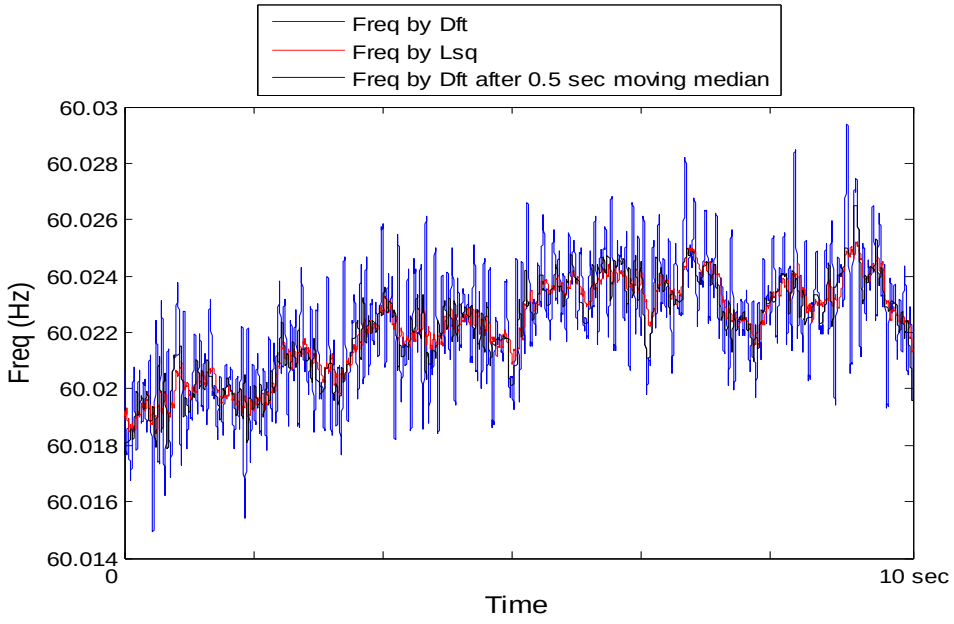

Appendix B Two area system diagram

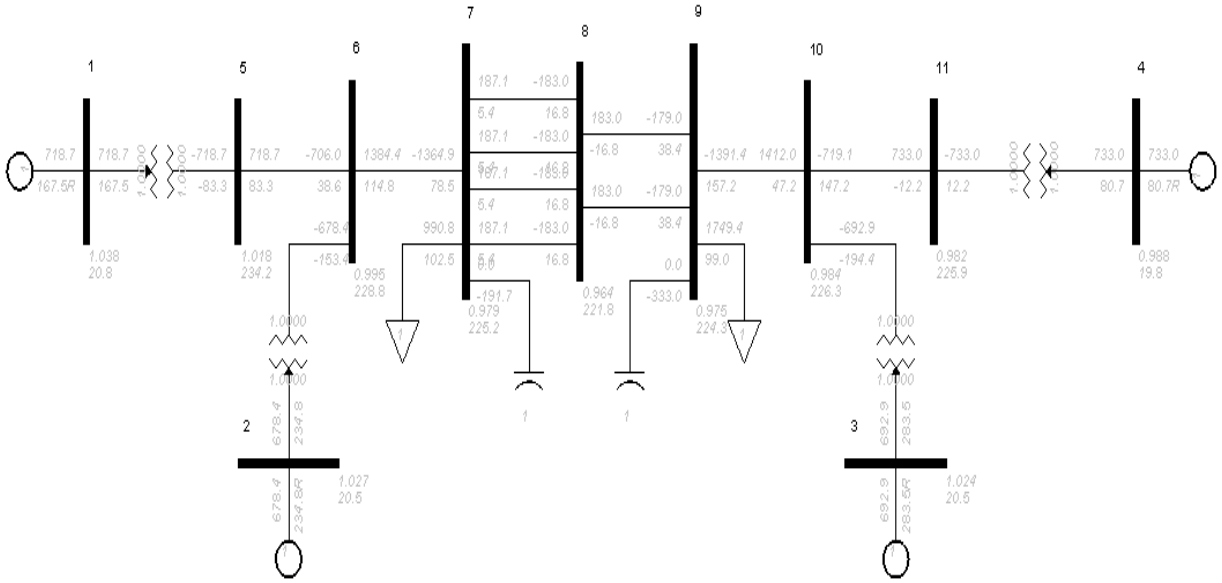

Appendix C Matlab code for NLSQ calculation

```
load voltageSignal.mat;     %input signal
sigLength = length(voltageSignal);
nomFreq = 60;   %nominal frequency
samPerCyc = 24; %points per cycle with norminal frequency sampling
PI = 3.14159265358979;
wSize = 192;                % Window size for a single LSQ fit (number of sampling points)
                            % take 1440 sampling points
                            % for example:
for m = 1:(sigLength-(wSize-1))          % matrix [V1.....V1297]
   for n = 1:wSize                  %       [V2.....V1298]
      volBuf(n,m) = voltageSignal(n+m-1);   %       [.............]
   end                              %       [V144....V1440]
   SingleWinVolBuf = volBuf(:,m);  % wSize points in SingleWinVolBuf
   xT = 1/(nomFreq*samPerCyc) : 1/(nomFreq*samPerCyc) : (wSize)/(nomFreq*samPerCyc);
   %%%%%%%%%%%%%%%%%%%%%%%%%%%%%%%%%%%%%%%%%%%%%%%%%%%%%%%%%%%%%%%%%%%%%%%%%%%%%%%
   % None-linear LSQ fit for the voltage data
   %%%%%%%%%%%%%%%%%%%%%%%%%%%%%%%%%%%%%%%%%%%%%%%%%%%%%%%%%%%%%%%%%%%%%%%%%%%%%%%
   nCenterFreq = nomFreq;
   xT = xT';
   reConV = [];
   yData1 = SingleWinVolBuf;
```

```
lowA   = max(abs(yData1 - mean(yData1)))*0.7;
UpperA = max(abs(yData1 - mean(yData1)))*1.1;
StartA = max(abs(yData1 - mean(yData1)));

lowB   = nCenterFreq - 0.8;
UpperB = nCenterFreq + 0.8;
StartB = nCenterFreq;

lowC   = -4*pi;
UpperC =  4*pi;
StartC = 0;

LowerBound = [lowA, lowB, lowC];
UpperBound = [UpperA, UpperB, UpperC];
StartPoint = [StartA, StartB, StartC];

s = fitoptions('Method','NonlinearLeastSquares',...
    'Lower',LowerBound, 'Upper',UpperBound,...
    'Startpoint',StartPoint);

f = fittype('a*sin(2*pi*b*x+c)','options',s);
[c2,gof2] = fit(xT,yData1,f);
```

```
    FreqV = c2.b;
    Angle = c2.c;
    Amplitude = c2.a;
    % reconstruct the voltage signal with the LSQ estimation equation within each window
    for reConCount = 1:length(yData1)
       reCons(reConCount) = Amplitude * sin(reConCount*2*PI*FreqV / (nomFreq*samPerCyc) + Angle);
    end

    reConV = [reConV,reCons]; % reconstruct the whole voltage signal with each LSQ window attached together
    finalFreq(m) = FreqV;
    volAngle(m) = Angle;
    % original angle is in [-pi, pi], bring it to [0, 2*pi] region
    if volAngle(m) < 0
       volAngle(m) = volAngle(m) + 2*PI;
    else
       volAngle(m) = volAngle(m);
    end
    % unWrap the angle data
    if m > 1
       unWrapCoe = ((volAngle(m) - volAngle(m-1)) / (2*PI));
       volAngle(m) = volAngle(m) - round(unWrapCoe)*2*PI;
    end
  end
```

```
figure(1);
subplot(2,1,1)
    plot(finalFreq,'b');
    legend('Frequency');
subplot(2,1,2)
    plot(volAngle,'r');
    legend('Voltage Angle');
```